The Influence of Environment on High-redshift Cluster Galaxies

a dissertation presented
by
Anna G. Delahaye
to
The Department of Physics

in partial fulfillment of the requirements
for the degree of
Doctor of Philosophy
in the subject of
Physics

McGill University
Montreal, Quebec
October 2017

Abstract

Galaxy properties such as colour, star-formation rate, and morphology are influenced by the environments in which they reside. In particular, the environments of galaxy clusters have been shown be very efficient at quenching star-formation and altering other observed galactic properties, although the specific mechanisms responsible for this evolution are not fully understood. Additionally, the effect that the cluster environment has on galaxies does not appear to be consistent at all redshifts, with high-redshift cluster galaxies having different observed properties compared to their local counterparts. In this thesis, two studies are presented that investigate the role of high-redshift galaxy cluster environments on their galactic populations.

The first study is an extensive photometric survey of the supercluster RCS2319+00, a massive supercluster system comprising three virialized cluster cores in close proximity with one another in projected space as well as redshift space. The system is located at a redshift of $z = 0.9$ and is expected to merge into a single $10^{15}\mathrm{M}_{\odot}$ cluster by $z = 0.5$, and is therefore a progenitor of the most massive cluster systems we see in the nearby universe today. Spectroscopic and submillimetre surveys have previously uncovered a complicated system of filamentary structure and infalling groups. To complement the previous studies, we assemble a large multiwavelength catalogue to identify cluster members based on photometric properties.

With a photometric catalogue complete with photometric redshifts for over 16,000 objects across the central RCS2319 field, we compile a cluster catalogue of nearly 1,800 cluster members. Using proxies for both local and global environments, we investigate the mass and colour properties of cluster galaxies depending on their specific environments within the supercluster. While we do not find a strong dependence on global environment, we do recover both a mass-density and colour-density relation depending on the local overdensity suggesting that immediate surroundings influence galactic properties more strongly than the overall structure in which it resides.

The second study presented investigates the presence of merging systems in high-redshift cluster environments compared to the field. We use a sample of four

galaxy clusters ($1.59 < z < 1.71$) discovered in the *Spitzer* Adaptation of the Red-Sequence Cluster Survey, along with a corresponding control sample. Utilizing deep imaging from the *Hubble Space Telescope*, cluster and control galaxies are classified by eye based on close pairs and distorted morphologies. We find a consistent fraction of merger candidates between the two samples, suggesting that galaxy–galaxy mergers are not a stronger source of galaxy evolution in clusters, but rather the cluster environment itself is more likely to be the dominant factor in cluster galaxy evolution.

Résumé

Les propriétés des galaxies, comme la couleur, le taux de formation stellaire et la morphologie, sont influencées par l'environnement dans lequel elles résident. Plus particulièrement, les environnements des amas de galaxies se montrent très efficaces pour étouffer la formation stellaire et altèrent d'autres propriétés galactiques observées, bien que le mécanisme responsable de cette évolution ne soit pas complètement maîtrisé. De plus, il y a une incohérence entre l'effet qu'ont l'environnement des amas sur les galaxies et le décalage vers le rouge de ces objets: les amas ayant un grand décalage vers le rouge ont des propriétés différentes des amas locaux. Cette thèse présente deux études portant sur le rôle des environnements des amas ayant de grands dcalages vers le rouge sur leurs populations galactiques.

La première étude est un relevé photométrique extensif du super-amas RCS2319+00, un super-amas massif comptant 3 noyaux d'amas en équilibre dynamique situés à proximité les uns des autres. Le système se situe à un décalage vers le rouge de z $= 0.9$ et devrait fusionner en un unique amas de $10^{15}M_{\odot}$ d'ici z $= 0.5$. Ce système est donc un progéniteur de l'amas le plus massif observable dans l'univers proche. Les relevés spectroscopiques et submillimétriques ont précédemment dévoilé un système complexe de structures filamenteuses et de groupes retombant vers leurs coeurs. Pour compléter ces travaux, nous assemblons un grand catalogue multi-longueur d'onde pour identifier les membres d'amas en se fondant sur leurs propriétés photométriques.

Avec un catalogue photométrique complet incluant les mesures photométriques des décalages vers le rouge de plus de 16 000 galaxies situées dans la zone centrale de RCS2319, nous compilons un catalogue d'amas ayant plus de 1 800 membres de cet amas. En utilisant des quantités relatives à l'environnement local et global, nous examinons la dépendance entre la masse et les couleurs des galaxies d'amas et leur environnement spécifique au sein du super-amas. Tandis que nous n'identifions pas de forte dépendance avec l'environnement global, nous percevons une relation entre la masse et la densité des galaxies, et une autre entre la couleur et la densité, qui dépendent de la surdensité locale. Cela suggère que

l'environnement immédiat influence plus fortement les propriétés des galaxies que l'environnement global.

La deuxième étude présentée dans cette thèse examine la présence de systèmes en processus de fusion dans les amas à grands décalages vers le rouge en comparaison avec les galaxies du champ. Nous utilisons un échantillon de quatre amas de galaxies ($1.59 < z < 1.71$), découverts par le relevé du *Spitzer Adaptation of the Red-Sequence Cluster*, de même qu'un échantillon de contrôle. En utilisant de l'imagerie profonde avec le télescope spatial Hubble, les galaxies incluses dans les échantillons sont visuellement classifiées en se basant sur leurs morphologies déformées et la présence de paires rapprochées. Nous trouvons des fractions de candidats en processus de fusion qui sont cohérentes entre les deux échantillons, suggérant que les galaxies en fusions ne sont pas une importante source de l'évolution galactique au sein des amas. L'environnement de l'amas serait plutôt le facteur dominant quant à l'évolution des galaxies dans les amas.

Contents

Listing of figures

Listing of tables

In memory of my grandparents, Gladys and Walter.

Acknowledgments

First, I would like to thank my supervisor, Tracy Webb, for her support and guidance throughout my graduate studies. The members of the RCS and SpARCS collaborations have provided invaluable feedback, constructive criticism, and support throughout my projects, especially Howard Yee and Gillian Wilson. Jim Geach was especially helpful in introducing me to the world of wide-field imaging. Merci beaucoup to Emilie Parent for the translation of the abstract.

Many thanks to both my parents, for their love and support throughout my education. I especially thank my grandparents, Gladys and Walter Dick, for their encouragement and generosity that has enabled me to get to where I am today. Finally, I thank my other half, Paul Scholz. I can't wait until we start the next chapter of our lives together.

Contribution of Authors

All text presented in this thesis was written by myself, and except in cases specifically noted all figures were created by myself.

Chapter 3

The RCS2319+00 supercluster and SpARCS−J1049 cluster were discovered by the RCS and SpARCS collaborations, respectively. The multiwavelength optical and near-infrared data for RCS2319+00 were obtained by Tracy Webb (PI) on behalf of the RCS collaboration. I was the PI and wrote the proposal for the follow-up observations of SpARCS−J1049. I performed all the reduction outlined in the chapter, with assistance and guidance from Jim Geach. PSF convolution of the z observations for SpARCS−J1049 was done by Alex Tudorica for uniformity with the other SpARCS−J1049 optical data, but otherwise the reduction and calibration was done by myself.

Chapter 4

All photometric redshift analysis described in the chapter was performed by myself, with guidance and suggestions from Jim Geach, Tracy Webb, and Paul Hsieh. Estimations of stellar masses were done by Tracy Webb.

For RCS2319+00, R_C and z' photometry was provided by Howard Yee and Mike Gladders, IRAC photometry was provided by Tracy Webb, and spectroscopic redshifts were provided by Ashley Faloon with assistance from Erica Ellingson and Renbin Yan.

For SpARCS−J1049, optical photometry in $u^*g'r'z'$ was provided by Alex Tudorica. I assembled the near-infrared (J and K_s) and infrared (3.6μm and 4.5μm) catalogues from the online databases for the UK Infrared Deep Survey (UKIDSS), and the *Spitzer* Extragalactic Representative Survey (SERVS), respectively. Spectroscopic redshifts were assembled by Tracy Webb from a variety of sources in-

cluding publicly available data and SpARCS observations provided by Andrew deGroot and Gillian Wilson.

Chapter 5

The environmental study of RCS2319+00 was conceived by Tracy Webb, with the specific analyses presented decided by Tracy Webb and myself. All the analyses, including the development of customized software, were done by myself. Invaluable feedback, guidance and suggestions were provided by Tracy Webb, Jim Geach, Howard Yee, David Gilbank, and Ashley Faloon.

Chapter 6

The merger study of the high-redshift SpARCS clusters was conceived and designed by myself. The selected clusters were discovered by the SpARCS collaboration. Spectroscopic redshifts were determined by Andrew deGroot and Gillian Wilson and photometric catalogues for the three clusters besides SpARCS−J1049, including stellar masses and photometric redshifts, were provided by Julie Nantais. The *HST* data were obtained from several programs (PIs Gillian Wilson and Saul Perlmutter). The reduction and processing of the *HST* imaging were done by Brian Hayden, Kyle Boone, Ryan Foltz, and Gillian Wilson. I developed the interactive classification software. Tracy Webb, Gillian Wilson, Adam Muzzin, and Howard Yee all provided substantial comments and feedback on the project.

Appendix

All data summarized in Table A.1 were obtained by the RCS collaboration, and reduced and calibrated by myself.

1

Introduction

1.1 Overview

Matter in the universe is not uniformly distributed. The large scale structure of the universe is composed of a complicated web of filaments populated by galaxies, and empty voids. The intersecting nodes of this 'cosmic web' are populated by large associations of galaxies: galaxy clusters. Galaxy clusters represent the most massive gravitationally bound systems in the universe, the result of the largest primordial overdensities in the universe collapsing. Their masses typically range from 10^{14} to $10^{15} M_{\odot}$ and are populated by hundreds to thousands of galaxies,

although stellar matter makes up only approximately 2% of the cluster mass. 10−12% of the cluster mass resides in the intracluster medium (ICM) in the form of an X-ray emitting halo of hot gas (Andreon, 2010; Gonzalez et al., 2013). However, the dominant mass source of galaxy clusters is non-baryonic, composed of a massive dark matter halo which comprises the remaining ∼85% of the cluster mass. Galaxy clusters feature a wide variety of environments, from the cluster outskirts which can be typical of low-density field environments, to the cores which provide the densest environments in the universe, and everything in between.

Clusters are formed via a 'bottom-up' approach, in which smaller systems (such as galaxies) collapse first and then coalesce into larger systems such as galaxy groups, and eventually clusters. Studying clusters at a variety of redshifts thus provides a probe into understanding how large scale structures are formed and how they evolve with cosmic time. Not only can clusters offer insight into the history of hierarchical structure formation, but they are also excellent systems for studying the effect that environment has on galactic populations throughout cosmic history.

The following thesis presents two studies involving high-redshift clusters in which we investigate the effect of the cluster environment on the cluster galaxy populations. The first study involves a photometric survey of the high-redshift supercluster RCS231955+00. Located at $z = 0.9$, RCS231955+00 is a progenitor of modern day massive clusters like the Coma Cluster, but at a lookback time of 7.5 billion years ago. The second study is a morphological analysis of four galaxy clusters in the redshift range $1.59 < z < 1.71$, presenting a sample of clusters

formed only 4 billion years after the Big Bang, nearly 10 billion years in lookback time.

In Chapter 1, a brief history of structure formation including galaxy clusters is outlined, along with the correlations galaxies exhibit between their characteristics and environments and how they evolve with cosmic time. Chapter 2 provides additional background on the instrumentation utilized, as well as the methodologies for galaxy cluster detection and how they are adapted for high-redshift surveys.

Chapter 3 describes the extensive imaging reduction and calibrations undertaken in order to provide wide-field multiwavelength catalogues. In Chapter 4, the calibrated data described in Chapter 3 are assembled and used to determine photometric redshifts, including descriptions of the methodology and execution.

The results of the photometric study of RCS231955+00 are presented in Chapter 5. Different definitions of environment are employed to probe both local and global surroundings, and the distributions of galactic properties such as colour and mass are investigated in terms of their environments.

Chapter 6 presents a study on the presence of merging galaxy systems in very high-redshift galaxy clusters. We utilize high resolution imaging to classify galaxy morphologies across several high-redshift clusters and compare against a corresponding field control sample.

Conclusions of the thesis and future work to progress the presented studies are given in Chapter 7.

1.2 Hierarchical Structure Formation

The formation of structure in the universe is described by a 'bottom-up' paradigm in a $\Lambda-$cold dark matter (ΛCDM) cosmology. ΛCDM states that the universe is composed of 5% baryonic matter, such as stars and gas, 25% non-baryonic matter in the form of cold (non-relativistic) dark matter, and 70% dark energy (Planck Collaboration et al., 2016). In this scenario, small scale fluctuations in the early universe result in over and underdense regions. Matter, baryonic and non-baryonic, begins to fall into the overdensities, thus increasing the size of the potential wells. While the non-baryonic dark matter remains non-interacting and serves only to deepen the gravitational well, eventually the baryons will hit a threshold and begin to collapse into stars, forming small systems such as low mass galaxies and globular clusters. As cosmic time evolves, the potential wells deepen and begin merging together along filamentary networks. Small galaxies merge into large galaxies, large galaxies merge into groups, and groups merge into galaxy clusters and superclusters. Large dark matter simulations following a ΛCDM cosmology such as the Millennium Run I (Springel et al., 2005) and II (Boylan-Kolchin et al., 2009) have simulated the evolution of large scale structure throughout cosmic time. Figure 1.1 from the Millennium$-$II Run shows snapshots in dark matter assembly of a massive galaxy cluster at several scales and epochs, from less than one billion years after the Big Bang to present day. At higher redshifts, only the smallest perturbations have collapsed, and as the universe evolves, larger and larger structures begin forming. In fact, the largest gravitationally bound structures in the universe $-$ mergers of galaxy clusters, or superclusters $-$

are only beginning to collapse at the current epoch.

The matter accretion and merging of dark matter haloes occurs along the filamentary structure visible in Figure 1.1 and widely reproduces the large scale structure seen in the local universe. Spectroscopic redshift surveys such as the Sloan Digital Sky Survey (SDSS; York et al., 2000) and the 2 degree Field Galaxy Redshift Survey (2dFGRS; Colless et al., 2001; Peacock et al., 2001) have mapped the three-dimensional locations of galaxies in the local universe. Figure 1.2 from the 2dFGRS (Peacock et al., 2001) shows a narrow slice in declination of over 140,000 galaxies out to a redshift $z = 0.2$. Although the depth limits completeness out to $z = 0.1$ or so, a complex structure of filaments, nodes and voids is revealed and widely consistent with dark matter simulation efforts.

1.3 Environmental Effects on Galaxy Properties

Many studies have shown that galaxy colours exhibit a clear bimodality with galaxies either exhibiting predominantly red or blue populations, defined as being part of the red-sequence or blue-cloud, respectively (e.g., Strateva et al., 2001; Hogg et al., 2002; Baldry et al., 2004). Indeed, many galaxy properties are found to correlate with this colour bimodality. Galaxies located in the red-sequence are more likely to be early-type ellipticals with low star-formation rates and high stellar mass, whereas the blue-cloud tends to be populated by low-mass, late-type star-forming spirals (e.g., Brown et al., 2000; Kauffmann et al., 2003; Balogh et al.,

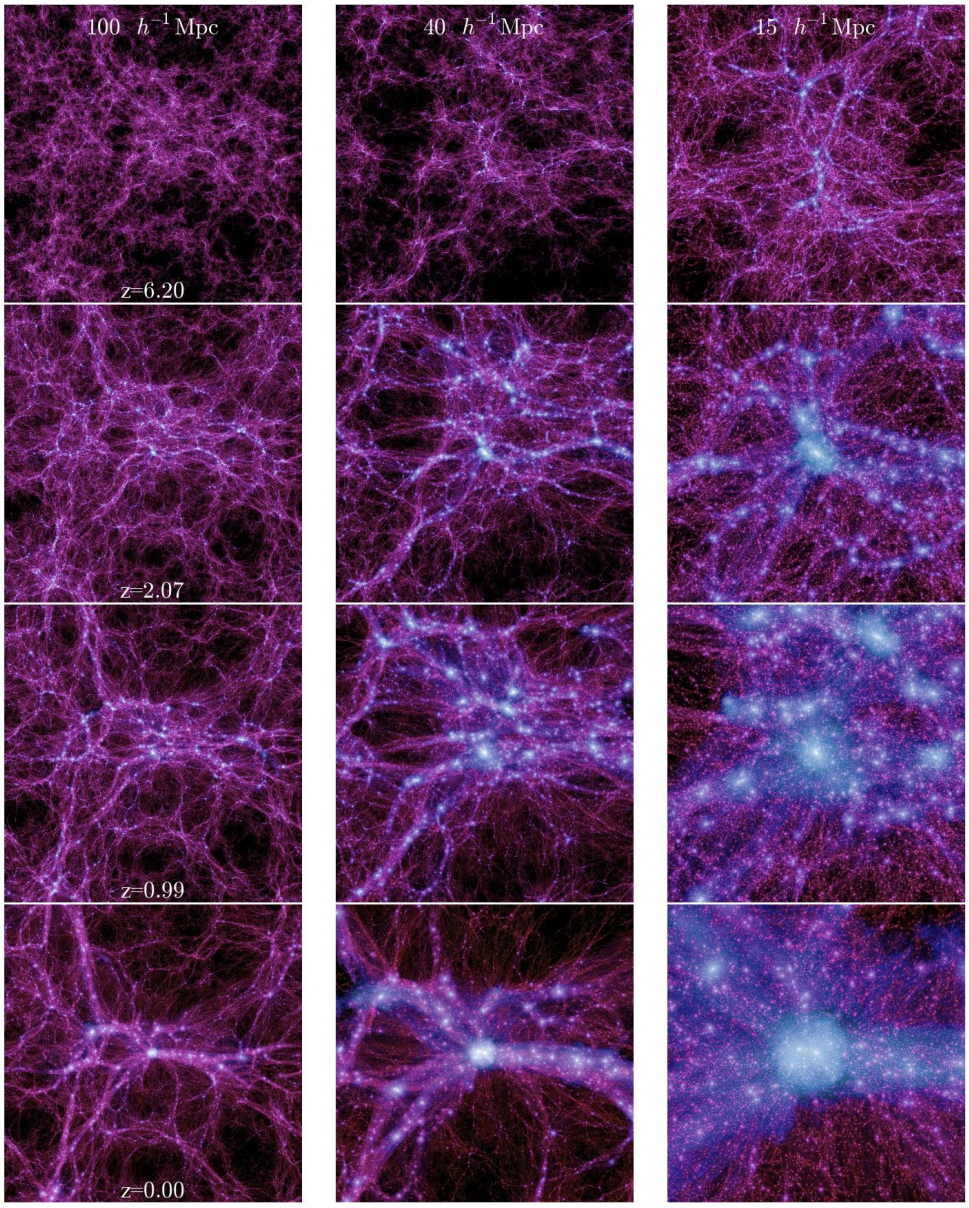

Figure 1.1: Evolution of a cluster-mass dark matter halo from the Millennium−II Simulation. The cluster is shown at redshift snapshots $z = 6.22, 2.07, 0.99$, and 0, across three different distance scales ($15 - 100h^{-1}$ Mpc). At higher redshift, only smaller haloes are present, with the size of the largest collapsed halo increasing with cosmic time. The small scale images illustrate the accretion of material along filamentary structures. Figure from Boylan-Kolchin et al. (2009).

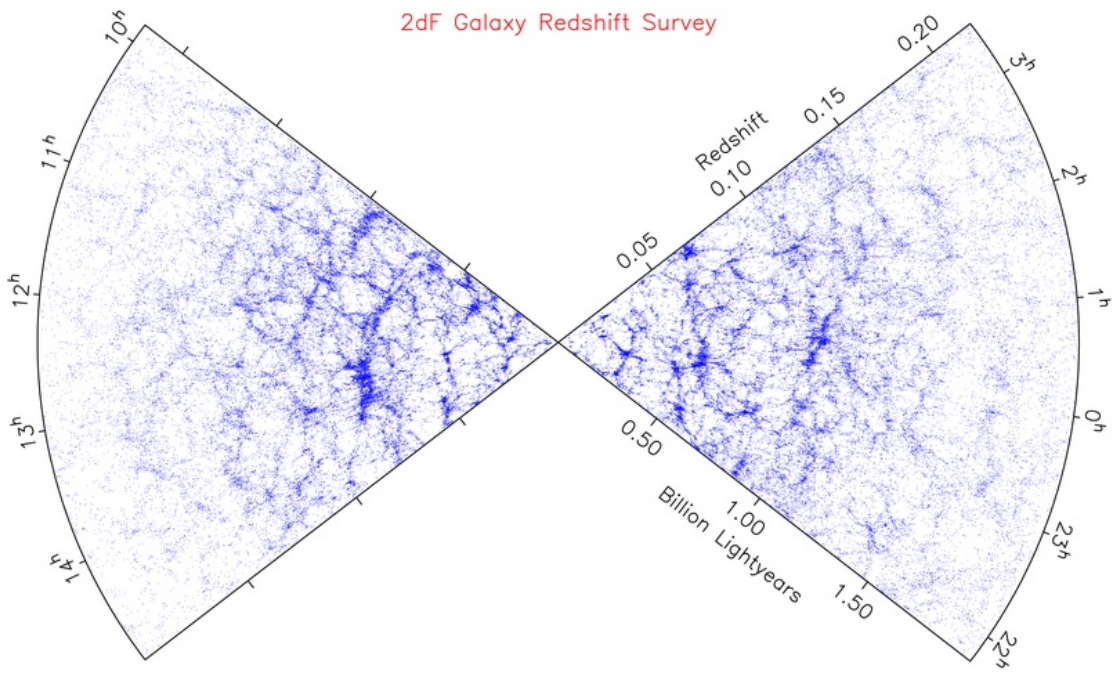

Figure 1.2: Distribution of over 140,000 galaxies as mapped out by 2dFGRS (Peacock et al., 2001). The dense nodes indicate positions of clusters and superclusters, connected via filamentary structures with large voids in between. (Image credit: 2dF Image Gallery)

2004; Hogg et al., 2004), as illustrated in Figure 1.3, taken from Schawinski et al. (2014). In the local universe, these properties are also found to be related to the environment in which the galaxies reside. The morphology−density relation first observed by Dressler (1980) states that the fraction of early-type galaxies in cluster environments increases with density, compared to their late-type counterparts which are more likely to be found in the low-density cluster outskirt environments. Star-formation rates (SFR) are also found to correlate with local density, with SFR decreasing with increasing local density at low redshift (Gómez et al., 2003; Kauffmann et al., 2004). However, stellar mass, colour, and SFR are all dependent on one another and disentangling these properties with respect to environment can be difficult. SFR per unit mass (sSFR) or per unit luminosity (SFRN) can be used as control for galaxy type, but both properties are still shown to decrease with increasing local density (Gómez et al., 2003; Kauffmann et al., 2004).

At higher redshifts ($0.5 < z < 2$), the relation between star-formation and density is still found to exist (Quadri et al., 2012; Strazzullo et al., 2013) and the morphology−density relation (or colour−density relation) is evident in both cluster and group environments (Holden et al., 2007). sSFR is also still shown to decrease with both density and mass when controlled for the other in cluster environments (Patel et al., 2009; Muzzin et al., 2012). However, at some point at an earlier epoch stellar mass assembly must have occurred in the denser cluster environments, likely coupled with increased star-formation.

Indeed, beyond a redshift of $z = 1$, this relation between density and SFR has been found to weaken. Several studies have revealed a reversal in the SFR−density

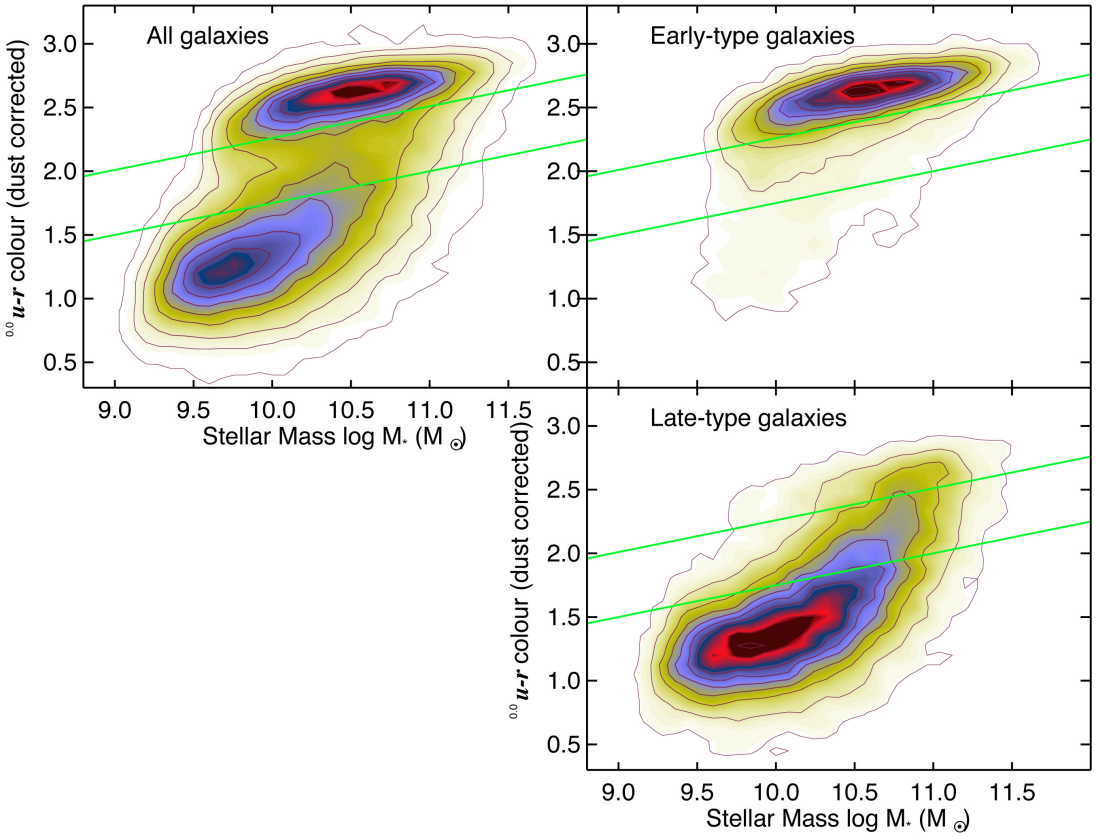

Figure 1.3: An example of galaxy bimodality from a sample of SDSS galaxies, illustrated in colour–stellar mass space from Schawinski et al. (2014). The colour in this case is the difference between the u and r filters, where a larger number indicates a redder colour. The populations are further split morphologically – into early- and late-type – highlighting a strong dependence on colour and morphology, with the red-sequence mostly dominated by early-type elliptical galaxies, and the blue-cloud populated by late-type spirals.

relation in non-cluster environments at these redshifts (Elbaz et al., 2007; Cooper et al., 2008), including finding high-density regions populated with a higher fraction of blue galaxies (Grützbauch et al., 2011). Additionally the fraction of blue (star-forming) galaxies is shown to increase with redshift, the Butcher−Oemler effect (Butcher & Oemler, 1984), and the global star-formation rate has been steadily decreasing since $z \sim 1$ (Lilly et al., 1996) with an enhanced decrease in cluster environments (Haines et al., 2013). This increase in SFR with increasing redshift has been witnessed in even the denser core regions of galaxy clusters (Tran et al., 2010; Brodwin et al., 2013; Santos et al., 2015), including in the central brightest cluster galaxy regions (Webb et al., 2015b; McDonald et al., 2016).

Overdensities of submillimetre sources at $z \sim 1-2$ suggest elevated levels of star formation over cluster and proto-cluster environments at high redshift (Clements et al., 2014). Indeed, a transition epoch between unquenched and quenched SFRs at a redshift of $z \sim 1.4$ has been postulated by infrared studies of cluster populations (Mancone et al., 2010; Brodwin et al., 2013; Alberts et al., 2014). SFRs in the cluster outskirts and into denser core regions are shown to be comparable or even enhanced relative to the field at these high redshifts, indicating a rapid quenching period occurring in clusters over $\sim z = 1.2-1.4$ to explain the relatively quenched cluster populations we see by $z = 1$ (Nantais et al., 2017). The mechanisms responsible for this quenching are not thoroughly understood, but the notable differences in quenching timescales between cluster galaxies and field galaxies suggest that there exist influences specific to cluster environments that are quenching galaxy star-formation and altering morphology.

1.3.1 Cluster Environment Quenching Mechanisms

Galaxy–ICM Interactions

The hot intra-cluster medium (ICM) of a galaxy cluster can interact directly with infalling galaxies in different ways depending on factors such as the mass of the cluster's potential well and the rate at which the galaxy is infalling.

Ram-pressure stripping refers to the rather violent interaction between a galaxy and the ICM, wherein the galaxy's gas is stripped away from it as it quickly plunges through into the cluster potential well. The gas is compressed which may trigger brief periods of star-formation, but the hot ICM removes cool gas from the galaxy and prevents future epochs of star-formation, dominating the galactic gravitational pull on the tenuous gas (Gunn & Gott, 1972). This process is rapid, with a short quenching timescale causing the galaxy to evolve from star-forming to quiescent. Stripping occurs when the pressure of the ICM dominates over the galaxy's gravitational hold over its interstellar medium (ISM), thus depending on the density of the ICM and mass of the infalling galaxy, with lower mass galaxies having a higher chance of experiencing ISM stripping. Simulations have shown that the inclination of the infalling galaxy plays a significant role in how efficient the stripping is, as well as illustrated how ram-pressure stripping can affect the angular momentum distribution and result in disturbances and morphological changes within the disk structure (Schulz & Struck, 2001). There is evidence of ram-pressure stripping occurring in nearby clusters, also suggesting that ram-pressure stripping could be responsible for deforming and warping the shape of

disk galaxies (Crowl et al., 2005).

A less violent and longer timescale mechanism for quenching star-formation is strangulation. In this case, while cold gas is not actively forced out of the incoming galaxy, the hot ICM prevents the accretion of new cool gas, and any gas that may be blown out during star-formation or active galactic nuclei (AGN) activity will be unable to re-accrete. This results in a slower transition from star-forming to quenched, as the available reserves of gas in the galaxy will remain gravitationally bound and able to form stars, but once the reservoir is used up star-formation will cease. Strangulation, or starvation, was first proposed by Larson et al. (1980) to explain the presence of lenticular galaxies in galaxy clusters, where low gas content and low rates of star-formation is seen, but the morphology exhibits disk-like properties. Despite being possible in cases of ram-pressure stripping, starvation does not trigger star-formation beyond any that was on-going before infall. Some studies investigating the stellar ages and metallicities of cluster galaxies favour the longer transition timescale of strangulation as the dominant source of star-formation quenching in cluster environments (Peng et al., 2015).

Galaxy–Galaxy Interactions

Galaxy–galaxy interactions are not unique to cluster environments, unlike ram-pressure stripping and strangulation which require the extended hot gas present in galaxy clusters. Galaxy−galaxy interactions simply require the presence of other neighbouring galaxies. This can occur more readily in cluster environments due to the higher local density of galaxies, although galaxies in relatively isolated

environments and group environments can still interact gravitationally.

The most dramatic form of galaxy–galaxy interactions are galaxy mergers, where two (or more) galaxies collide with one another and eventually merge into one single system. Major mergers, where the mass ratios between the interacting galaxies is similar, will vastly alter the appearance and characteristics of the final remnant compared to the progenitors (Toomre & Toomre, 1972). Due to the vast space between stars within the galaxies, direct collisions between stars are unlikely; however, the low density gas and molecular clouds populating the interstellar medium (ISM) can compress and trigger massive bursts of star-formation (Sanders & Mirabel, 1996). The gravitational interactions can also affect orbital paths, causing tidal tails and distorted morphology, and funnel material into the central black holes, triggering active galactic nuclei (e.g. Kauffmann et al., 1993; Hopkins et al., 2008).

A less extreme but more common example of galaxy–galaxy interaction in cluster environments is galaxy harassment (Moore et al., 1996). These are typically higher speed encounters where the relative velocities between the constituent galaxies are too high for eventual coalescence, but they pass close enough to trigger gravitational distortions. Simulations by Moore et al. (1996) have shown that heating caused by repeat encounters can alter the overall velocity dispersion within spiral galaxies, causing the overall stellar distribution, and therefore light profile, to change. As a common metric for morphological type involves the shape of the light profile (for example, using the Sérsic index as a proxy for elliptical or spiral morphology (e.g. Sersic, 1968; Caon et al., 1993; van der Wel, 2008)),

harassment can trigger morphological changes causing spiral galaxies to begin to exhibit ellipitical and spherical galaxy properties. The degree of harassment and the ensuing morphological and stellar mass changes are found to depend significantly on the particular properties (such as infall rate and disk orientation) of galaxies falling into the cluster halo (Bialas et al., 2015). Harassment, like mergers, can trigger brief periods of intense star-formation as gas reservoirs are disturbed, before enhanced stripping or morphological transformations begin to dominate (Moore et al., 1998).

2

Observatories and Methodology

An significant part of this thesis concerns the reduction and calibration of optical and near-infrared data in order to characterize the spectral energy distributions (SEDs) of galaxies. The facilities used for the majority of this data collection are described in this chapter, along with the methodology that led to the discovery of the observational targets.

2.1 Canada-France-Hawaii Telescope

The Canada-France-Hawaii Telescope (CFHT) is a telescope facility run by the National Research Council of Canada, the Centre National de la Recherche Scientifique of France, and the University of Hawaii. The CFHT hosts a 3.6 m optical and near-infrared telescope and is located on Mauna Kea at a height of 4200 m. Mauna Kea provides excellent conditions for astronomical observations; the elevation results in a thinner atmosphere improving optical observations, and the aridity decreases water contamination in near-infrared observations. Although its mirror diameter is small compared to the other 8−10 m class observatories located on the summit of Mauna Kea, the CFHT's world-class instrumentation keeps it at the forefront of optical and near-infrared observatories.

2.1.1 CFH12K Camera

Prior to 2003, the optical camera on the CFHT was CFH12K. It consisted of 12 CCDs, three of which were red-sensitive entailing enhanced response to long wavelengths, manufactured by MIT Lincoln Laboratories. Each CCD had dimensions of 4096×2048 pixels and were arranged in a 2×6 array with approximately $7''$ gaps between chips. With a pixel scale of $0.206''$/pixel, its field of view of was $28' \times 42'$. (See Figure 2.1 for detector layout.) While the CFH12K represented a huge step forward in the era of wide-field imaging, many issues such as fringing, chip-to-chip response variations, and peculiarities in saturation, required extensive and careful reduction and calibrations to obtain optimal data.

2.1.2 MegaCam

MegaCam is the wide-field optical imager located at the prime focus of the CFHT and has been in use since 2003. MegaCam consists of an array of 36 e2v detector CCDs in a 4×9 layout with each chip having dimensions 4612×2048 pixels per chip. Since 2015, an updated set of filters has allowed expansion to 40 CCDs with the central two rows having additional CCDs at either end (the 'wings'). The pixel scale is approximately 0.187″/pixel resulting in a full field-of-view of 0.96×0.94 degrees, not including the wings. Between each chip is a small gap of 13″ (70 pixels), with two large gaps (80″ or 425 pixels) between the top two and bottom two rows. See Figure 2.1 for layout.

MegaCam has a set of five broadband filters (u^*, g', r', i', z'), shown in Figure 2.2, designed to match the filters of the Sloan Digital Sky Survey (SDSS) and ranging in wavelength from approximately 3000−10000 Å. In 2015 these were updated and renamed u, g, r, i, and z and have roughly the same filter shape and response as their predecessors.

2.1.3 Wide Field Infrared Camera

The near-infrared camera on the CFHT is the Wide-Field Infrared Camera (WIRCam). WIRCam consists of 4 Hawaii−2RG detectors of dimension 2048×2048 pixels with a resolution of 0.307″/pixel, giving a field-of-view of approximately $21' \times 21'$. The chips are arranged in a 2×2 configuration with 45″ gaps between them, shown in Figure 2.1.

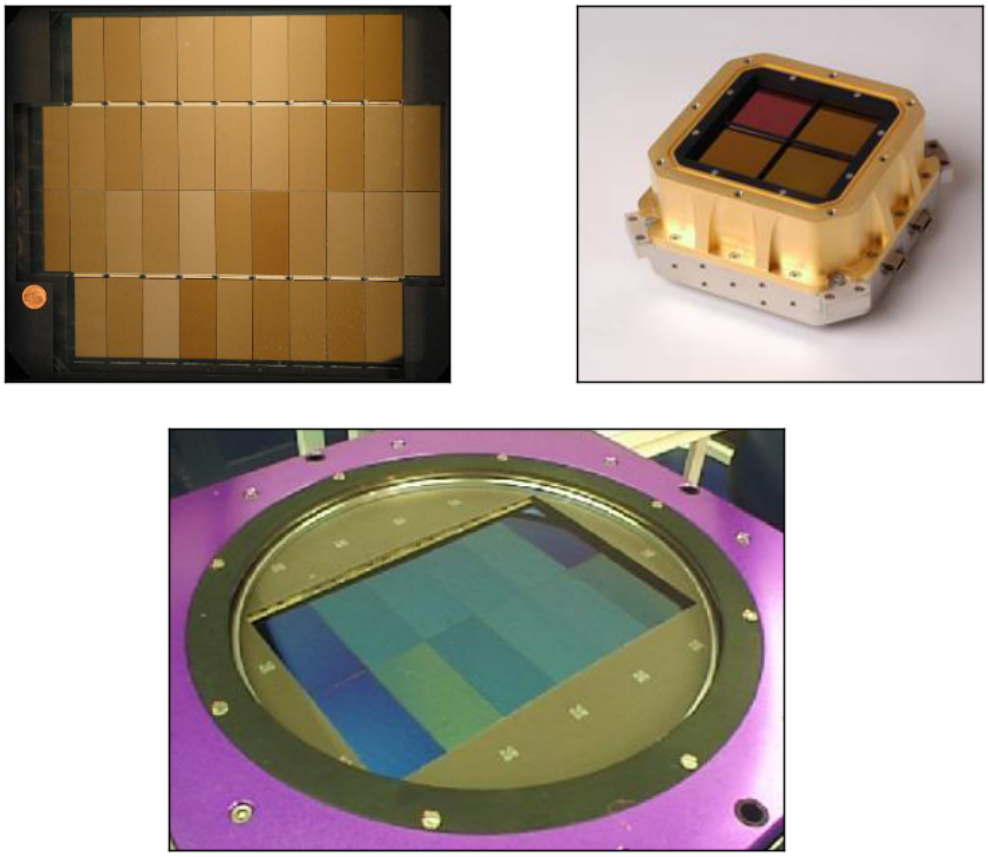

Figure 2.1: *Top Left:* Photo of MegaCam focal plane illustrating the chip layout, including the pair of 'wings' on either side. (Image credit: Canada-France-Hawaii Telescope/2003). *Top Right:* WIRCam 2×2 array of HAWAII$-$2RG detectors. *Bottom:* Photo of CFH12K array, used before MegaCam was installed in 2003 (Image credit: Canada-France-Hawaii Telescope/1999).

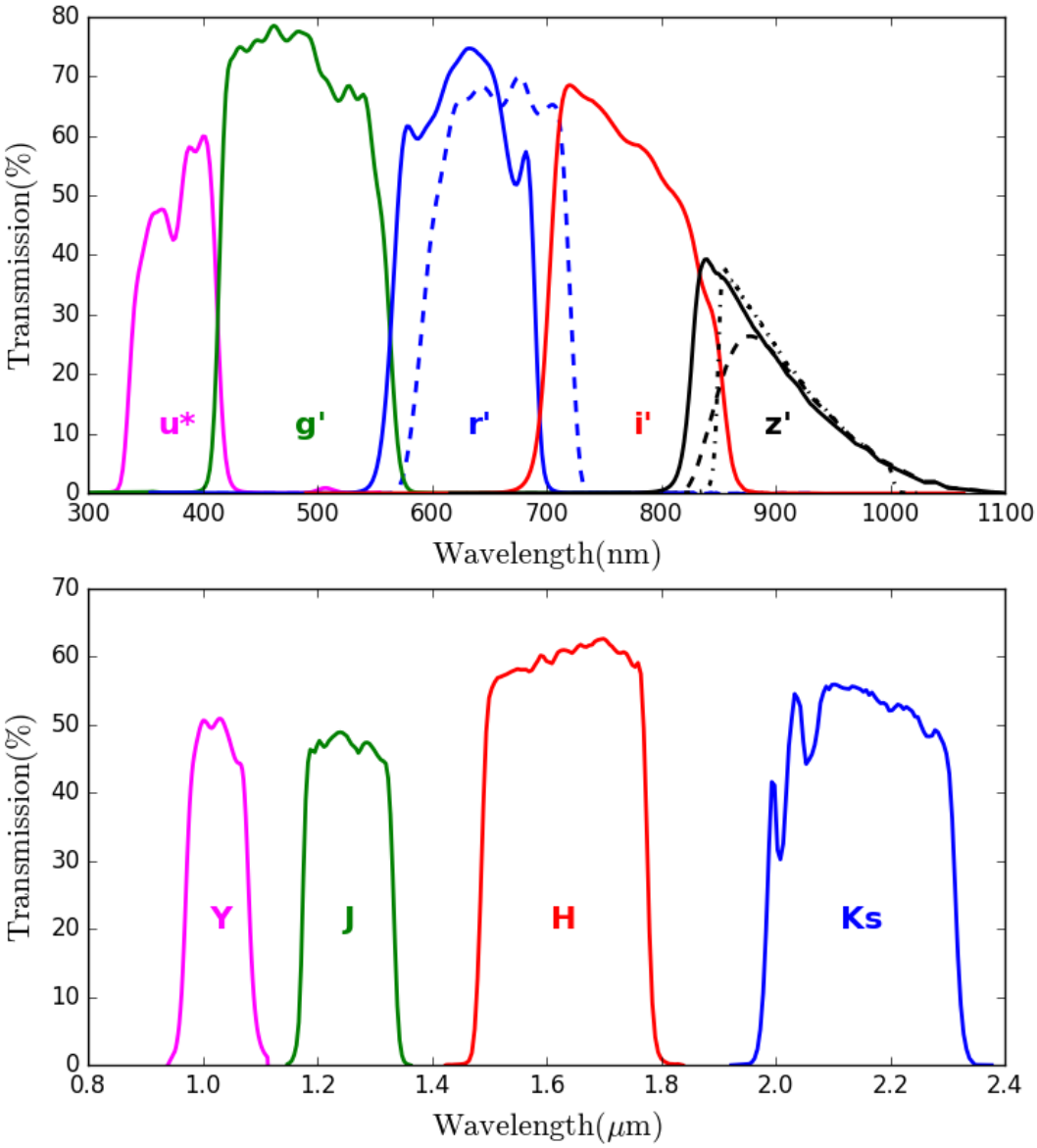

Figure 2.2: *Top:* The filter response curves of the Megacam filters. The solid lines indicate the $u^*g'r'i'z'$ filters than were in use from 2003 to 2015. The g' and i' observations presented in this thesis were taken with this filter set. The dashed r and z curves represent the filters R_C and z' which were on the CFH12K camera and used by the Red-Sequence Cluster Survey for cluster identification. The dot-dashed z' filter indicates the new z filter that was installed in 2015. This filter was used for additional observations of SpARCS1049.*Bottom:* Transmission curves for the four broadband filters on WIRCam. The observations presented in this thesis were primarily done with filters J and Ks.

WIRCam has four broadband near-infrared filters ranging from 0.95 to 2.3 μm, as shown in the bottom panel of Figure 2.2.

2.2 Cluster Finding Surveys

Galaxy clusters represent the highest overdensities of mass in the universe and trace out large-scale structure. As such, they can be used to determine cosmological parameters, such as σ_8 and Ω_0, and test cosmological models (e.g. Carlberg et al., 1996; Eke et al., 1996; Henry, 2000; Gladders et al., 2007; Allen et al., 2011, for review). However, these studies require large, unbiased samples of clusters across many epochs.

Early galaxy cluster surveys consisted of simply looking for heightened concentrations of galaxies using optical photometric plates (Abell, 1958; Zwicky & Rudnicki, 1963). While these methods allowed the identification of hundreds to thousands of galaxy clusters, the risk of contamination from foreground and background sources was high, and the only clusters detectable were in the nearby universe ($z \sim 0.2$). The advent of new CCDs that could image large areas of the sky and be processed automatically prompted searches for optical detections of galaxy clusters beyond the nearby universe (Postman et al., 1996; Lidman & Peterson, 1996). However, the issues of projection and false detections remained prevalent. The field experienced a resurgence in the '80s and '90s with the advent of large scale X-ray surveys, such as *Einstein* (Gioia et al., 1990; Gioia & Luppino, 1994) and *ROSAT* (Rosati et al., 1998). Bremsstrahlung radiation from the hot

electron gas in the gravitational potential well of the cluster results in diffuse X-ray haloes which allowed the detection of thousands of new galaxy cluster candidates. This method has lower likelihood for false detections as the X-ray halo will only populate an intrinsically dense system, so line-of-sight overdensities will not emit X-rays. However, as the brightness of the X-ray halo scales with cluster mass, clusters are selected to be more massive and lower mass clusters may be missed. Additionally, at higher redshifts the X-ray halo may not have evolved enough for detection or even exist yet in low mass systems. As such, shallow wide-field surveys would find the only nearest and most massive clusters, and deep narrow-field surveys would find lower mass and more distant clusters but would become limited by the intrinsic rarity of galaxy clusters (approximately one per square degree). To probe the entire mass function of galaxy clusters as well as extend beyond the local universe, a reliable detection method for low mass clusters is required.

By the late '90s, large-field optical imaging observatories became available for deep and wide-field surveys. The Cluster Red-Sequence Method (CRS) (Gladders & Yee, 2000) was developed as a method to utilise the newly available wide-field imaging capability of new optical instrumentation including incorporation of CCDs, and provide a clean, robust sample of galaxy clusters across many epochs. Most importantly, CRS provides an algorithm which can be run automatically on large datasets, eschewing the requirement for individual visual verifications.

CRS makes use of the fact that galaxy clusters are known to be populated by so-called 'red and dead' early-type galaxies which fall along a well-defined line in colour−magnitude space (Dressler, 1980; Bower et al., 1992). The most

significant feature in a galaxy's spectrum separating the red and blue populations is the 4000Å break, a discontinuity caused by absorption due to metals in older (redder) populations of stars. The older a galaxy's population is, the deeper the break. Using a clever selection of filters designed to bracket this gap, the CRS algorithm can detect overdensities in colour, magnitude, and position thus selecting for galaxy clusters at a given redshift. Not only is this relation shown to exist in higher redshift colours, but the colour of the red-sequence will redden with redshift thus providing a preliminary photometric redshift estimate (Stanford et al., 1998; López-Cruz et al., 2004). Figure 2.3 illustrates the position of the red-sequence in colour−magnitude space as a function of redshift, in this case using the filters V and I_C centred at approximately 5500Å and 8000Å, respectively. The contamination is lower than other optical based methods, as the brightest, reddest galaxies at a given redshift will trace the cluster potential and any foreground or background sources will not exhibit the same properties. The CRS method thus provides a relatively clean sample of galaxy clusters across many epochs, with relatively inexpensive observation constraints, requiring only two-filter imaging for detection over a wide range in redshift.

2.2.1 Red-Sequence Cluster Survey

The Red-Sequence Cluster Survey (Gladders & Yee, 2005) (RCS) utilized the CRS method developed in Gladders & Yee (2000) and surveyed nearly 100 deg^2 in both the northern and southern sky. The northern portion of the survey used the Canada-France-Hawaii Telescope (CFHT) and its, at the time, state-of-the-art

CFH12K camera. The filters R_C and z', centred on wavelengths 6500 Å and 9100 Å, respectively, were selected to bracket the 4000 Å break and search for clusters over $0.2 < z < 1.4$. In total, 10 patches were observed with the CFHT resulting in a northern survey area of 46 deg^2. A set of 12 complementary southern patches were also observed with the Cerro-Tololo Inter-American Observatory (CTIO), a 4m optical telescope based in Chile.

Thousands of galaxy clusters, galaxy groups, and candidates were discovered in the survey, allowing statistical studies to be done on the properties and evolution of galaxy clusters. Studies have used the RCS galaxy cluster sample to investigate everything from the evolution of star-formation rates (Webb et al., 2013), to cluster scale dark matter haloes (Simon et al., 2008; Jee et al., 2011), to cosmological constraints (Gladders et al., 2003, 2007). Its success prompted an expanded iteration RCS-2 (Gilbank et al., 2008), a nearly 1000 deg^2 survey searching for clusters over approximately the same redshift range ($0.1 < z < 1.0$). RCS-2 took advantage of the new larger field optical camera on the CFHT, Megacam. The survey comprised the similar r' and z' filters for the 4000 Å break brackets, as well as the bluer g' filter, to characterize foreground sources better as well as search for gravitationally lensed background sources.

Discovery of RCS2319 Supercluster

Galaxy cluster RCS231953+0038.1 was discovered as a significant red-sequence overdensity in RCS-1, located at $z \sim 0.9$. Upon closer inspection, two more significant red-sequence peaks were discovered (RCS232003+0033.5 and RCS231946+0030.6)

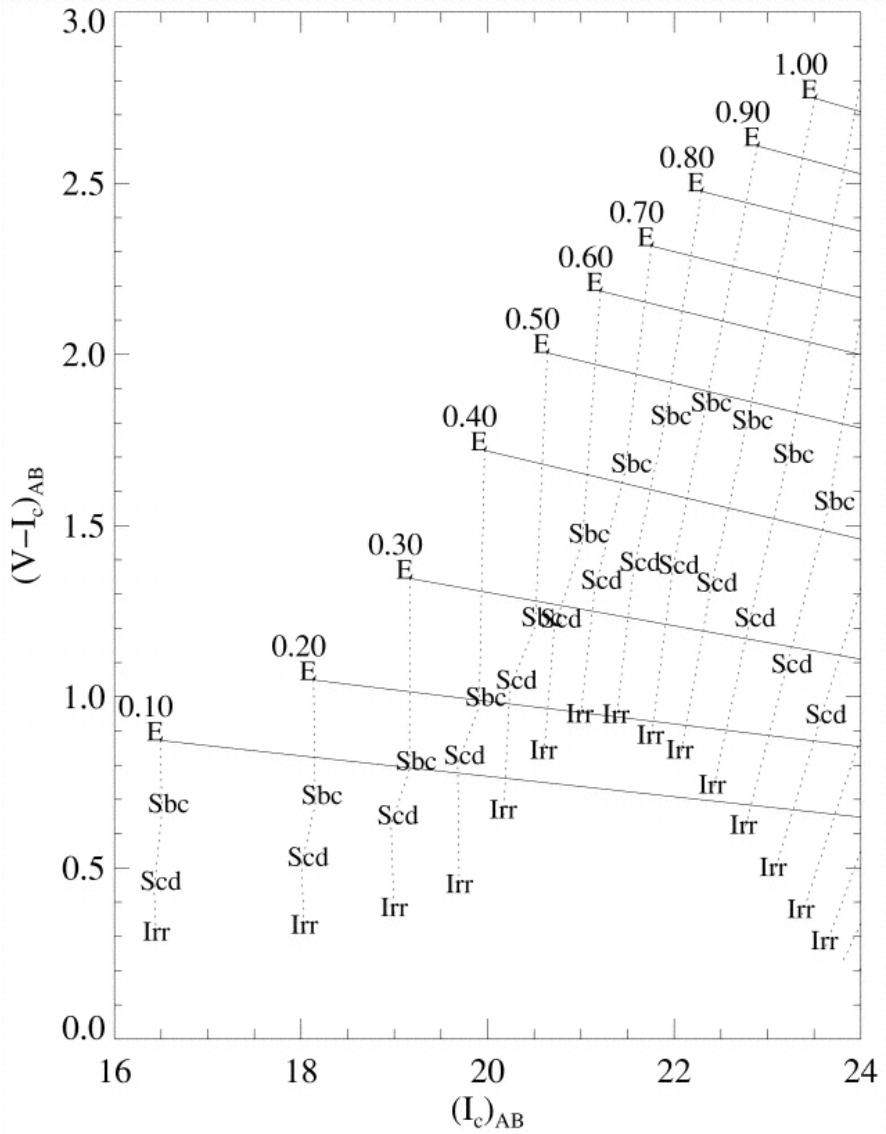

Figure 2.3: Simulated colour−magnitude diagram from Gladders & Yee (2000), indicating the position of the red-sequence with evolving redshift. The dashed lines indicate the different populations for a given redshift, shown from $z = 0.10$, near the bottom, to $z = 1.00$ at top. Of note is the colour, $(V - I_C)_{AB}$ in this case, increasing with increasing redshift, as well as red-sequence overlapping with higher redshift young galaxies rather than foregrounds.

at a similar redshift. Spectroscopy confirmed that the three clusters (designated Cluster A, Cluster B, and Cluster C, respectively) lie at a projected distance of less than 3 Mpc on the sky and a line of sight velocity of 630 km s^{-1}, with cluster spectroscopic redshifts $z = 0.901, 0.905, 0.905$ (Gilbank et al., 2008). Indeed, due to the proximity of the clusters to one another, Gilbank et al. (2008) propose the three will merge by a redshift of $z \sim 0.5$ with a total mass of about $10^{15} M_{\odot}$, comparable to the local universe Coma Cluster.

The supercluster, from here on designated RCS2319, became a target for many multiwavelength campaigns. Additional optical follow-up revealed a significant system of strongly lensed arcs around the core of the most massive cluster, Cluster A (Gladders et al., 2003), as seen in close-up figures of the cluster cores in Chapter 5. X-ray observations from *Chandra* revealed three dense cores of hot gas (see Figure 2.4), resulting in mass estimates $M_{X,tot} \sim 4.7 - 6.4 \times 10^{14} M_{\odot}$ (Hicks et al., 2008). An extensive spectroscopic campaign by Faloon et al. (2013) found over 300 cluster members and revealed a web of infalling groups and extended structure around the clusters. Among these structures was a massive filament bridging between clusters A and B, also found as a submillimetre *Herschel* over-density (Coppin et al., 2012), forming stars at rate of nearly a thousand $M_{\odot} yr^{-1}$. Figure 2.5 shows the red-sequence significance contours from RCS overlaid on an colour image consisting of optical and near-infrared filters g', i', and K_s.

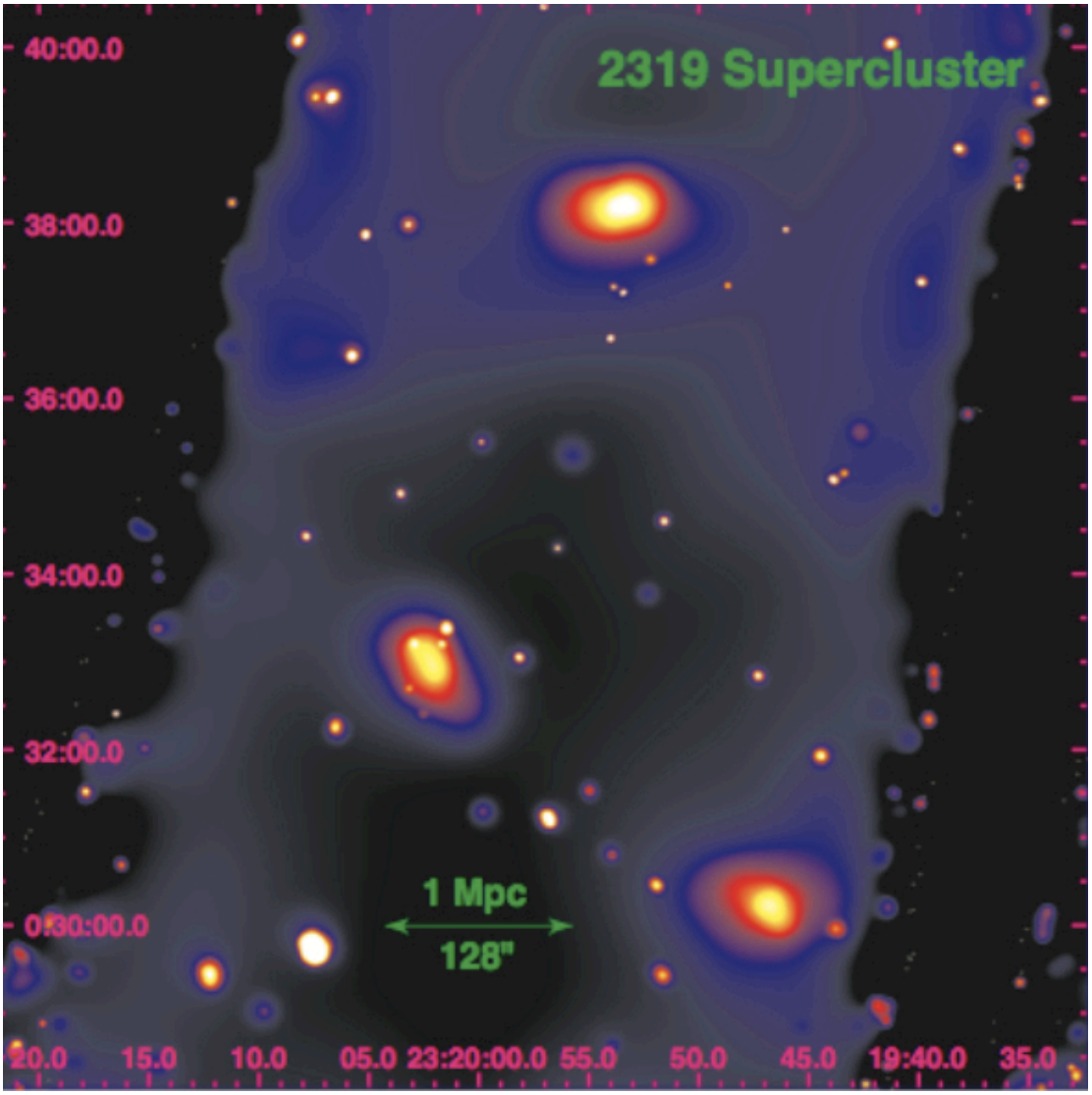

Figure 2.4: *Chandra* observations in the 0.7−3.0 keV band of the RCS2319 supercluster, clearly highlighting the hot X-ray gas component of each individual cluster. Figure taken from Hicks et al. (2008).

Figure 2.5: RGB colour image of RCS2319 supercluster, with filters $g'i'K_s$. The white contours show smoothed red-sequence contours.

2.2.2 *Spitzer* Adaptation of the Red-Sequence Cluster Survey

After the success of the Red-Sequence Cluster Survey, demonstrating the robustness of two-filter wide-field imaging for cluster detections, infrared imaging was incorporated in order to push the identification of clusters out to redshifts beyond $z = 1$. The *Spitzer* Adaptation of the Red-Sequence Cluster Survey (SpARCS) followed the methods outlined in the RCS, but instead of using optical filters to bracket the 4000 Å break, a combination of optical and infrared were used (Muzzin et al., 2009; Wilson et al., 2009). In this case, rather than covering the red side of the break, z' imaging was used for the blue side of the break and the 3.6 μm filter from the Infrared Camera Array (IRAC) on *Spitzer* was selected as the red-ward filter. Wide-field infrared imaging was available from the *Spitzer* Wide-Area Infrared Extragalactic Survey (SWIRE; Lonsdale et al., 2003) over 50 deg^2 across six fields. Deep imaging in z' was taken with MegaCam on the CFHT to cover the four northern SWIRE fields along with MOSAIC-II on CTIO for the southern fields resulting in a SpARCS total area of 42 deg^2, and 28 deg^2 for the northern fields. Similarly to RCS, overdensities of red galaxies can be used to select for galaxy clusters. Instead of using the colour $R_C - z'$, which identifies galaxy clusters up to $z = 1$, the colour $z' - 3.6\mu$m is used which can detect clusters at $z > 1$. Figure 2.6 illustrates how the 4000 Å break of a passive galaxy will move through the filters with increasing redshift, indicating the bandwidths of the R_C, z', and 3.6μm filters.

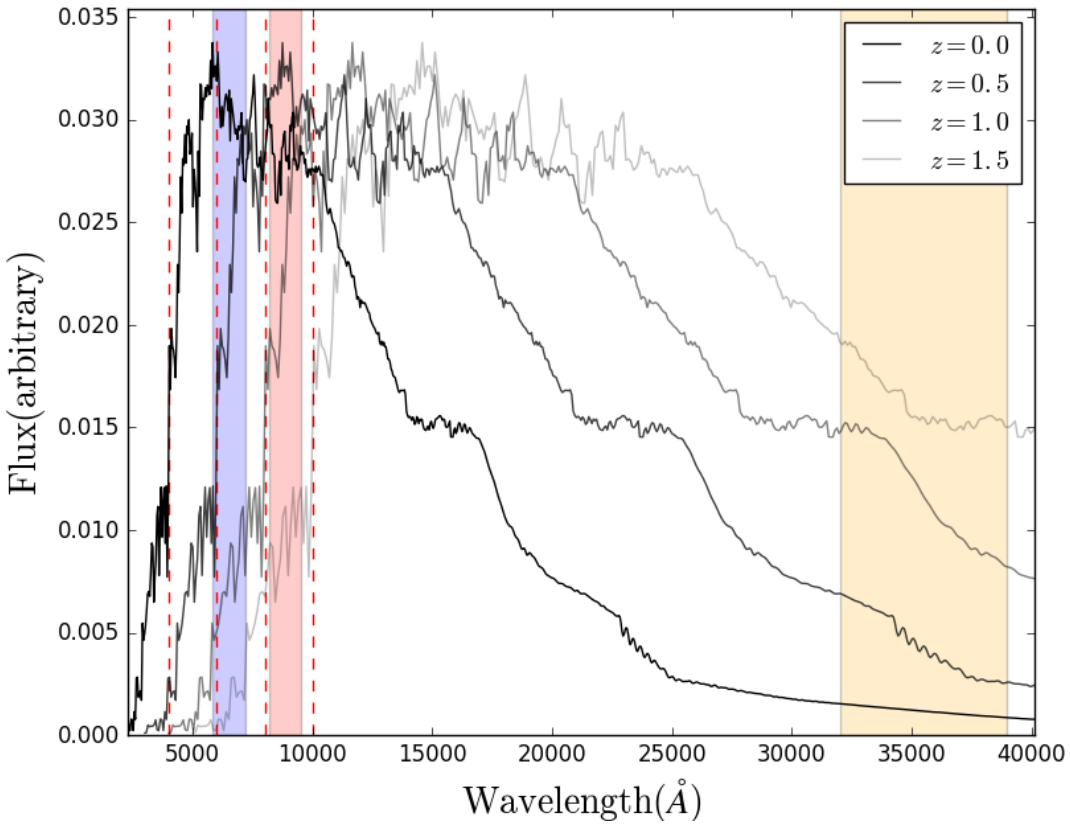

Figure 2.6: The Spectral Energy Distribution (SED) of a passive galaxy as seen at different redshifts, from 0 to 2. The dashed red lines indicate the positions of the 4000 Å break as moves with redshift. The shaded boxes indicate the approximate filter bandwidths for R_C (blue), z' (red), and 3.6μm (orange). At a redshift of 1.5, the 4000 Å break is redward of the z' filter and is now bracketed by 3.6 μm on the red side.

Discovery of SpARCS1049

SpARCS104922.6+564032.5 (hereafter SpARCS1049) is a massive, high-redshift galaxy cluster discovered in SpARCS and presented in Webb et al. (2015a). SpARCS1049, located at a redshift of $z = 1.7$, is noted for its extremely high star-forming brightest cluster galaxy (BCG) which, contrary to previous theories, suggests that wet (star-forming) merging may be an important factor in BCG evolution at early redshifts. Richness estimates based on galaxy overdensity suggest a cluster mass of up to several times $10^{14}M_{\odot}$, a significant cluster and among the most massive discovered at these redshifts to date.

The discovery of the massive cluster prompted a wealth of multiwavelength follow-up, including near-infrared *HST*, submillimetre from the James Clerk Maxwell Telescope (JCMT), and spectroscopy from KECK (as described in Webb et al., 2015a). Figure 2.7 shows the central region of SpARCS1049 in a two-filter composite in the *HST* filters F105W and F160W. The positions of the BCG and foreground spectroscopic interlopers are indicated by the green and red cross-hairs, respectively, with spectroscopic members indicated with green circles.

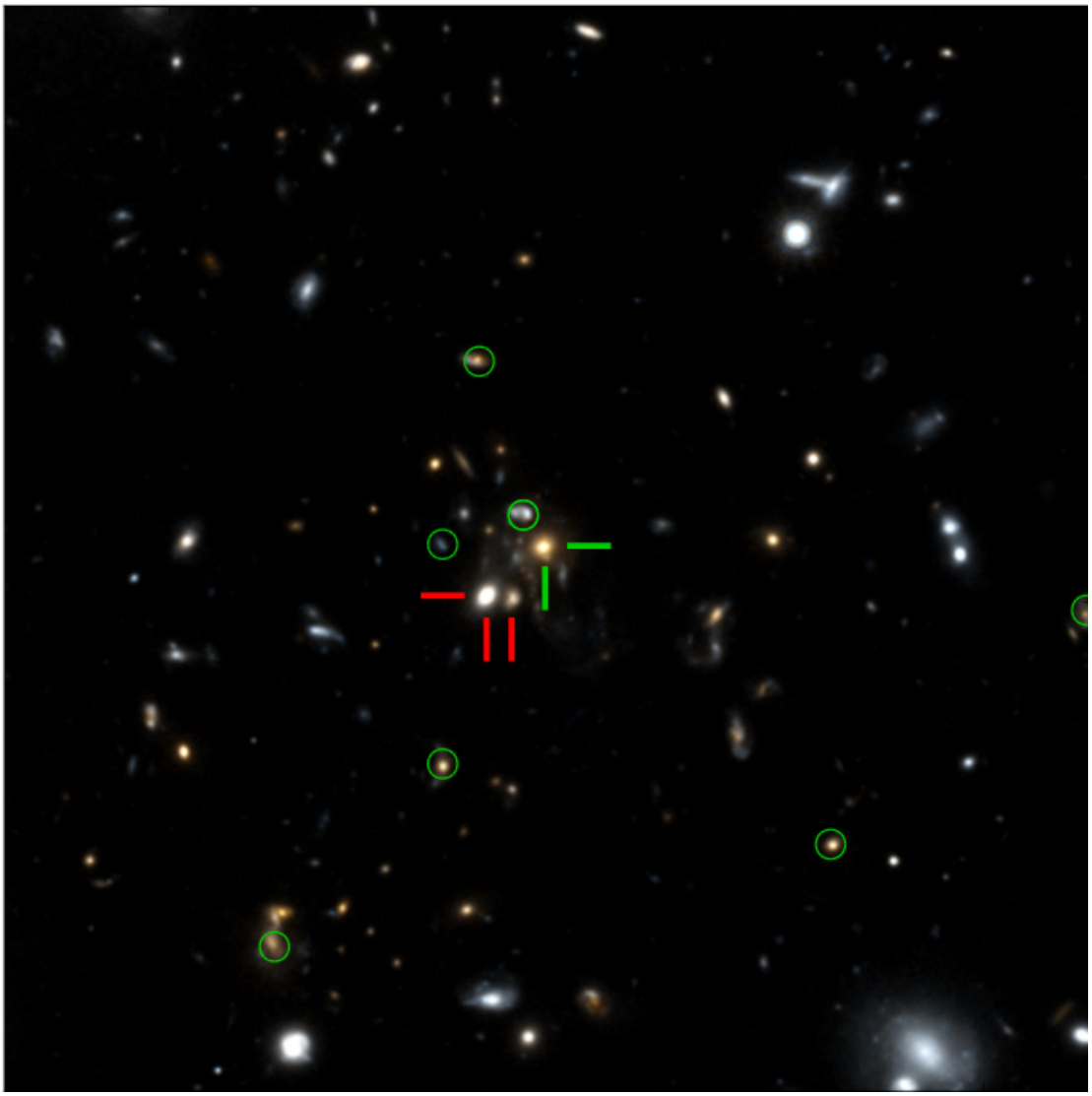

Figure 2.7: Pseudo-colour image of central $1' \times 1'$ region of SpARCS1049 in *HST* filters F105W and F160W. The BCG is indicated by the green cross-hairs, spectroscopic non-members in red cross-hairs, and spectroscopic cluster members in green circles.

3

Data Reduction and Calibration of Optical and Near-Infrared Imaging

The following chapter describes the imaging data acquired for RCS2319 and SpARCS1049 and the ensuing reduction and calibrations done on the multiwavelength dataset.

3.1 Observations from the Red-Sequence Cluster Survey

Imaging and catalogues for all RCS identified clusters were available in filters R_C and z' as part of the RCS release (Gladders & Yee, 2005). Additional unprocessed observations in optical and near-infrared wavelengths were taken for a sample of RCS clusters (see Appendix), including RCS2319, with the MegaCam and WIRCam instruments, respectively, both on the Canada-France-Hawaii Telescope (CFHT). Additional follow-up observations included infrared imaging and catalogues from *Spitzer* in the four filters of the Infrared Array Camera (IRAC; 3.6 μm, 4.5 μm, 5.8 μm, and 8.0 μm) (Webb et al., 2013).

The RCS2319 supercluster also had extensive spectroscopic observations that yielded confident redshifts for approximately 2400 objects, including several hundred confirmed cluster members (Faloon et al., 2013). Figure 3.1 shows the field surrounding RCS2319, highlighting the positions of X-ray detected contours of the three cluster cores, and indicating the fields of view for each instrument (MegaCam, WIRCam, and IRAC). The R_C and z' images from RCS cover the whole field and the spectroscopic survey covers approximately the same area as WIRCam (blue dashed line in Fig. 3.1).

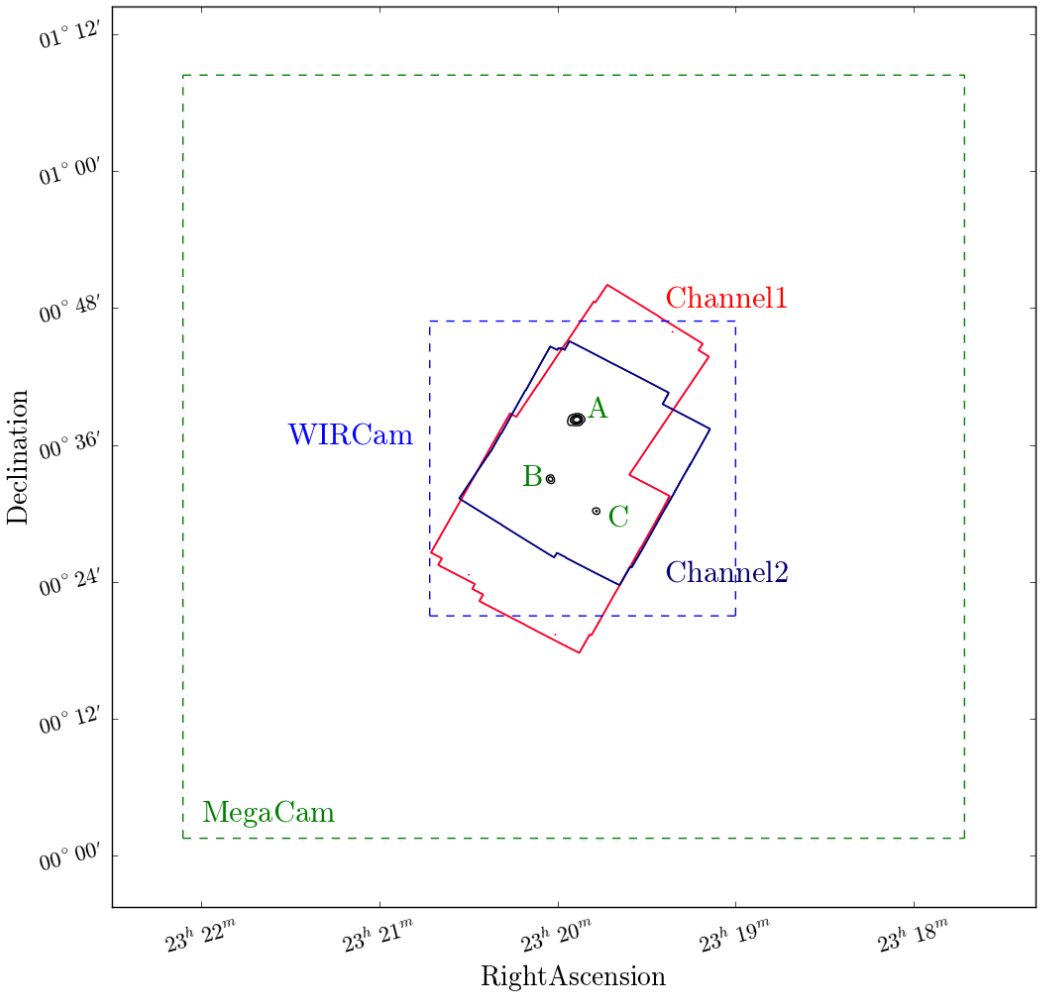

Figure 3.1: Instrument coverage of all data sets for RCS2319. The green dashed line indicates the MegaCam field-of-view, blue dashed line shows WIRCam, the red solid line is IRAC Channel 1 and the solid blue line is IRAC Channel 2. Overlaid are X-ray contours of the three cluster cores with their corresponding names.

3.2 Data Acquisition and Reduction

Observations in the optical filters (g' and i') were taken with MegaCam, located on the CFHT. In all observations, the exposures were taken with moderate dithering so as to cover the small chip-to-chip gaps but not the larger row-to-row gaps. The total field-of-view covers approximately 1 square degree. Observations of RCS2319 in g' and i' were taken in 2010 with total exposure times of 1440 s and 8.1 ks, respectively, with 6 and 27 individual exposures each. As the target cluster galaxies are expected to be quite faint in the bluer filters, a shorter integration time in g' can be used in order to identify brighter foreground galaxies. The deeper i' exposures, which overlap with the observed wavelength of the 4000Å break as $z = 0.9$, are necessary in order to better characterize the break for determining photometric redshifts of cluster members.

Near-infrared observations of the clusters were taken with the Wide-field Infrared Camera (WIRCam) on the CFHT in the J and K_s filters, with a subset having additional imaging in H (see Appendix). Observations of RCS2319 in J and K_s were done in 2010 with total exposure times of 960s and 600s, respectively, and were dithered to cover the chip-to-chip gaps.

Initial processing of the WIRCam data was carried out by the 'I'iwi pipeline at CFHT[*]. This reduction included dark subtractions, flat field corrections, bad pixel masking, and sky subtractions. Similarly, the MegaCam data were preprocessed by the Elixir[†] pipeline at CFHT, applying steps such as flat fielding, bias sub-

[*] http://www.cfht.hawaii.edu/Instruments/Imaging/WIRCam/IiwiVersion1Doc.html

[†] http://www.cfht.hawaii.edu/Instruments/Imaging/MegaPrime/dataprocessing.html

traction, and bad pixel masking. The preprocessing removes variance from chip to chip and ensures uniformity across the entire focal plane. Additionally, the data reduction centre Terapix[‡] specializes in processing large amounts of astronomical data from wide-field surveys and provides resources for reducing imager data for many instruments, including both WIRCam and MegaCam, for which it was originally designed. First order corrections are provided for astrometry and photometry; however, more refined processing is required.

After the preprocessing by Elixir, the MegaCam data were received as multi-extension fits (MEF) files with 36 extensions − one for each CCD. Headers containing a first-order focal plane model for the each of the MegaCam chips' positions were provided by Terapix. We then ran each individual exposure through the image co-addition software SWarp[§], which resamples and places each chip according to the header information. The output from SWarp was a single exposure containing the entire square-degree field of 36 CCDs and allowed astrometric corrections to be done with the entire array as one focal plane, rather than trying to fit each of the 36 chips individually. After initial chip placement, we normalized the flux of each observation by its exposure time.

The preprocessed WIRCam data from the 'I'iwi pipeline were also provided as MEF files. They were then split into their four respective chips (compared to the 36 chips from MegaCam) with some additionally split into subexposures. With only four chips per exposure the initial SWarp run for chip placement, as done for the MegaCam exposures, was not necessary, as astrometric calibrations

[‡] http://terapix.iap.fr/
[§] http://www.astromatic.net/software/swarp

could be done accurately on a chip-to-chip basis. As with the MegaCam data, all observations had their flux levels normalized by their respective exposure times before further calibrations.

3.2.1 Weight Maps

The locations of bad pixels for MegaCam were also provided by Terapix, as text files describing the columns and edges that need to be masked out. From these files combined with the individual chip header information, we constructed full-field weight maps. The weight maps had values of either 1 or 0 and are multiplied by the input source images during combination, thus the masked pixels will contribute zero flux to the final coadded image.

For some cases in the longer exposure MegaCam data, satellite trails of varying brightness were visible. In the most noticeable cases, the weight maps were edited to additionally mask out the trail for the individual exposure.

For WIRCam, bad pixels and regions as well as bright stars were masked out in the preprocessed data. The weight maps were thus extracted from the frames themselves, copied as an array equal to zero wherever the input is zero, and one everywhere else.

3.3 Astrometry

Accurate astrometry is essential when dealing with any imaging, but especially important when dealing with large fields-of-view where distortions can be signifi-

cant across the focal plane. For most source matching, a threshold of less than an arcsecond offset is required. Precise astrometry is crucial in the cases of follow-up observations, such as slit spectroscopy, where offsets larger than an arcsecond can result in missing sources entirely. Figure 3.2 shows an inset of four MegaCam images coadded together without any additional astrometric corrections applied. The relative shift between the exposures causes a 'doubling' effect, smearing out sources. Figure 3.3 compares an uncorrected MegaCam exposure against bright SDSS sources indicating the absolute offsets that occur without precise astrometry. The offsets shown in Figure 3.3 are approximately 11″, far above the optimal sub-arcsecond offset and is not adequate for source matching.

Astrometric corrections are typically done by comparing sources from the observations against a calibrated catalogue of known sources and deriving the necessary offsets, rotations, and shear required to align the world coordinate system (WCS). For both WIRCam and MegaCam, the astrometric solutions were performed using the Software for Calibrating AstroMetry and Photometry (SCAMP)[¶]. SCAMP, along with SWarp, was developed by the Terapix team originally for the reduction of MegaCam and WIRCam imaging.

Bright objects were extracted from each image using SExtractor[‖] by requiring a high threshold for detection. The catalogue, consisting of high signal-to-noise sources, was output as binary FITS LDAC file and contained parameters such as positions, positional uncertainty, fluxes, and quality flags. For observations of RCS2319, the calibrated reference catalogue selected for WIRCam was the 2

[¶] http://www.astromatic.net/software/scamp
[‖] http://www.astromatic.net/software/sextractor

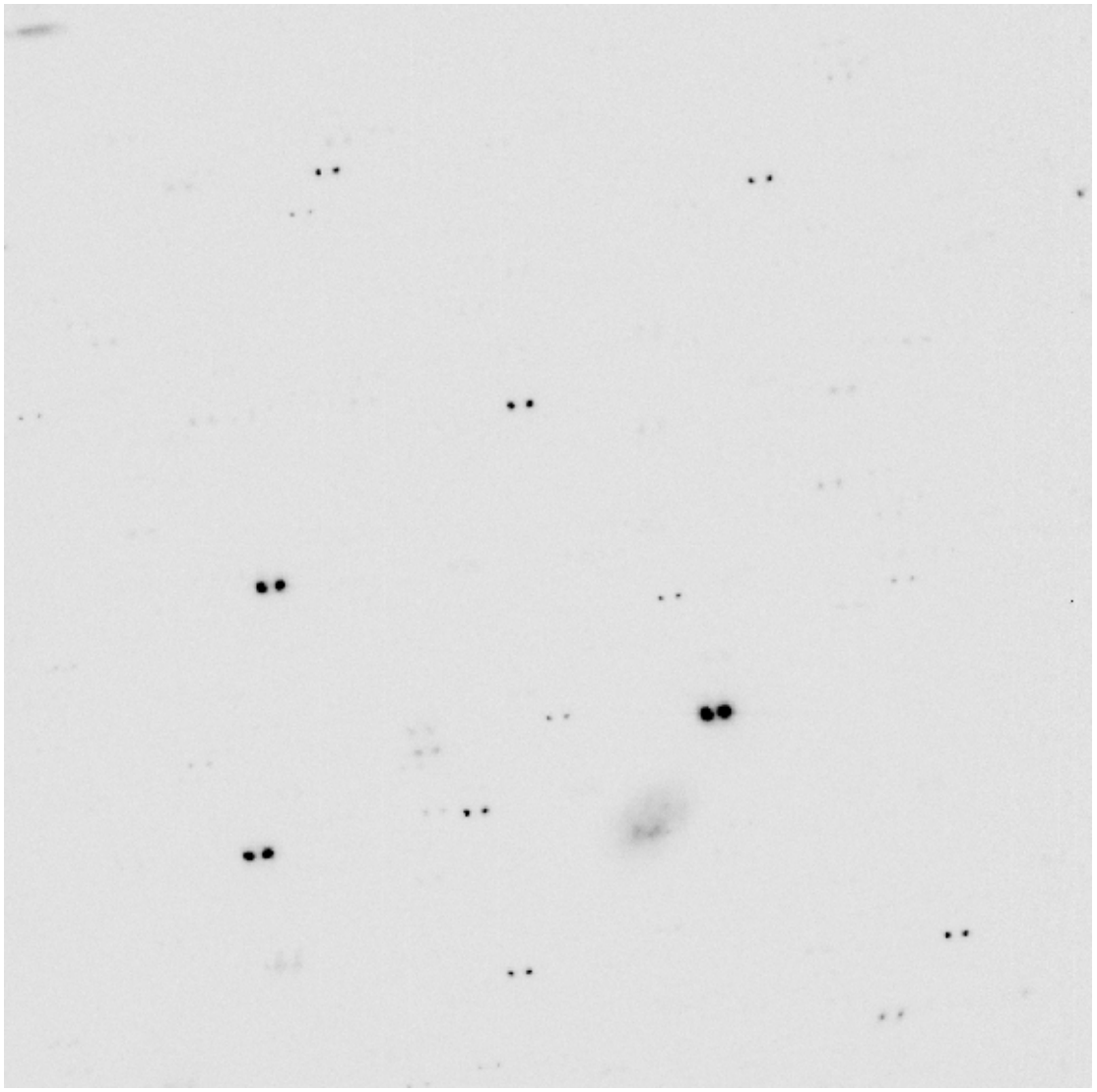

Figure 3.2: A small inset of MegaCam (approximately $105'' \times 105''$) illustrating the 'doubling' and blurring that occurs when multiple exposures that have not been correctly aligned are stacked.

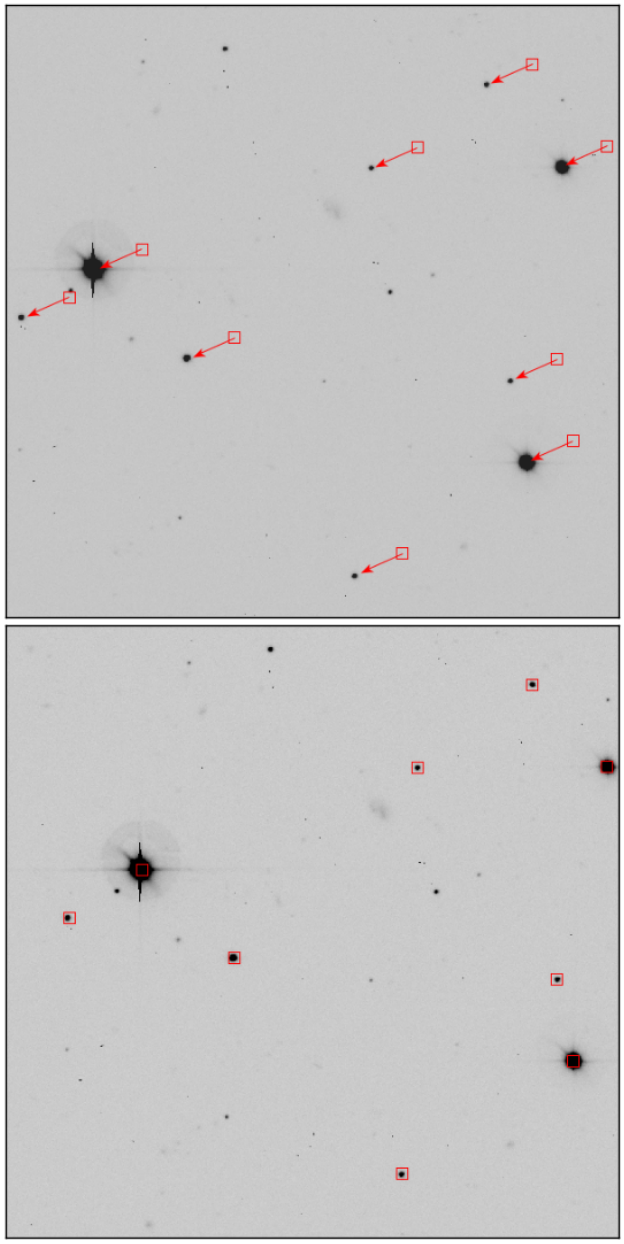

Figure 3.3: *Top:* A $2' \times 2'$ inset of a MegaCam exposure highlighting the offset from SDSS (red squares). At this region of the focal plane the offset is nearly $11''$ although it can vary across the whole field. *Bottom:* Same field after being calibrated against SDSS with SCAMP and run through SWarp.

Micron All-Sky Survey (2MASS) and for MegaCam the sixth data release of the Sloan Digital Sky Survey (SDSS) was used. Filter selection was also available for the reference catalogues; exact filters were used since the CFHT has matched filters to SDSS and 2MASS.

FITS catalogues containing the source information from SExtractor were passed into SCAMP and matched to the selected reference catalogue. SCAMP would flag exposures that had poor matches between the input and reference catalogues, resulting in higher chances of inaccurate projections. Generally this was rectified by placing tighter restraints on the reference objects used such as implementing a magnitude cut, thus only including bright, high signal-to-noise sources. Using a χ^2 minimization routine of positional differences between matched sources, SCAMP solved for pixel scale, offsets, position angle, and focal plane distortion. To correct for the shear distortion, which can be significant across the square degree field of MegaCam, a fifth order polynomial correction was determined for both WIRCam and MegaCam. For each exposure, SCAMP output a header that contain the necessary astrometric transformations required to align the world coordinate system (WCS), including positional offset and higher order shearing.

The exposures were coadded and mosaicked together using SWarp, an image combination program that is designed to be used in conjunction with SCAMP astrometric solutions. Each individual exposure was read in with its corresponding header produced by SCAMP along with the weight map that masked out chip gaps and bad pixels. The final image pixel scale was set to the median scale of all input images and was centred so that all input images fit in the final field-

of-view. Each input frame was regridded to the final pixel scale and size, with nearest neighbour interpolation used between pixels. The background was subtracted using a background map produced by iteratively determining the average background across the entire field in $n \times n$ grids, where typically $n = 128$ pixels was used. Using a map instead of a single background value corrects for variability across the field, and the size of the mesh was selected to be large enough to sample enough background region without source contamination while being small enough to still reproduce variability.

Once all input images had been background subtracted and resampled, they were coadded together into the final image. The median value of each pixel was used during combination, with pixels masked by the weight maps not contributing any flux. The bottom plot in Figure 3.3 shows an inset of a final astrometrically calibrated and coadded image compared to the SDSS reference catalogue. A resampled weight map corresponding to the density of overlapping frames in the final mosaicked image was also produced by SWarp.

3.3.1 Follow-up Observations to SpARCS1049

Optical catalogues obtained from MegaCam for SpARCS1049 were available as part of a SpARCS follow-up program (A. Tudorica, submitted). Unfortunately, due to the chip placement, a substantial fraction of the cluster core is not covered by the z' filter as shown in Figure 3.4. As z' provides the blue-ward edge of the 4000Å break for the high-redshift clusters, the lack of z' magnitude information in the gap prevents the identification of cluster members via photometric redshift.

Thus additional z' observations were requested to complete the catalogue.

The z observations (since updated from the z' filter) were taken in December 2015. The reduction followed the same steps as the RCS observations, with the exception of the 4 'wing' chips now being present on the focal plane. The original focal plane map was still used with the wings adjusted manually to align. Astrometric calibrations were done with SCAMP and SDSS was used for the reference catalogue. Finally mosaicking was done with SWarp and the corresponding SCAMP headers.

3.4 Photometry

3.4.1 PSF Matching

The point spread function (PSF) describes the light profile of a point-like source as it is observed by the detector. Many things affect the PSF such as the telescope optics, the instrument, the individual filter, the astronomical seeing, and the airmass at the time of the observation. The PSF can vary throughout a single set of observations or across the detectors. In the cases of aperture photometry, where a set aperture is placed over each source and the light within that aperture is measured, different PSFs will cause different fractions of the source's flux to be measured. In an optimal photometric dataset, PSFs will be consistent across all filters, or at least for filters in neighbouring wavelengths. As the PSF will likely vary from filter to filter, optimizing the uniformity of the data and thus the photometric redshift estimations requires characterizing the PSFs for each final

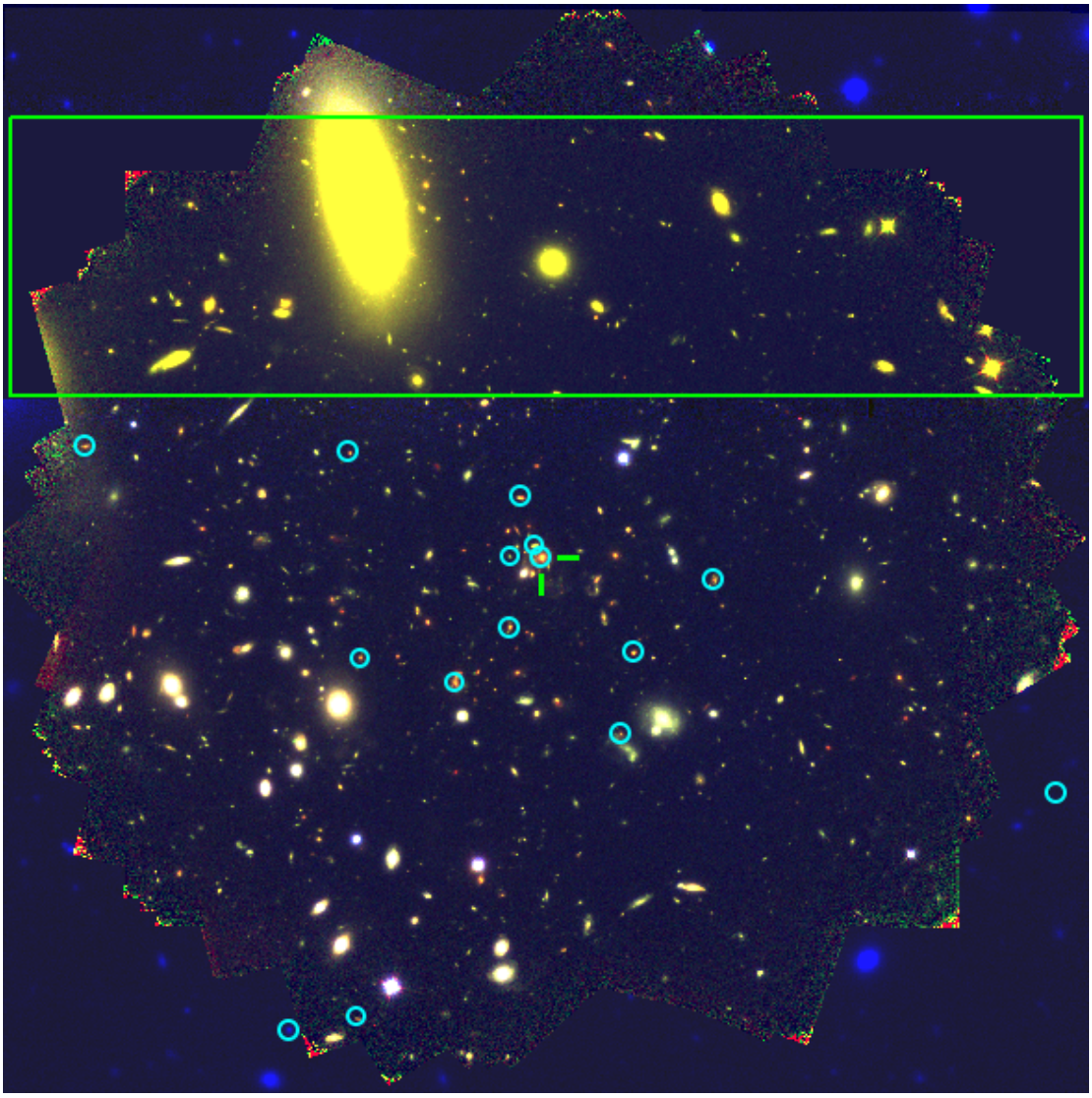

Figure 3.4: Three colour *HST*+ CFHT (F160W + F105W + z') image showing the central $2' \times 2'$ region of cluster SpARCS1049. The cyan circles indicate spectroscopically confirmed cluster members with the brightest cluster galaxy indicated by the green ticks. The green rectangle indicates the chip gap in the z' observations, making it difficult to identify cluster members in that region via photometric redshift.

image and convolving the image to match the one with the largest PSF, before catalogue extraction.

The PSF is typically measured by stacking isolated and unsaturated stars, which represent point sources illuminating the detector. In a clean image, stars can be readily identified by plotting the magnitude or flux of all sources as function of their radius. In Figure 3.5, this has been shown for all sources of the g' image, highlighting the different types of sources. The stars are selected from the vertical locus, highlighted in green in Figure 3.5. Extended sources are typically galaxies, sources smaller than stars are typically cosmic rays, and the turn off of the stellar locus at the bright end is due to saturated sources.

To measure the PSF for each CFHT observation, SExtractor was run on each image selecting for bright, high signal-to-noise sources. Point sources were selected following the size-magnitude relation illustrated in Figure 3.5. Further refinements are made by selecting the brightest sources that have not reached saturation as well as selecting for low ellipticity. Each source was individually inspected on its corresponding image, ensuring that the source is far from chip edges and has no near neighbours. The final selection of point sources to be stacked ranged from twenty to fifty objects for each of the images (g', i', J, and K_s). Sources were stacked using the IDL code `make_psf.pro` which selects clean sources from an imported list and produces an averaged PSF. The output PSFs can then be compared to one another, and in the cases of strongly dissimilar PSFs the necessary convolution kernels can be determined in order to convolve all images to the same PSF.

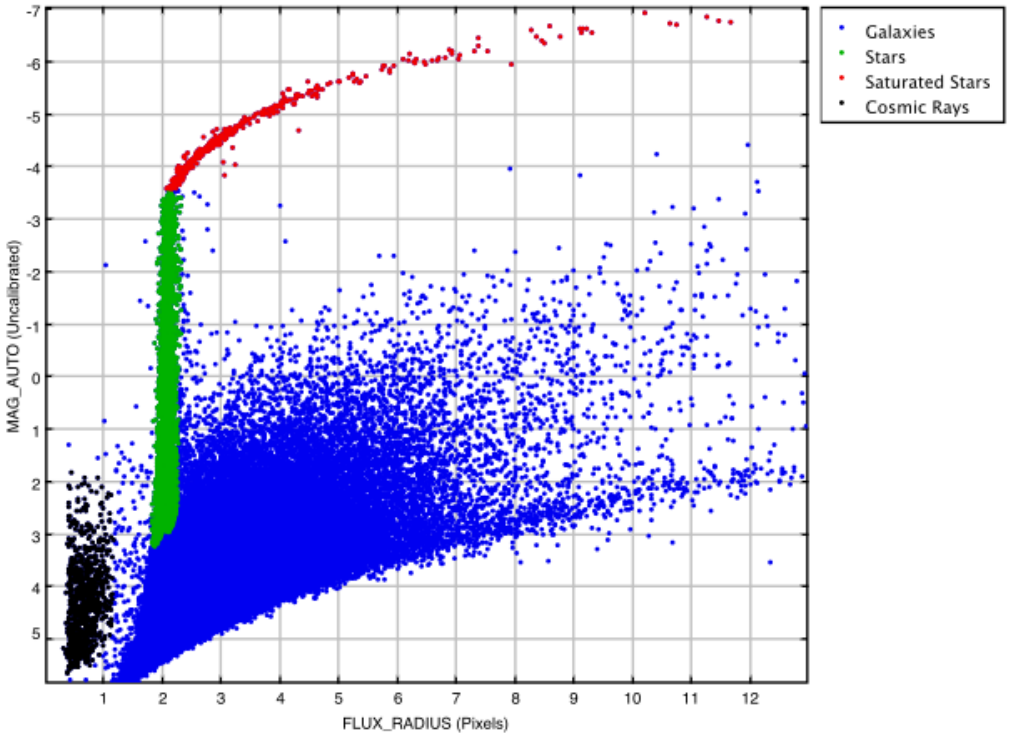

Figure 3.5: The size-magnitude relation for sources in the MegaCam g-band image, where the magnitude is arbitrary (pre-calibration) and the flux radius represents the approximate half-light radius for sources. The different source regions have been indicated by different colours. The point sources (stars) lie along the mostly vertical locus (in green), where the physical size of the source on the detector is independent of the flux of the object. Beyond a certain flux, the stars become saturated and begin to spread across more pixels as flux increases (indicated in red). Black sources indicate cosmic rays which are faint and typically only illuminate one pixel. All other sources are typically due to galaxies.

For the MegaCam observations, PSF convolution was deemed unnecessary due to both the similarity of the g' and i' PSFs (see Figure 3.6), and the extreme variance across the field-of-view for the R_C and z' observations. The CFH12K camera that was used for the R_C and z' observations as part of RCS had different chip-to-chip responses, making it difficult to ensure uniformity across all four optical filters. The size−magnitude of the R_C observation is shown in Figure 3.7, exhibiting extreme chip-to-chip variations of the PSF with no clear locus for stellar sources or the turn off for saturated sources. The calibrations of the CFH12K images were done as part of the RCS in Gladders & Yee (2005) where great care was taken to correct for all the variations and inconsistencies across the observations. Thus the magnitudes from the RCS catalogue are sufficient for our purposes, and although some offsets due to PSFs may be required, this can be alleviated during the photometric redshift calculations, detailed in Chapter 4.

Unlike the optical observations' similar PSFs, the near-infrared observations had markedly different PSFs, requiring convolution. The J-band observations had a significantly wider PSF than the K_s-band, as seen in the first two plots in Figure 3.8. Convolution kernels were produced using the Image Reduction and Analysis Facility (IRAF Tody, 1986), which contains a wide array of tasks for astronomical data. The task `psfmatch` within the `images.immatch` package was used to compute and apply convolution kernels. The task was first run with the K_s PSF as an input image and the J PSF as a reference. The mode was set to output a kernel that convolves the input PSF into the reference PSF.

After the kernel was produced, `psfmatch` was run again in convolution mode,

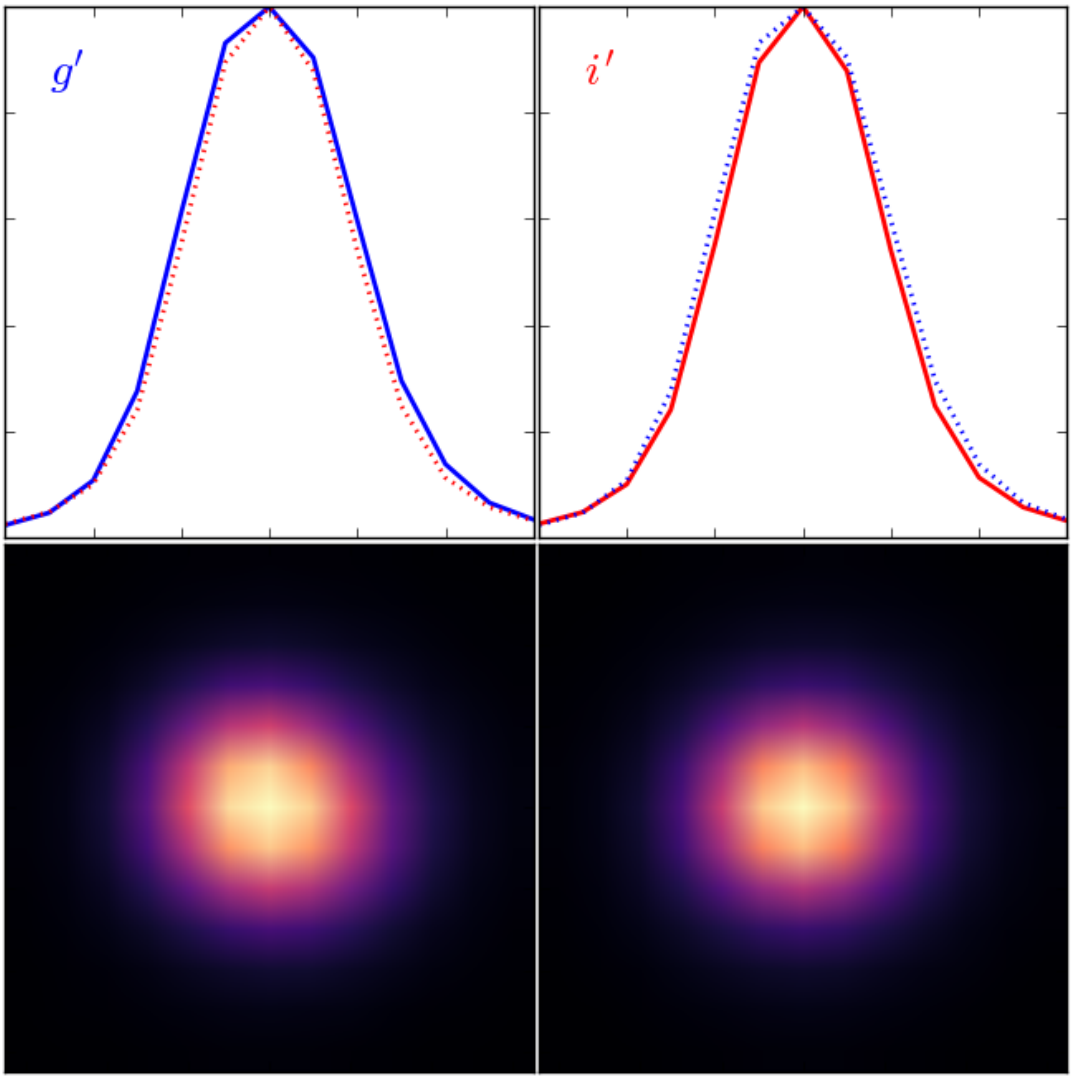

Figure 3.6: The PSFs of optical imaging in g' and i', derived from a set of stacked unsaturated stars. The bottom images show the 2D PSF and the top plots show the normalized 1D PSF. The PSF for the indicated filter is shown as the solid line, with the PSF of the other filter indicated by the dotted line. The PSFs are similar enough that convolution matching is not necessary.

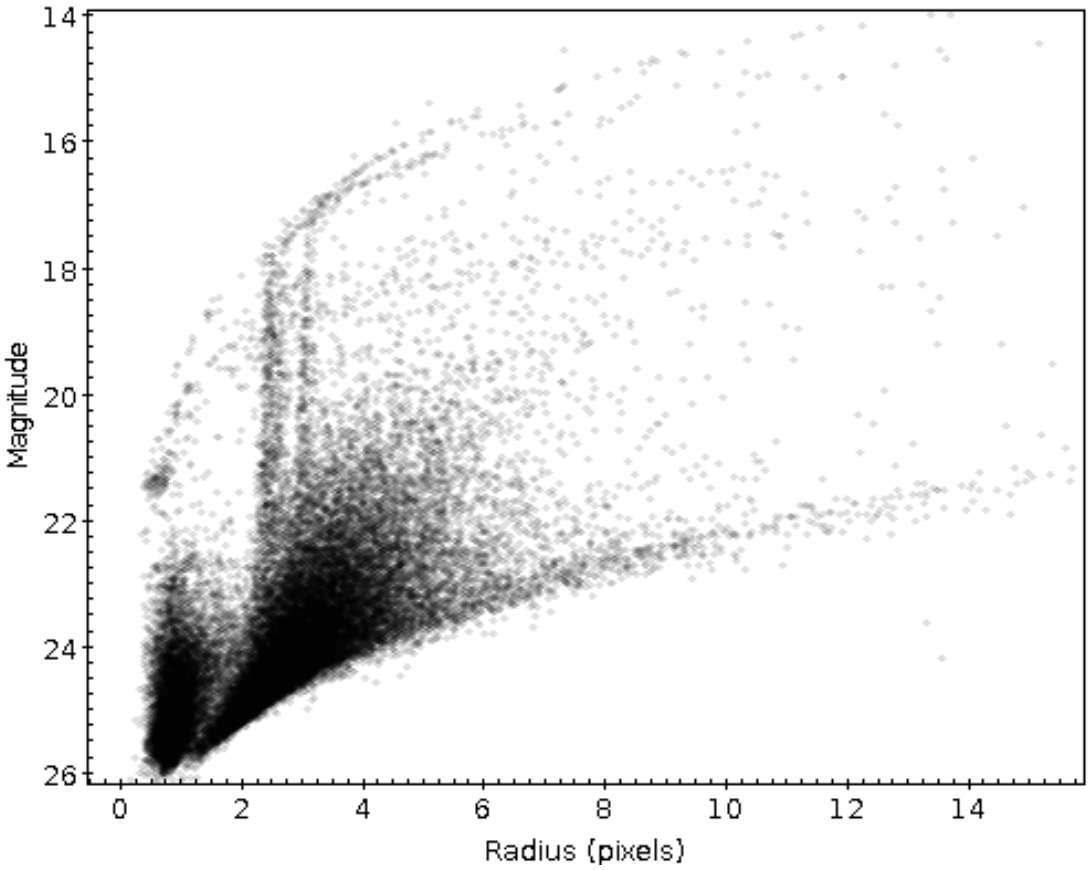

Figure 3.7: Size−magnitude relation for sources in the R_C-band image from the CFH12K camera, similar to Figure 3.5. As opposed to the g-band image where the different classes of sources can be easily separated, the chip-to-chip variations of the CFH12K camera are clearly evident here with multiple tracks for point sources and saturated sources. This variance inhibits the ability to perform clean PSF matching.

with the original K_s image and matched kernel as inputs. The output image should thus have the same PSF as the original reference, in this case the J band PSF. Figures 3.8 and 3.9 show the results of the convolution. Figure 3.8 shows the 1D and 2D PSFs of all three images (original K_s, J, and convolved K_s). The lower panels show the 2D PSFs, of which the K_s and J were used to calculate the convolution kernel. The PSFs are zoomed in to highlight the size difference between J and K_s; the PSFs used for kernel production were large enough that the wings dropped to 0. The top panels show all three 1D PSFs, with the corresponding filter in bold and the other two in dotted lines. It is clear from the top panels that the original K_s image had a significantly smaller PSF than the J, whereas the PSFs became nearly identical post-convolution. Figure 3.9 similarly illustrates that point sources of the J and convolved K_s images now lie along the stellar locus in flux−radius space. Figure 3.9 is similar to 3.5 with the exception that the intensity is measured in flux instead of magnitude (linear instead of logarithmic), with stellar sources still lying along a vertical line. From here on, all references to K_s imaging refer to the convolved image.

3.4.2 Calibrations

Absolute photometric calibrations are done by comparing offsets between magnitudes in source catalogues and reference catalogues. Fortunately the filter shapes and responses of MegaCam and WIRCam closely match those of SDSS and 2MASS, respectively. The optical data (g' and i') were thus calibrated against the SDSS Data Release 12 (Alam et al., 2015) and the infrared data (J and K_s) were

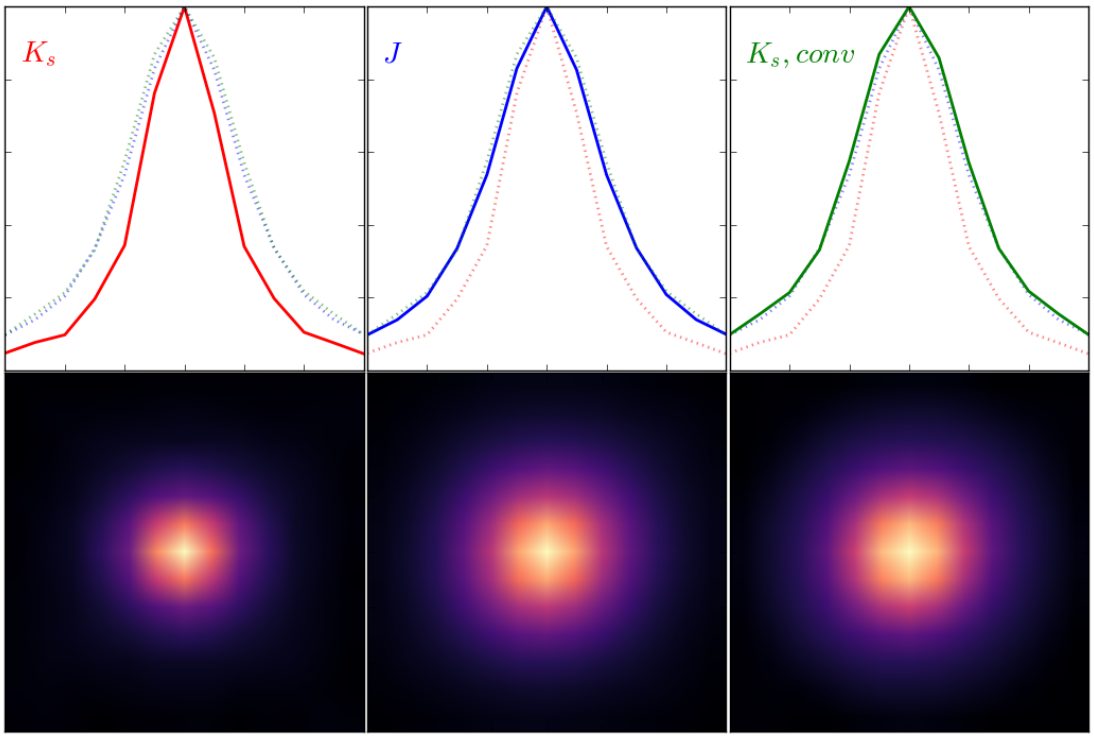

Figure 3.8: PSFs of near-infrared imaging in K_s, J, and J-matched convolved K_s. The plots are same as Figure 3.6, with the bottom images showing the stacked PSFs for each filter and the top plots show the normalized 1D PSFs. The PSF for each indicated filter is shown as the solid line, with the other two PSFs indicated by the dotted lines. Of note is the significantly narrower K_s PSF before convolution, whereas the J and convolved K_s PSFs overlap with one another, as is the goal for PSF convolution.

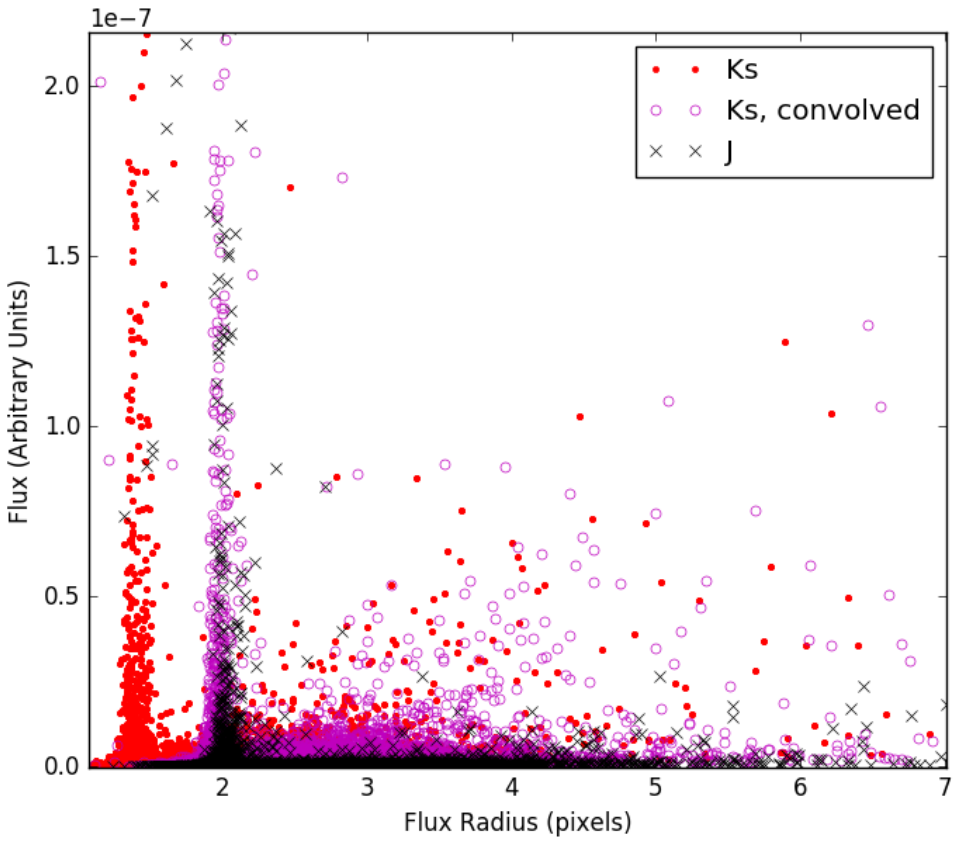

Figure 3.9: Flux vs. Flux Radius measurements for near-infrared data, where flux is arbitrarily scaled. The tight columns of sources indicate point sources (stars), the radius at which it is centred correlated with the width of the PSF. The offset between the J and K_s sources highlight the broader PSF of the J imaging, which is consistent once the K_s imaging has been convolved to match the J imaging PSF.

calibrated against 2MASS (Skrutskie et al., 2006).

Sources from the CFHT images were extracted with SExtractor, weighted according to the exposure overlap produced by SWarp. For calibrations, aperture photometry was done using 3″ apertures for MegaCam and 4″ for WIRCam to best match to the reference catalogues. These were then matched to the corresponding references catalogues with a 1″ match radius required. The weighted median difference between the source and reference catalogues was determined for stellar objects after one iteration of removing outliers. The calculated offset was then applied to the source catalogues to shift them to the corresponding magnitude system, as $m_{cal} = m_{obs} + (m_{ref} - m_{obs})_{med}$. SDSS is on the AB magnitude system, where each filter has the same zeropoint such that spectral flux density in different filters is the same for the same magnitude. 2MASS is on the Vega magnitude system where the filter zeropoints are different for each filter, so for uniformity the WIRCam catalogues were shifted onto the AB system; an offset of $+0.91$ was applied to the J magnitudes and $+1.85$ to the K_s magnitudes, following the conversions from Blanton & Roweis (2007).

After reduction and calibration, the 5σ limiting magnitudes for points sources are approximately 23.8 and 24.5 for the g' and i' catalogues, respectively. The depths for the infrared data are approximately 21.6 and 21.9 for the J and K_s catalogues, respectively.

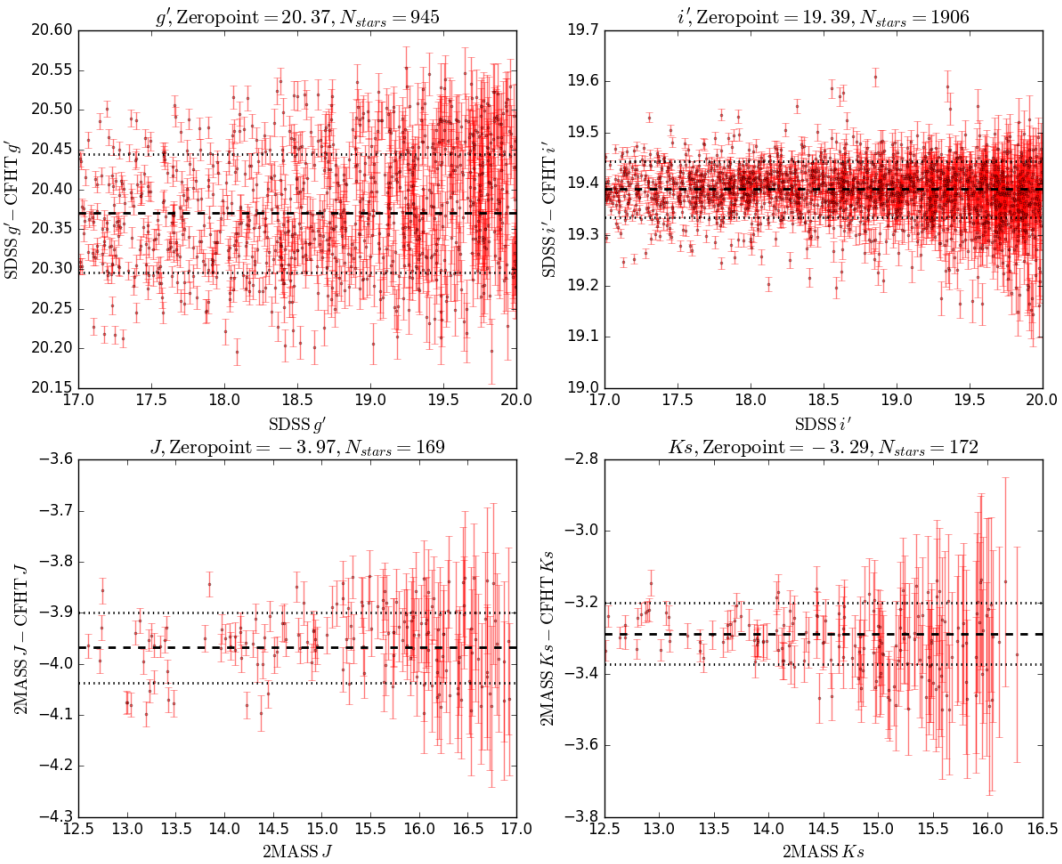

Figure 3.10: Photometric calibration plots, showing the offset from the reference catalogues to the CFHT catalogues. The top two plots show g' and i' calibrated against SDSS, and the bottom show J and K_s calibrated against 2MASS. The weighted median offset is indicated by the dashed lines and the dotted lines indicate the 1σ standard deviation.

4

Photometric Catalogues and Redshifts

This chapter describes the methodologies and techniques used to derive photometric redshifts for large samples, and details the photometric catalogue assembly and subsequent photometric redshift determinations for the galaxy clusters presented in this thesis.

4.1 Photometric Redshift Methodology

Determining distances to astronomical objects is crucial in understanding the sources themselves, especially in the cases of galaxy cluster studies where it's

important to ascertain membership. The most common way to estimate distance is measuring the redshift, either by spectroscopy or photometry. Both methods have advantages and disadvantages, with the differences generally resulting in a trade off between accuracy and time requirements.

Spectroscopic redshifts are determined by measuring the wavelength shift of spectral features, either emission or absorption, with respect to reference wavelengths. This method is highly accurate, especially in the case of emission spectra, but it can be very costly to obtain the data for a large number of sources. The advent of multi-object spectrometers has enabled the simultaneous spectroscopic observation of tens to hundreds of objects within a single exposure, although multiple masks will still generally be required to map an entire field especially in cases with crowding such as cluster centres. Integration times also steeply increase with faintness (and thus redshift) as less photons are collected per exposure, inhibiting the ability to disperse the spectrum and still see features. Additionally, in the case of galaxy clusters, the populations are known to be populated mostly by quiescent galaxies with little to no active star-formation, thus limiting the ability to identify cluster sources based on bright emission features.

In contrast to spectroscopic redshifts, photometric redshifts readily provide large sample sizes of both quiescent and star-forming sources at a cost of much lower redshift accuracy. Instead of searching for individual features over a narrow region of the galaxy spectrum, photometric redshifts utilize broadband magnitude information from many filters in order to characterize the overall spectral energy distribution (SED) from ultraviolet to infrared. The most common method for

determining photometric redshifts is template fitting, where a library of known galactic SED templates is fit to the input photometry allowing redshift to vary, with the photometric redshift being the one that reduces the χ^2 fit between the data and template. More advanced photometric redshift techniques involves extensive training against a large sample of objects with known spectroscopic redshifts and parametrizing photometry and colours as a function of redshift.

The accuracy of photometric redshifts have been found to depend on both the number and wavelength range of filters, with accuracy increasing with more filters and a longer wavelength range (Bolzonella et al., 2000). Early iterations of photometric code by Bolzonella et al. (2000) found that up to a redshift of $z = 1$, the accuracy of photometric redshifts can improve from $\sigma_z = 0.3$ to $\sigma_z = 0.17$ by incorporating near-infrared magnitudes to 5 band optical photometry. Improvements to photometric redshift methods and the advent of deep multiwavelength surveys have provided an extensive range of filters and coverage enabling the wide employment of accurate photometric redshifts. For example, Dahlen et al. (2013) evaluated photometric redshift results from 11 individual estimations using a 14 filter photometric catalogue from the Cosmic Assembly Near-infrared Deep Extragalactic Survey (CANDELS; Koekemoer et al., 2011). With a variety of templates and photometric redshift methods employed, the redshift accuracy varied from $\sigma = 0.03$ to $\sigma = 0.06$ based on different trials and selection techniques. Even more impressive, the Cosmic Evolution Survey (COSMOS; Scoville et al., 2007) has provided extremely accurate photometric redshifts due to the combination of both broad and narrow filters and coverage from the ultraviolet

to infrared. Utilizing the 30 filters results in photometric accuracies of $\sigma = 0.007$ for the brightest sources and $\sigma = 0.012$ for fainter sources (Ilbert et al., 2009).

4.1.1 EAZY

Easy and Accurate Photo-Zs from Yale (EAZY; Brammer et al., 2008) is a public code designed to calculate photometric redshifts via SED template fitting.

Templates

Two modes of template fitting are available with EAZY - either a single template fit or a simultaneous multiple template fit. In single template fitting mode, typically a large set of SED templates are used that ideally sample all possible galaxy SEDs. Each object's SED is then matched to an individual template that best describes it. While the computational time is short using this method, it is very difficult to assemble a library of all possible SEDs and the high rate of mis-matched SEDs will result in inaccurate photometric redshifts. EAZY thus provides the ability to do linear combinations of templates in order to determine the best fit to the input photometry. Rather than selecting an individual template, a combination template is determined as follows:

$$T_z = \sum_{i=1}^{N_{temp}} \alpha_i T_{z,i}$$

where the best fit template at a given redshift z, will be a combination of all input templates with individually determined coefficients, α_i. A smaller template

set can be used, with a subset that roughly correspond to different SED shapes, from quiescent to starbursting, based on stellar population synthesis models.

Bayesian Prior

EAZY can incorporate the use of a magnitude prior, which is used to break degenerate redshift probabilities (i.e. multi-peaked probabilities) based on the apparent magnitude of the object, as well as taking into account the smaller volume probed at lower redshifts. EAZY provides priors in both the r filter ($\sim$6500Å) and K filter($\sim$ 2.2μm), with the r filter prior shown in Figure 4.1. The prior takes into account redshift volume (lower redshifts are probing smaller volumes) and observed luminosity (very bright objects are unlikely to be high-redshift). In short, objects with a higher apparent brightness are more likely to be found at lower redshifts. In cases where SED features, such as the 4000 Å break and the Lyman alpha break at 912 Å, are fit equally well to the photometry, the magnitude prior can force the degeneracy to be broken based on the observed fluxes. Figure 4.3 in §4.2.1 illustrates the improvement in incorporating a magnitude prior.

Zeropoints

While EAZY does not directly use spectroscopic redshifts for training photometric redshifts, they can be used to estimate individual offsets (zeropoints) for each filter. Using known spectroscopic redshifts, the input photometry can be matched to the best template combination that is set to the spectroscopic redshift and the fluxes are adjusted to ensure the best template fits across the whole sample. This

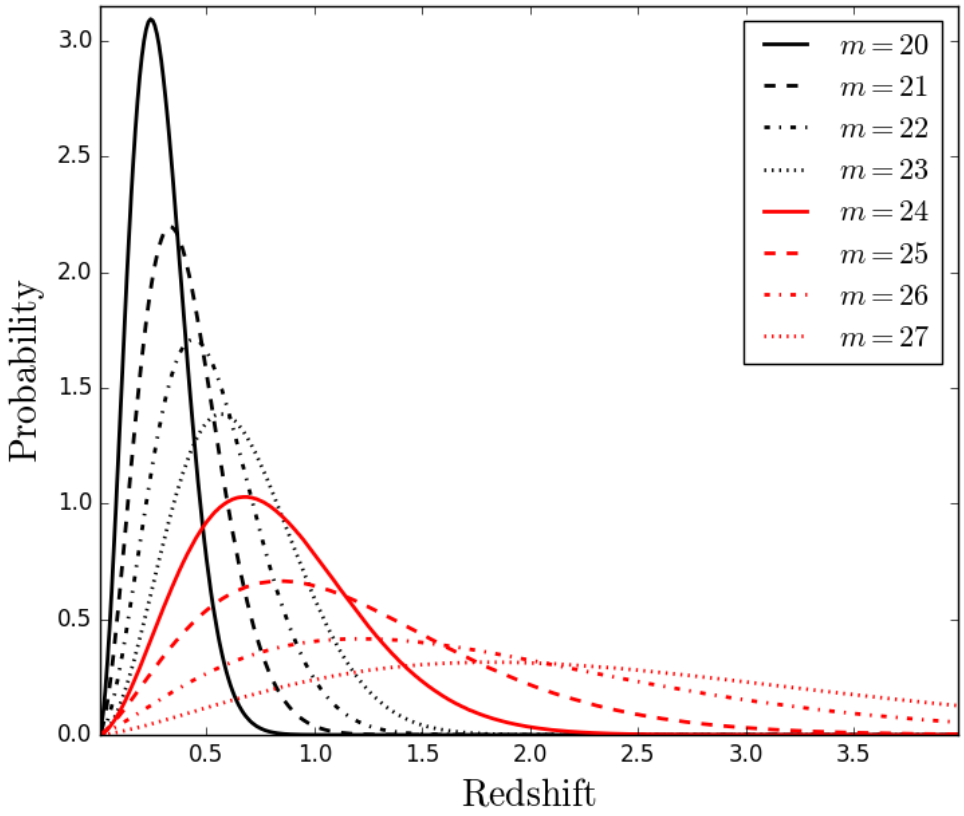

Figure 4.1: Normalized r-band magnitude-redshift prior provided by EAZY (Brammer et al., 2008), for apparent magnitude range $20 < m_r < 27$. The prior uses the magnitude information when determining the most likely photometric redshift. The brighter in r the object is, the more likely it is to be low redshift.

can help alleviate filter-to-filter variations, such as different seeing and PSFs.

Photometric Accuracy and Quality Parameter

Brammer et al. (2008) define a reliability parameter to identify objects where the photometric redshift may be unreliable due to factors such as poor fits to templates, mis-matches to spectroscopic redshift, spurious fluxes, or multiple-peaked probabilities. The quality parameter, Q_z, is defined as:

$$Q_z = \frac{\chi^2}{N_{filt} - 3} \frac{z_{up}^{99} - z_{lo}^{99}}{p_{\Delta z=0.2}}$$

where N_{filt} is the number of filters included in the SED fit, z_{up}^{99} and z_{lo}^{99} are the upper and lower 3σ confidence intervals, $p_{\Delta z=0.2}$ is the integrated probability that the redshift lies within $\pm\Delta z = 0.2$, and χ^2 is the χ^2 statistic of the template fit; all parameters are provided in the EAZY output. Brammer et al. (2008) find that the scatter in $\Delta z/(1+z)$ increases with Q_z beyond $Q_z = 3$ or so, and eliminating redshifts where Q_z is above 3 will cut outliers independent of redshift.

While spectroscopic redshifts are not required for EAZY to determine photometric redshifts, having a significant spectroscopic sample can help assess the quality of the photometric redshifts. There are many ways to evaluate the scatter and RMS of the $z_{phot} - z_{spec}$ relation, and Brammer et al. (2008) utilize the normalized median absolute deviation (σ_{nmad}), which is less sensitive to outliers

than other standard deviation calculations. σ_{nmad} is defined as:

$$\sigma_{nmad} = 1.48 \times \text{median}\left(\left|\frac{\Delta z - \text{median}(\Delta z)}{1 + z_{spec}}\right|\right)$$

where $\Delta z = (z_{phot} - z_{spec})$.

There are multiple ways to evaluate the photometric redshift that EAZY provides. Figure 4.2 illustrates the output for an example object. The top plot shows the input photometry in red stars with the best template combination indicated by the black line. Below is the redshift probability distribution, $p(z)$, indicating the likelihood of any redshift after taking into account the magnitude prior, if using. The peak and marginalized redshifts indicated by the red lines are provided by EAZY along with the overall $p(z)$. The peak redshift corresponds to the maximum of $p(z)$, and the marginalized redshift indicates the average redshift after integrating over the entire $p(z)$ distribution.

4.2 Photometric Catalogues and Redshifts

4.2.1 RCS2319

Multiwavelength catalogues were compiled for RCS2319 utilizing imaging from the optical to infrared. As described in Chapter 3, optical and near-infrared imaging in filters g', i', J, and K_s were processed and calibrated. Additional optical catalogues from RCS provided R_C and z' magnitude information (Gladders & Yee, 2005). Infrared photometry was available as part of a follow-up campaign

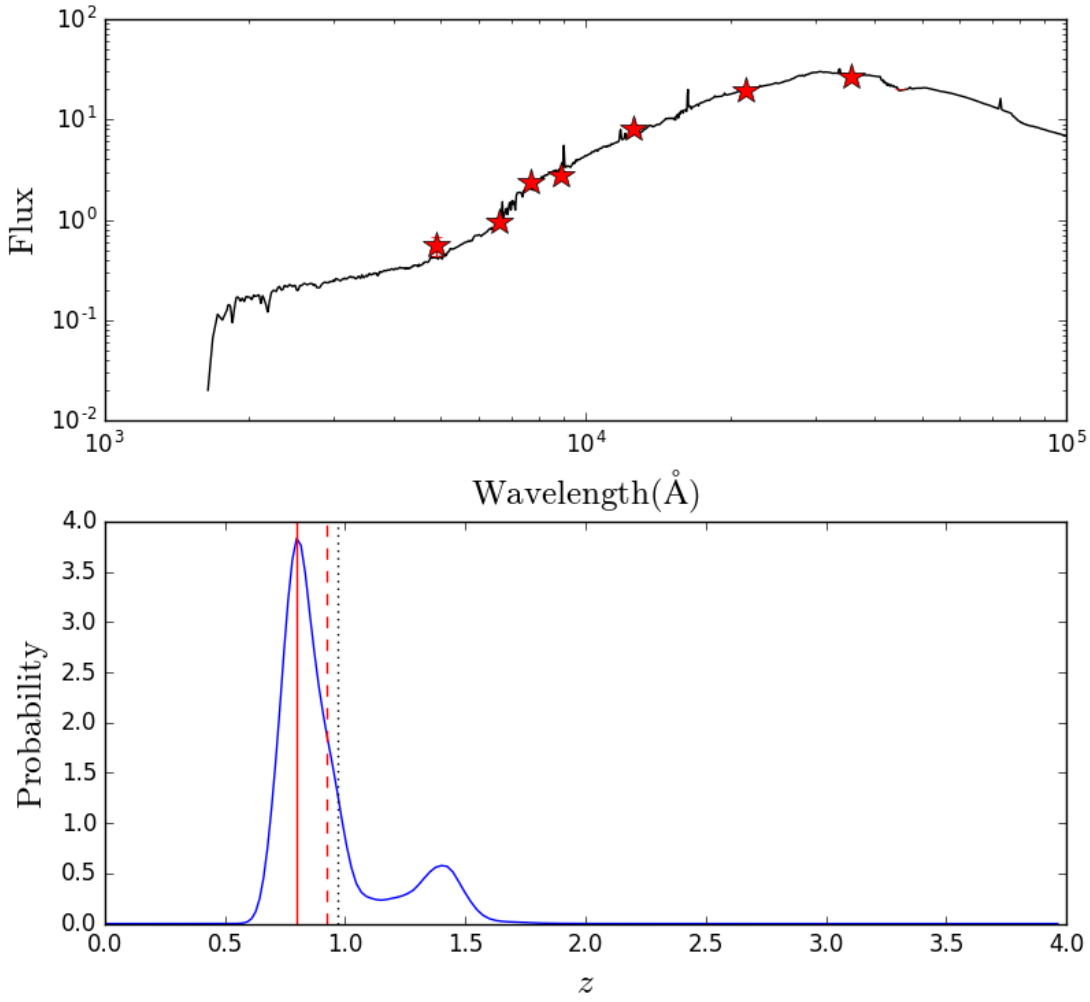

Figure 4.2: *Top:* Example SED fit (black line) to input photometry (red stars). *Bottom:* Redshift probability distribution for an example multi-peaked probability. The solid red line indicates the peak redshift (i.e. where the likelihood is maximized), the dashed red line indicates the marginalized redshift, and the dotted black line indicates the spectroscopic redshift, where available.

of RCS clusters using the Infrared Array Camera (IRAC) on the *Spitzer* space telescope (Webb et al., 2013). An extensive spectroscopic catalogue of RCS2319 was compiled by Faloon et al. (2013) resulting in nearly 2400 confident redshifts including over 300 confirmed cluster members. A matched catalogue including the spectroscopy, R_C, z', and IRAC flux information was compiled by Faloon et al. (2013). We compiled a final catalogue for RCS2319 by source matching to the Faloon et al. (2013) catalogue with a $1''$ match radius for g' and i', and a $1.5''$ match radius for J and K_s. The match radii were selected to be large enough that slight variations in the astrometry would not cause sources to be missed, and close enough to reduce matching to incorrect sources. The near-infrared data have higher chances of blending sources as well as having larger PSFs which can cause different positions for the centroid, thus a slightly higher tolerance was used. In total, the supercluster had coverage in 8 filters ($g'R_Ci'z'JK_s + 3.6\mu\text{m}, 4.5\mu\text{m}$ from IRAC) ranging from ∼5000 Å to 4.5 μm, or ∼2500 Å to 2.4 μm coverage in the restframe with 2341 high confidence redshifts available over the entire field.

Photometric redshifts were calculated using EAZY (Brammer et al., 2008). EAZY was run in multi-template fitting mode using the six default templates provided by EAZY, determined by stellar synthesis models and ranging from quiescent to starbursting, with an additional template for a post-starburst galaxy. Photometric redshifts were not trained on our sample of objects with known redshifts to avoid biasing towards our spectroscopic sample; however, zeropoints for each filter were iteratively estimated to best fit the templates for the objects with reliable spectroscopic redshifts. The zeropoints were used to help alleviate some

of the differences between each filter, due to properties such as different seeing or PSFs. The zeropoints were normalized to conserve the R_C-band flux as the r-band prior grid supplied by EAZY was used in the photometric redshift calculations (see Figure 4.1). Each object required a detection in at least four filters to have the redshift estimated.

Of the 2341 objects with a confident spectroscopic redshift, 2222 objects had sufficient filter detections to have photometric redshifts estimated. Figure 4.3 highlights the importance of incorporating a magnitude prior for redshift determination. Without taking into account the quality parameters or any other factors, the raw σ_{nmad} (as described above) decreases from 0.474 to 0.084 and the fraction of outliers with $\Delta z/(1 + z_{spec}) > 0.15$ decrease from almost 60% to under 20% with the addition of a magnitude prior.

We use the quality parameter as defined in Brammer et al. (2008) and described in §4.1.1 to characterize the quality of the photometric redshifts and remove outliers. While, as stated above, a cut of $Q_z > 3$ is recommended to reduce scatter, we find that for even modest values of $Q_z = 5$, a high portion of accurate photometric redshifts are eliminated with a substantial population around the cluster redshift. In order to see if it is possible to isolate outliers without also isolating a large fraction of confident redshift objects, we calculate Q_z using the upper and lower 1 and 2 σ intervals as well. The left panel in Figure 4.4 shows redshift scatter as a function of Q_z where Q_z is calculated using the 1, 2, and 3 σ confidence intervals (Q_{z68}, Q_{z95}, and Q_{z99}, respectively). The vertical dashed line indicates the limit of $Q_z = 3$. While most of the outliers lie to the right of the dashed line

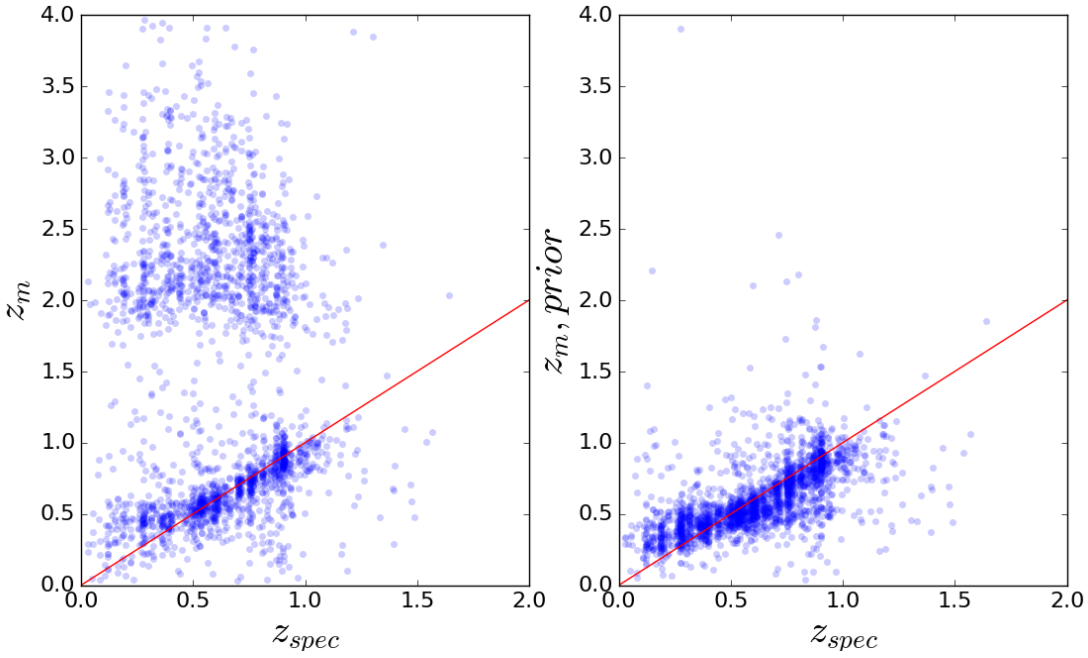

Figure 4.3: *Left:* Marginalized photometric redshift without prior applied against z_{spec}. *Right:* Marginalized photometric redshift with r based prior applied. Obvious mismatches between photometric and spectroscopic redshifts, where a large fraction of photometric redshifts are substantially overestimated, are vastly corrected once the magnitude prior is applied.

in all three cases, we can clearly see that a higher number of confident redshifts are also to the right with increasing σ-intervals. The right panel in Figure 4.4 shows the objects that are rejected for each definition of Q_z and using a cutoff of 3, with the cluster redshift boundaries indicated by the dashed black lines. While the fraction of cluster members removed is roughly the same depending on the Q_z used, the σ_{nmad} of the rejected points is higher for Q_{z68} and a higher fraction of outliers are rejected compared to Q_{z99} ($\sigma_{nmad} = 0.185$ instead of 0.141 and 23% outliers rejected instead of 20%). We thus choose to adopt Q_z using the 1 σ confidence intervals as a quality indicator and reject photometric redshifts with $Q_z > 3$.

To ensure uniformity across our sample of cluster galaxies, we use a flux limited catalogue in K_s requiring a K_s magnitude greater than the limiting magnitude of 21.9. Combined with the four filter requirement, this provides a cleaner sample of galaxies as a larger fraction of the SED will be characterized. Figure 4.5 displays the photometric redshift residuals for the final selected sample of all spectroscopic objects. The scatter (σ_{nmad}) for the entire photometric sample is 0.084, which improves to 0.081 when $Q_{z68} \leq 3$ is required, and further improves to 0.069 when $m_K \leq 21.9$ is additionally required. As seen in Figure 4.5, the photometric redshifts for lower redshift objects are consistently overestimated. This is likely due to the lack of a filter bluer than g' (such as u^*) which better characterizes nearby sources. Indeed, the scatter is further reduced around the cluster redshift ($0.7 < z_{spec} < 1.1$) to 0.053, where the low redshift galaxies are removed from the estimate. However, since there is no risk of these sources contaminating the

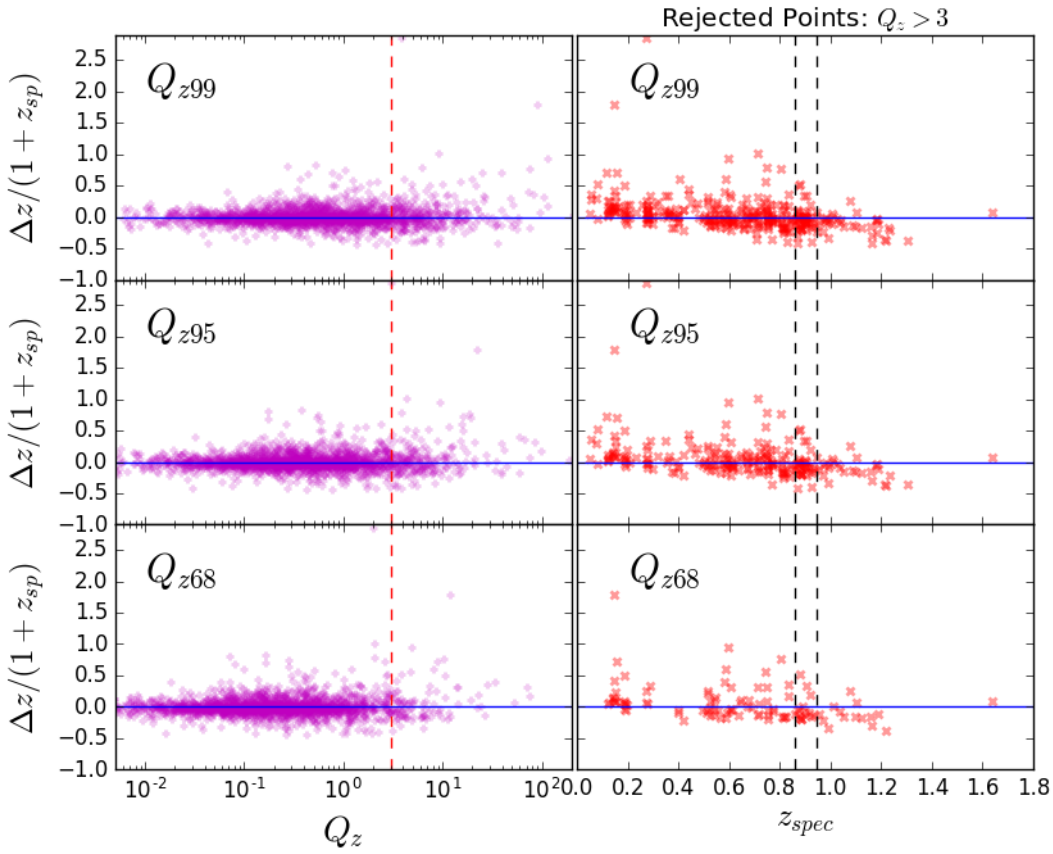

Figure 4.4: *Left:* Residuals in $\Delta z = z_{phot} - z_{spec}$ as a function of Q_z using 1, 2, and 3 σ confidence intervals. The red vertical line marks the suggested cutoff ($Q_z > 3$) for rejection. *Right:* Rejected points for $Q_z > 3$ for different confidence intervals, in residuals versus z_{spec} space. The dashed red lines indicate the spectroscopic boundary of cluster members based on Faloon et al. (2013). Clearly, using the 95th or 99th percentile quality parameters results in eliminating many reliable photometric redshifts including those of cluster members.

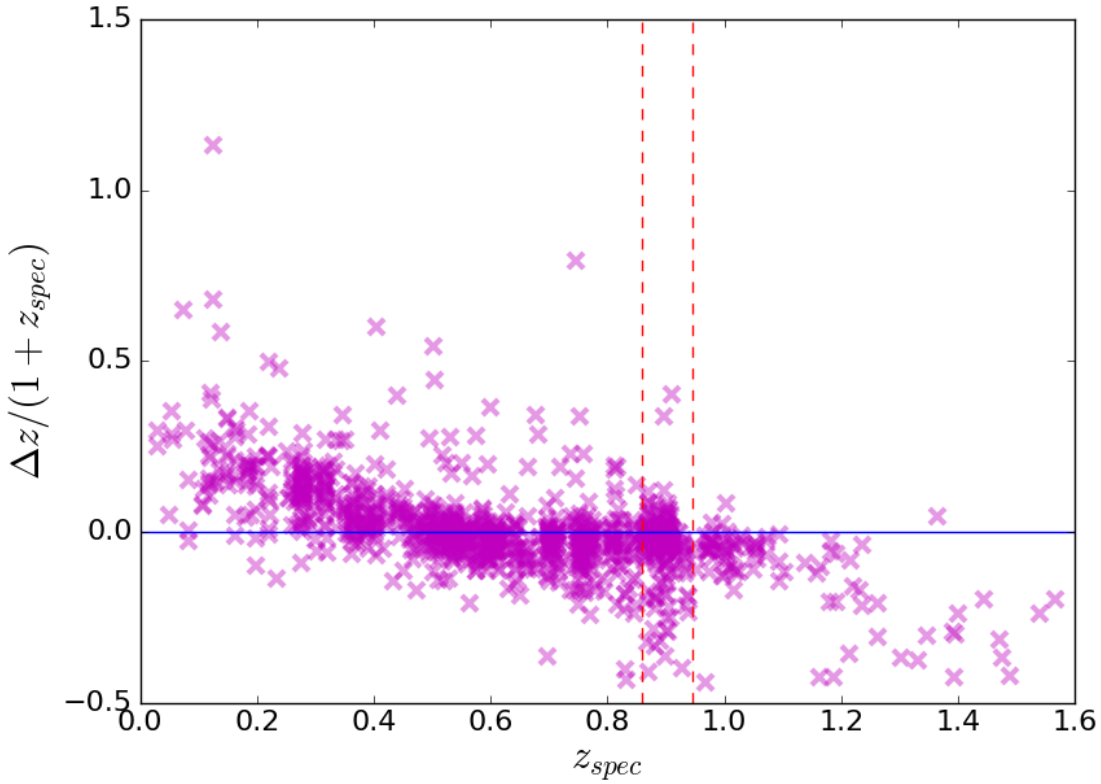

Figure 4.5: Residuals in z_{phot} ($\Delta z = z_{phot} - z_{spec}$) as a function of spectroscopic redshift for final sample where $Q_{z68} \leq 3$ and $m_K \leq 21.9$. The dashed red lines indicate the cluster redshift boundaries.

cluster sample, there is no urgent need to follow-up with blue-filter observations.

Stellar Masses

Stellar masses were determined using the IDL software Fitting and Assessment of Synthetic Templates (FAST; Kriek et al., 2009). FAST was developed to work with EAZY and uses stellar synthesis models applied to the EAZY input photometry and output photometric information. For RCS2319, FAST was run using the Flexible Stellar Population Synthesis Models from Conroy et al. (2009), the stellar initial mass function from Chabrier (2003), the dust law from Kriek & Conroy (2013), and assuming a delayed exponentially declining star-formation rate. Figure 4.6 shows the distribution in stellar mass for the high-quality ($Q_{z68} \leq 3$) photometric sample, including the K_s-limited sample. No redshift cuts have been applied; see §5.3 for mass distributions of cluster members.

4.2.2 SpARCS1049

SpARCS104922.6+564032.5 (SpARCS1049) was discovered in the SpARCS coverage of the Lockman Hole, a 15 deg^2 region of sky with a very low density of neutral hydrogen (Lockman et al., 1986). The lack of X-ray absorbing hydrogen has made the Lockman Hole a popular area for multiwavelength observations, allowing unobscured observations out to high redshifts. While surveys were originally conducted in X-rays (e.g. Hasinger et al., 1993, 1998, 2001), the Lockman Hole has since become an observing target for all wavelengths including ultraviolet (Martin et al., 2005), infrared (e.g. Kawara et al., 1998; Huang et al., 2004),

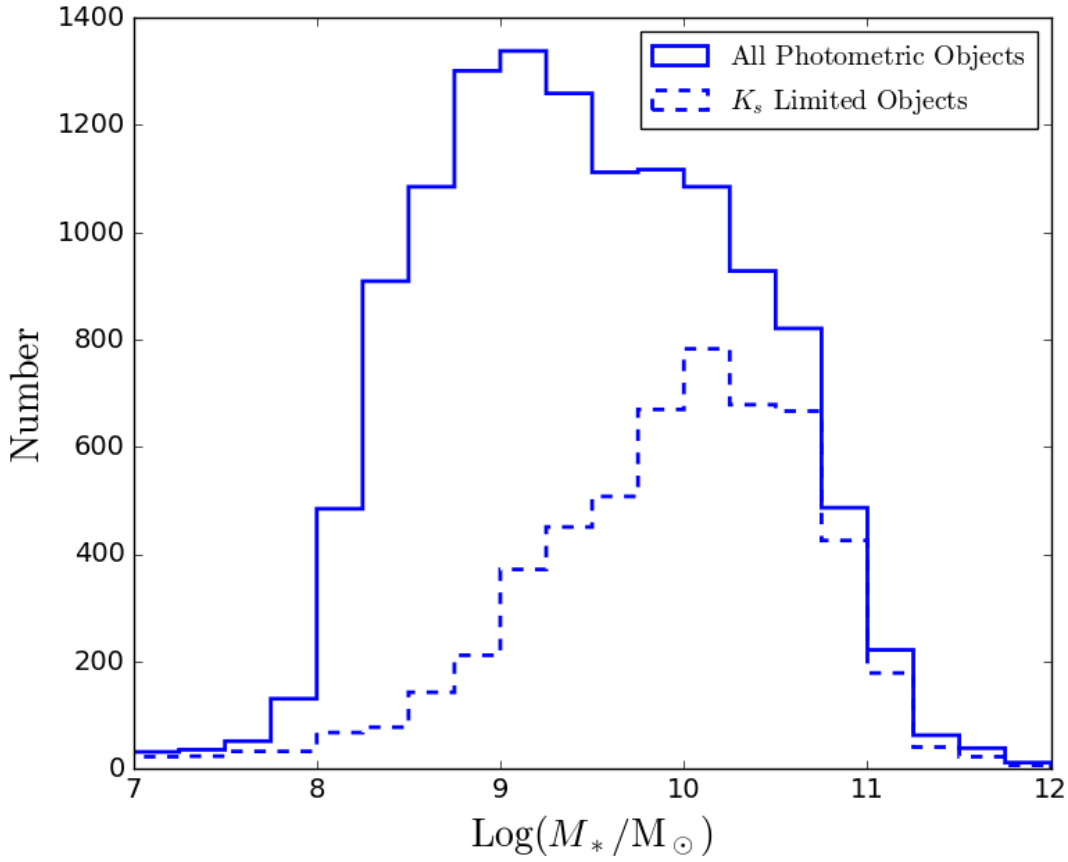

Figure 4.6: Stellar mass distribution for all photometric objects with $Q_{z68} \leq 3$, and the subset of those with $m_K s < 21.9$. No redshift selection has been applied.

submillimetre (e.g. Mortier et al., 2005; Coppin et al., 2006), and radio (e.g. Ivison et al., 2002; Ciliegi et al., 2003; Mahony et al., 2016).

Multiwavelength catalogues for SpARCS1049 were compiled from a mix of publicly and privately available data. Deep, uniform, optical observations using the CFHT in $u^*g'r'z'$ were taken as part of SpARCS follow-up (A. Tudorica, submitted). Near-infrared catalogues are available as part of the UK Infrared Deep Survey (UKIDSS; Lawrence et al., 2007), with J and K_s imaging contained in the Deep Extragalactic Survey UKIDSS catalogue. Infrared catalogues across the Lockman Hole are available from the *Spitzer* Wide-Area Infrared Extragalactic Survey (SWIRE; Lonsdale et al., 2003) as well as the *Spitzer* Extragalactic Representative Volume Survey (SERVS; Mauduit et al., 2012). Due to the location of SpARCS1049 near the edge of the SWIRE coverage, infrared fluxes in 3.6μm and 4.5μm were used from SERVS. 8-band photometric catalogues were compiled for SpARCS1049, in filters $u^*g'r'z'JK_s + 3.6\mu\text{m}, 4.5\mu\text{m}$. Limited spectroscopy was available for the vicinity of SpARCS1049; however, due to the uniformity of all datasets across the Lockman Field, photometric calibrations could be done against all available spectroscopy over the Lockman Hole, with coverage ranging from 4 to 8 filters. In total, the spectroscopic catalogue had approximately 5,600 reliable spectroscopic redshifts against which the photometric redshifts could be calibrated (via zeropoint estimations) and compared.

As with RCS2319, photometric redshifts for SpARCS1049 were determined using EAZY in multiple-template fitting mode with six templates. Zeropoints were iteratively determined, normalized to the r' flux for use with the r-prior. However,

Table 4.1: Limiting magnitudes in AB for the four optical filters, and corresponding limits in μJy.

Filter	m_{lim} (AB)	f_{lim} (μJy)
u^*	24.2	0.76
g'	24.7	0.48
r'	24.2	0.76
z'	23.5	1.46

unlike RCS2319, upper flux limits were incorporated into the photometric redshift determination. As the target cluster lies at a redshift of $z = 1.7$, the fluxes of cluster members in the optical band are very faint and in many cases non-detected. Thus for the four optical filters, instead of a null value for a non-detection, the flux and error is set to $f_{lim}/2 \pm f_{lim}/2$, where f_{lim} is the flux corresponding to the limiting magnitude in each band. Table 4.1 lists the optical depths in AB magnitudes for the four optical filters, along with the corresponding f_{lim} in units of μJy.

Zeropoints were calibrated with the non-limited catalogue, and applied to the limited catalogue. The inclusion of limits allows many more sources to have photometric redshifts determined, although at a cost of lower accuracy. Figure 4.7 shows the photometric redshifts for the limited and non-limited catalogues as a function of spectroscopic redshift. For the entire non-limited catalogue, over 4,700 sources had their photometric redshifts estimated with $\sigma_{nmad} = 0.059$. The catalogue including limits had over 5,100 photometric redshifts determined with $\sigma_{nmad} = 0.065$.

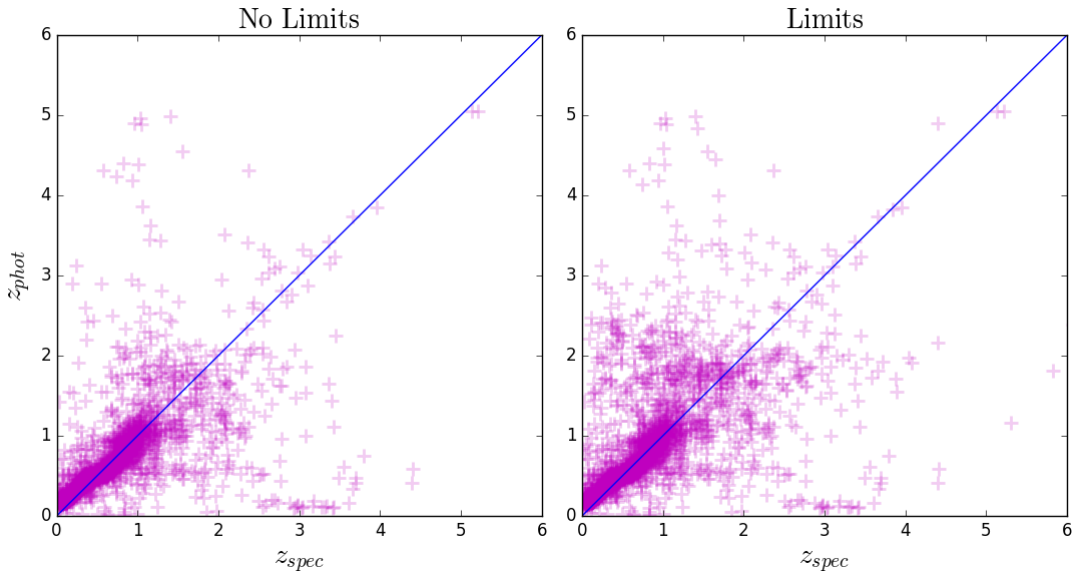

Figure 4.7: Photometric redshifts as a function of spectroscopic redshift for SpARCS1049. On the left is the cleaner sample requiring detections in at least four filters for photometric redshifts to be calculated. On the right, magnitude limits have been incorporated so that the four filter requirement includes lower limits as well as flux detections.

Stellar Masses

As with RCS2319, stellar masses were estimated using FAST in conjunction with the output from EAZY. For SpARCS1049, stellar masses were calculated using the stellar population libraries from Bruzual & Charlot (2003), the dust law from Calzetti et al. (2000), the initial mass function from Chabrier (2003), and assuming an exponentially declining star-formation rate.

5

Characterizing Galaxy Populations within the RCS2319 Supercluster

5.1 Introduction – Environmental Diversity in Superclusters

Galaxies and their properties have been shown to depend on many factors, some of them intrinsic to the galaxy itself (such as mass) and some of them extrinsic (such as environment and cosmic epoch, e.g. Gómez et al., 2003; Kauffmann et al.,

2004; Peng et al., 2010). To better understand how each factor contributes to the observed galaxy properties and how they evolve, it is necessary to probe a wide range of masses, environments, and redshifts. For environmental diversity, superclusters provide the largest sample of environments contained in a single object. They represent the largest gravitationally bound structures in the universe with masses up to several $10^{15}M_{\odot}$. They contain a large range of dynamical and physical environments from high-density cluster cores to infalling groups (which may be experiencing elevated levels of interaction (Dressler et al., 1994)) to isolated field galaxies, along with a wide range of galaxy masses with the most massive galaxies in the universe found in cluster cores. They present ideal laboratories to study environmental effects on galaxy populations, providing both relaxed cluster environments as well as dynamically active systems between the clusters themselves, with nearby groups and filamentary structure able to be identified by optical distributions of galaxies and, in some cases, X-ray signatures (Kodama et al., 2005). A single dataset is thus able to probe from the densest core regions to low-density fields using uniform data preparation and analysis.

While superclusters contain a rich sample of environments at a given epoch, finding superclusters to sample many epochs is more difficult. Many are known in the local universe; however, confirmed high redshift superclusters remain elusive, partly due to larger separations between core components at higher redshifts.

The first Red-Sequence Cluster Survey, RCS-1 (Gladders & Yee, 2005), was designed with the intent of detecting galaxy clusters over a wide range in both cluster mass and redshift. Among the hundreds of candidates discovered with the

survey was the supercluster RCS231953+00 (here after RCS2319) located at a redshift of $z \sim 0.9$. RCS2319 comprises three X-ray detected and spectroscopically confirmed cluster cores (Cluster A: RCS231953+0038.1, z = 0.901, Cluster B: RCS232003+0033.5, z = 0.905, and Cluster C: RCS231948+0030.6, z = 0.905) with a separation of less than 3 Mpc in the plane of the sky. X-ray studies have measured the cluster core masses to be $M_{X,tot} \sim 4.7 - 6.4 \times 10^{14} \mathrm{M}_{\odot}$ (Hicks et al., 2008), and Cluster A, the most massive, is a known strong lensing source (Gladders et al., 2003). Based on the clusters' proximities to one another and merger rate estimations, Gilbank et al. (2008) propose that the system will merge into a $10^{15} \mathrm{M}_{\odot}$ halo by z $\sim$ 0.5. This makes RCS2319 one of the most massive and compact high-redshift superclusters known with a complex structure comprising three cluster cores and an extensive web of filamentary structure and infalling groups (Coppin et al., 2012; Faloon et al., 2013). Extensive multiwavelength observations have been done from the optical to infrared in order to characterize the populations in the different dynamical environments present.

In this chapter we present the results from an extensive photometric study on the environments and galaxy properties of the supercluster RCS2319.

5.2 Cluster Member Selection

There are many methods for selecting cluster members from a given photometric redshift catalogue. Different photometric redshift values can be used (such as the peak probability redshift or the marginalized redshift) and uncertainties can

be selected from either the 1, 2, or 3 σ confidence intervals provided by the photometric redshift software or the overall scatter (e.g. σ_{nmad}) of the entire sample. Additionally, the redshift probability distribution is provided as shown in Figure 4.2. As the overall redshift probability distribution provides the most information that is not necessarily available using only the peak or marginalized redshift, we elect to use the integrated probability to determine the likelihood of an object being a cluster member. The integrated probability over the cluster redshift, $\mathcal{P}_{cm}$, is calculated by:

$$\mathcal{P}_{cm} = \int_{z_{cl}-\delta z}^{z_{cl}+\delta z} p(z)dz$$

where $p(z)$ is the provided redshift probability distribution, z_{cl} is the cluster redshift, and $\delta z = (1 + z_{cl}) \cdot \sigma_{nmad}$. For RCS2319, we use the median redshift of the clusters $z_{cl} = 0.905$ and $\sigma_{nmad} = 0.069$ (see §4.2.1). As $p(z)$ is normalized, $\mathcal{P}_{cm}$ will range from 0 to 1. For example, $\mathcal{P}_{cm} = 0.7$ corresponds to a galaxy where 70% of the redshift likelihood lies between $z_{cl} - \delta z$ and $z_{cl} + \delta z$. $\mathcal{P}_{cm}$ depends on factors such as how peaked the redshift probability distribution is and how near the redshift probability peak is to the cluster redshift. In the cases of quiescent galaxies, where the 4000 Å break can be fit rather well with photometry, $p(z)$ tends to be more strongly peaked and cluster members will typically have $\mathcal{P}_{cm}$ greater than 0.5. However, bluer star-forming galaxies are more difficult to characterize with photometry and tend to have a broader $p(z)$ and can have $\mathcal{P}_{cm}$ as low as 0.3 or 0.4 (Papovich et al., 2010). Figure 5.1 shows the integrated $\mathcal{P}_{cm}$ as a function of $R_C - z'$ colour where there is a clear correlation between the two, with higher $\mathcal{P}_{cm}$

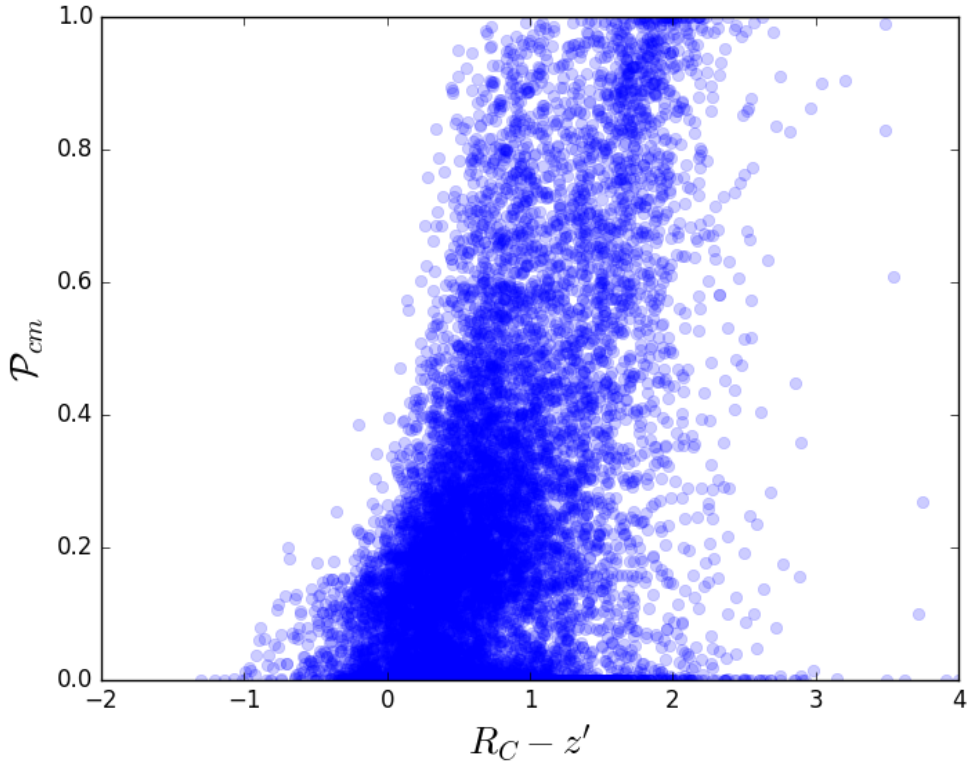

Figure 5.1: Dependence of $\mathcal{P}_{cm}$ on $R_C - z'$ colour for entire photometric sample, showing the tendency for redder objects ($R_C - z' > 1.4$ or so) to on average have higher $\mathcal{P}_{cm}$, whereas the majority of bluer objects will have $\mathcal{P}_{cm} < 0.5$.

associated with redder objects and bluer objects having on average much lower $\mathcal{P}_{cm}$.

Figure 5.2 shows example SED fits for spectroscopically confirmed cluster members and the corresponding redshift probability distributions, highlighting the integrated area over the redshift range, $\mathcal{P}_{cm}$. At the top are the quiescent galaxies, notable for their very narrow $p(z)$ resulting in a high $\mathcal{P}_{cm}$, above 0.99 for both cases. The objects are ordered by decreasing $\mathcal{P}_{cm}$, highlighting how differ-

ent galaxy types will produce different SEDs and therefore different estimates for both most likely and marginalized redshifts. Figure 5.3 shows $\mathcal{P}_{cm}$ as a function of spectroscopic and photometric redshifts in the central $25' \times 25'$ region of the supercluster where there is the densest coverage in filters, with the dashed horizontal red lines indicating $\mathcal{P}_{cm} = 0.3$ and $\mathcal{P}_{cm} = 0.5$ and the dotted line indicating $\mathcal{P}_{cm} = 0.35$. Between $\mathcal{P}_{cm} = 0.3$ and 0.35, Figure 5.3 shows most objects to be spectroscopic interlopers with few spectroscopic members. Thus in order to provide a cleaner catalogue while still allowing inclusion for bluer galaxies with broader $p(z)$, we elect to use $\mathcal{P}_{cm} = 0.35$ as our selection criteria.

5.3 RCS2319 Supercluster Galaxies

Multiwavelength observations were used to determine photometric redshifts across the cluster field, with the data described in Chapter 3 and the redshift analysis presented in Chapter 4. Across the central $25' \times 25'$ cluster region which has the most uniform wavelength coverage, there are nearly 35,000 objects of which 16,735 have photometric redshifts determined. Using quality parameter and magnitude restrictions ($Q_{z68} \leq 3$ and $m_K \leq 21.9$) and selecting cluster members based on integrated redshift probabilities ($\mathcal{P}_{cm} \geq 0.35$) we have a final cluster catalogue of 1,766 members. Images of the cluster are shown in Figures 5.4 and 5.5, with Figures 5.6 and 5.7 illustrating the distributions of cluster members.

Figure 5.4 shows a combined optical and near-infrared RGB image of the supercluster in filters g', J, and K_s. The dashed circles indicate the 1 Mpc radii of

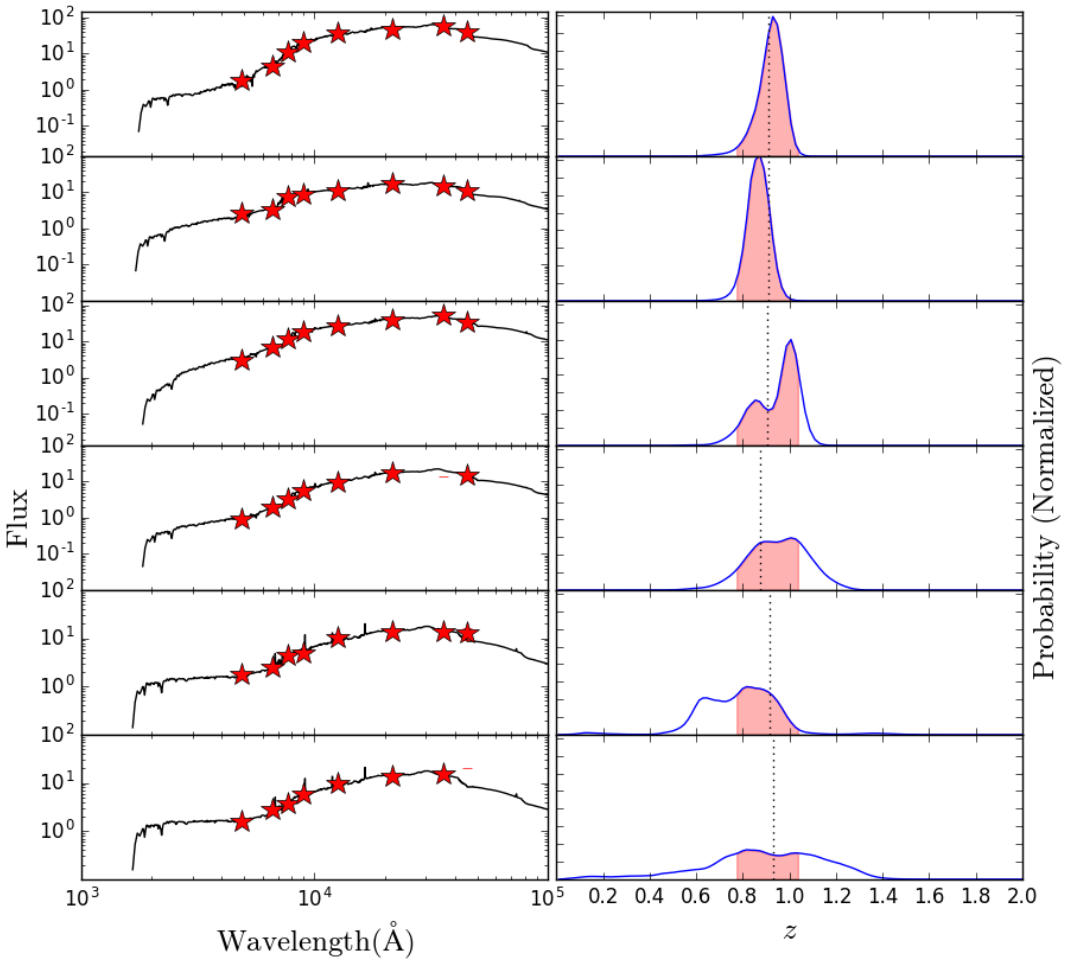

Figure 5.2: A sample of spectroscopically confirmed cluster members with integrated redshift probabilities, $\mathcal{P}_{cm}$, greater than 0.3. The fluxes and best template fits are shown in the left panels, with the redshift probability distributions, $p(z)$, shown in the right panels. The probabilities are normalized to 1, with the spectroscopic redshifts indicated by the dashed black lines and the red shaded regions indicating the integrated values over the cluster redshift bounds. The objects are ordered by $\mathcal{P}_{cm}$, with values near 1.0 at the top, to 0.3 at the bottom.

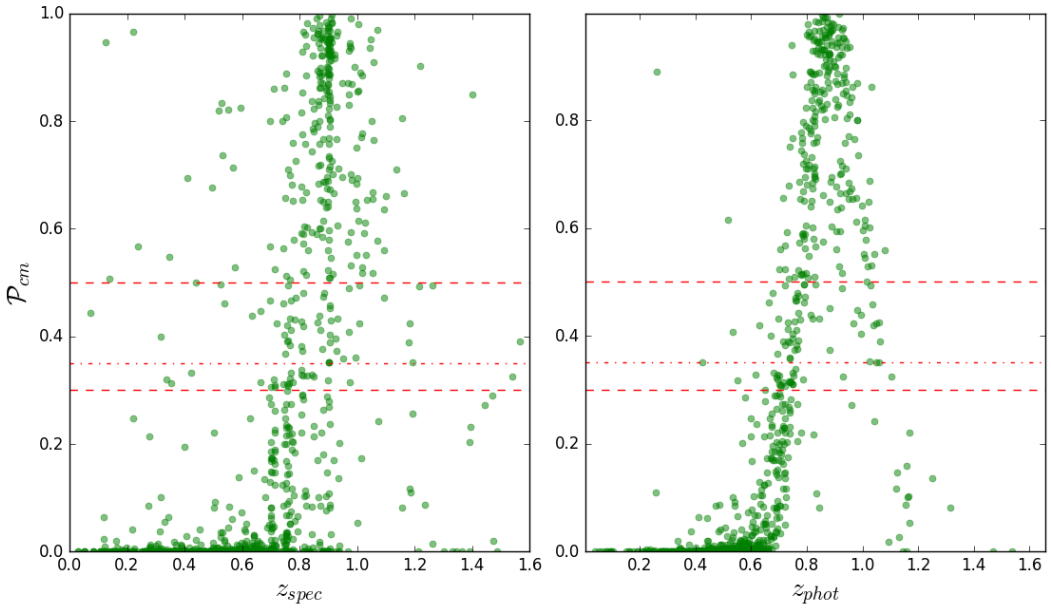

Figure 5.3: Integrated redshift probabilities, $\mathcal{P}_{cm}$, as a function of spectroscopic redshift (left) and photometric redshift (right). Shown in both plots are spectroscopic objects in the central $25' \times 25'$ region after quality and magnitude cuts. The dashed red horizontal lines indicate $\mathcal{P}_{cm} = 0.3$ and $\mathcal{P}_{cm} = 0.5$, common cuts used for selecting blue and red cluster members, and the dash-dot red line indicates $\mathcal{P}_{cm} = 0.35$.

each cluster and highlight the overdensity of red cluster members. The clusters from top to bottom are designated A, B, and C. Figure 5.5 displays insets of the individual cluster cores in RGB with filters g', i', and K_s. The cluster members appear yellow with blue-green arcs indicating situations of strong lensing, mostly apparent in cluster A and around the large galaxy near the centre of cluster C.

Figure 5.6 shows the number distribution of cluster members based on the requirements laid out above. The top panel shows only the objects where $\mathcal{P}_{cm} \geq 0.5$, and the bottom panel shows those with $\mathcal{P}_{cm} \geq 0.35$. As expected, red and quiescent galaxies are preferentially found with the higher $\mathcal{P}_{cm}$ requirements, as the (red-sequence selected) cores are dominant. Using the requirement $\mathcal{P}_{cm} \geq 0.35$ still strongly selects the cores, but also includes more objects, including bluer ones, in the surrounding areas. In order to fully investigate the environmental dependence on galaxy properties, it is thus necessary to ensure inclusion of bluer, star-forming objects.

Figure 5.7 shows the distribution of cluster selected object in terms of colour and mass properties. Cluster centres are indicated by the black stars, and the white contours show the unresolved 250μm emission from Coppin et al. (2012), indicating the high starforming filament between Clusters A and B. For the left panels which show objects as a function of colour, we use a conservative colour cut of $(R_C - z') \geq 1.4$, with the two filters bracketing the 4000 Å break at $z = 0.9$, as the division between the blue and red populations (see Figure 5.8 for a colour−magnitude diagram highlighting the separation between blue cloud and red sequence populations). The majority of the red galaxies are found near

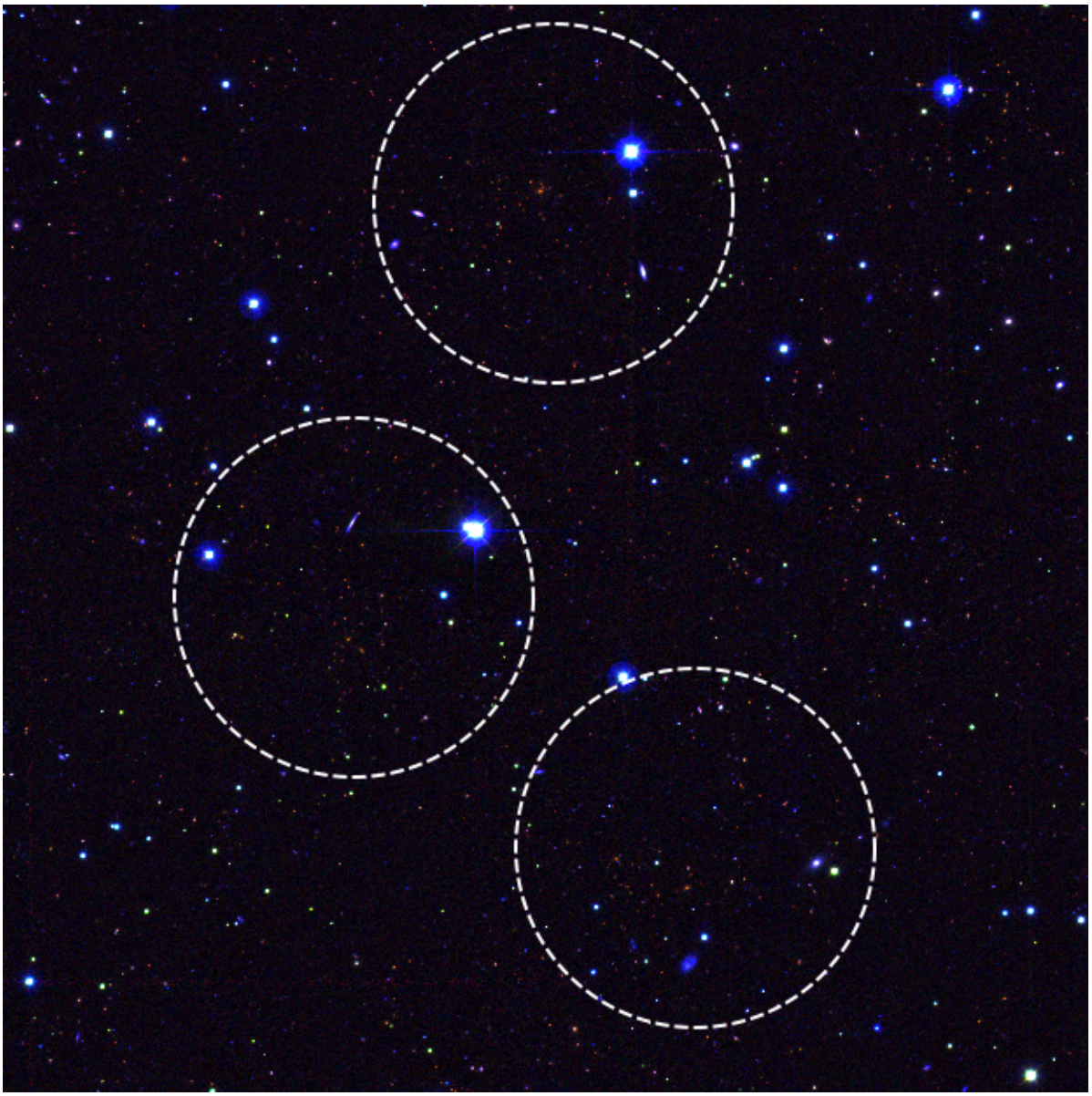

Figure 5.4: Approximately $12.5' \times 12.5'$ RGB cutout around the RCS2319 supercluster in $g'JK_s$. The dashed circles represent the physical 1 Mpc radius for each cluster component, centred on the red-sequence overdensity peaks. The clusters are dominated by the population of red objects near the central regions of each circle.

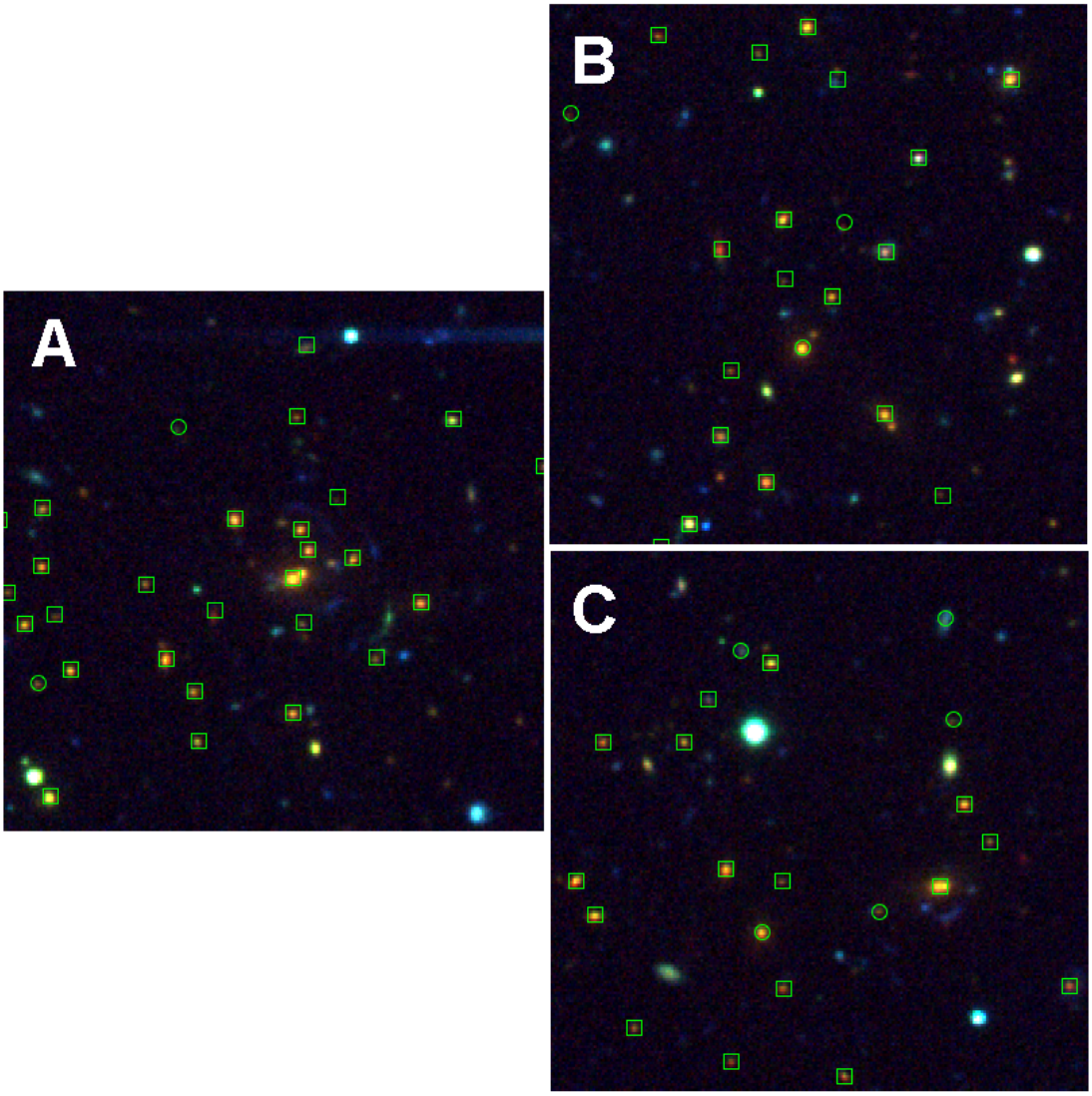

Figure 5.5: 500 kpc $\times$ 500 kpc insets of the central regions of the three clusters in $g'i'K_s$. The green squares and circles indicate cluster members selected with $\mathcal{P}_{cm} \geq 0.5$ and $\mathcal{P}_{cm} \geq 0.35$, respectively. Faint blue-green arcs from strong lensing are visible around the center of Cluster A, as well as around the brightest galaxy (near lower right) in Cluster C.

the cores of the clusters while the blue galaxies tend to be distributed fairly uniformly across the field. The right panels show the distribution of galaxies by stellar mass using $3 \times 10^{10} \mathrm{M}_{\odot}$ as the division between high and low mass galaxies, following Kauffmann et al. (2004). As with red galaxies, the high mass galaxies are preferentially located near the cluster cores, although there is a significant presence of lower mass galaxies near the cores as well. There is a very slight excess of low-mass and blue galaxies in the southern lobe of the *Herschel* filament, suggesting that perhaps there is a population of low-mass, star-forming galaxies causing the increased submillimetre emission.

5.4 Galactic Properties as a Function of Environment

5.4.1 Local Environment

The local environment of a galaxy generally refers to its immediate surroundings regardless of the overall structure the galaxy is found in. To quantify the local environment for each object in our supercluster, we calculate the projected tenth nearest neighbour density, $\Sigma_{10} = \dfrac{10}{\pi d_{10}^2}$, where d_{10} is the distance to the tenth nearest neighbour. We choose to use tenth nearest neighbour to reduce the probability of the intrinsic densities being increased due to the presence of interlopers. We are less concerned with the absolute density of the regions in which the galaxies reside, and more interested in the relative environments i.e. which galaxies

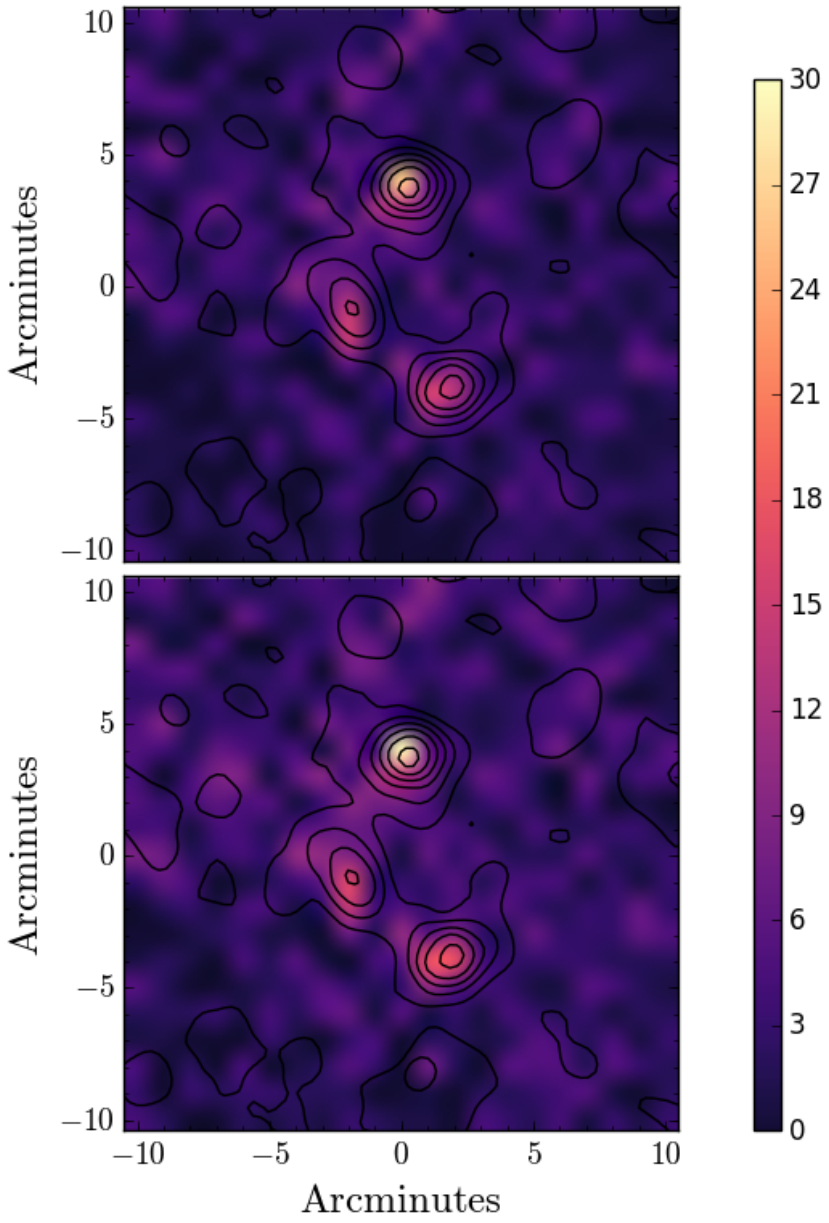

Figure 5.6: Number density, in units of galaxies per arcmin^2, of photometric cluster members for different integrated redshift probabilities. The black contours indicate the smoothed red-sequence contours, starting at 2.5σ significance. The top panel shows the subset for which $\mathcal{P}_{cm} \geq 0.5$ which is generally used to select red, quiescent members. The bottom panel shows the selected cluster subset with $\mathcal{P}_{cm} \geq 0.35$.

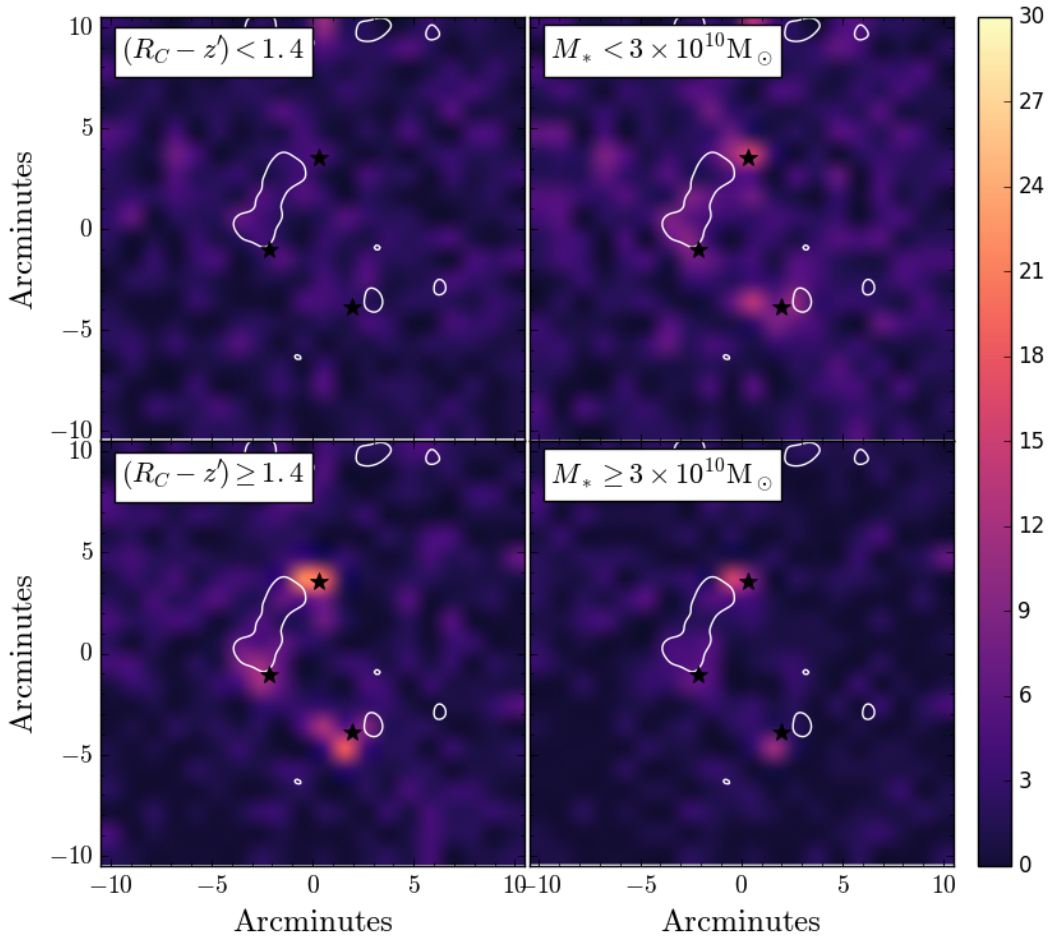

Figure 5.7: *Left:* Distribution of blue galaxies (top; $R_C - z' < 1.4$) and red galaxies (bottom), in galaxies per arcmin^2. *Right:* Distribution of low mass galaxies (top; $log(M_*/\mathrm{M}_\odot) < 10$) and high mass galaxies (bottom). The black stars indicate the centres of the clusters based on the red-sequence contours, and the white contours indicate the smoothed 250μm emission from Coppin et al. (2012).

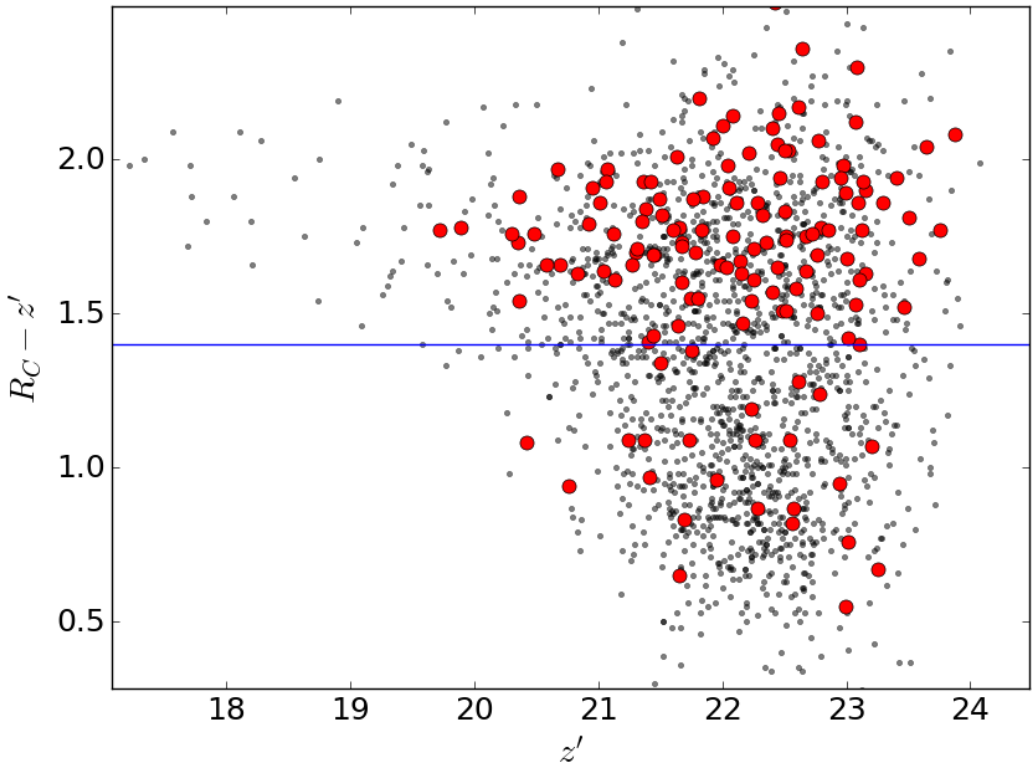

Figure 5.8: Colour−magnitude diagram in $R_C - z'$ and z' for cluster objects within 500 kpc of a cluster core (red circles) and all other cluster field members (black dots). The blue horizontal line indicates the division between red-sequence (centred approximately along $R_C - z' = 1.8$) and the blue cloud which is sparsely populated by core members but has many field galaxies. The boundary at $R_C - z' = 1.4$ is selected to be on the conservative (redder) side to ensure minimal blue cloud contamination.

reside in the densest or least dense regions in the supercluster system. We thus measure the relative overdensity, $\Sigma_{10}/\langle\Sigma_{10}\rangle$ expressed as $(1+\delta_{10})$, where $\langle\Sigma_{10}\rangle$ is the mean surface density calculated from the tenth nearest neighbour. Expressing the density in terms of $\log(1+\delta_{10})$ provides a relative density measurement where a negative value represents an underdense regions relative to the mean density, and a positive value represents an overdense region relative to the mean.

While photometric redshifts can smear out structure compared to using more precise spectroscopic redshifts, studies by Lai et al. (2016) have shown that structure can still be recovered and colour−density relations can still be retrieved even for moderate uncertainties of $\pm 0.06(1+z)$, comparable to the scatter of our sample around the cluster redshift. Indeed, while we are unlikely to recover the intrinsic densities in 3D space, we are able to identify those galaxies residing in the highest and lowest local density environments and reveal if any dependence of colour on local environment exists. To aid in disentangling the relationship between stellar mass, colour, and environment, we bin in mass with a lower limit of $10.2 < \log(M/\mathrm{M}_\odot)$. The depth in K_s-magnitude and the dependence between K_s-magnitude and mass (see Figure 5.9) suggests that we are complete down to a mass of $\log(M/\mathrm{M}_\odot) = 10.2$ so we choose this as our lower stellar mass limit. We split into three mass bins: $\log(M/\mathrm{M}_\odot) = 10.2, 10.5$, and 10.81, roughly corresponding to 1.6, 3.2, and $6.5\times10^{10}\mathrm{M}_\odot$. The mass bins were selected to have similar numbers of objects, while still sampling a broad enough mass range. Objects were also split into three density environments: $\log(1+\delta_{10}) < -0.3, -0.3 \leq \log(1+\delta_{10}) < 0.3$, and $0.3 \leq \log(1+\delta_{10})$ which correspond to regions of half the average density, av-

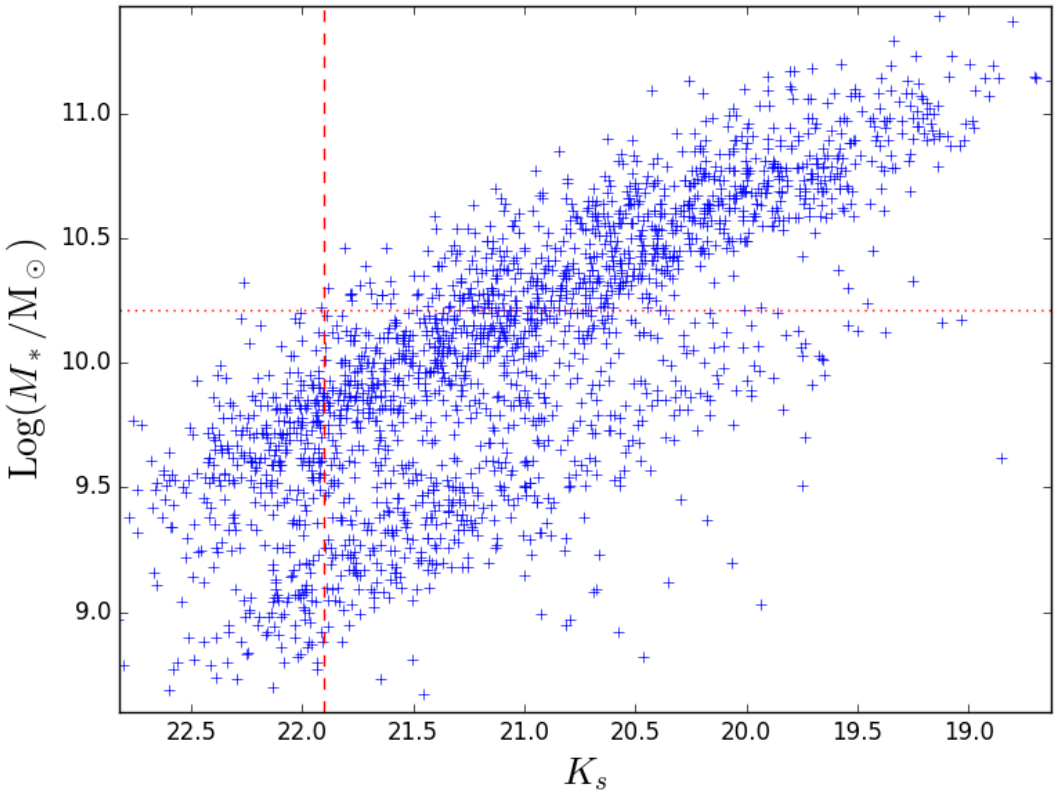

Figure 5.9: Stellar mass as a function of K_s magnitude for objects with $\mathcal{P}_{cm} \geq 0.35$. The vertical dashed line indicates the limit of $K_s = 21.9$, with the horizontal line indicating the corresponding mass limit.

erage density, and twice the average density. Figure 5.10 shows the dependence of $R_C - z'$ colour with relative overdensity, for both the entire sample and controlled for mass, as well as the fraction of red galaxies, f_{red}, as a function of relative overdensity.

To characterise how significant the trend is, we determined the best fit slope and uncertainty using a χ^2 minimization routine for each mass bin. The best fit slopes and uncertainties along with the number of standard deviations from

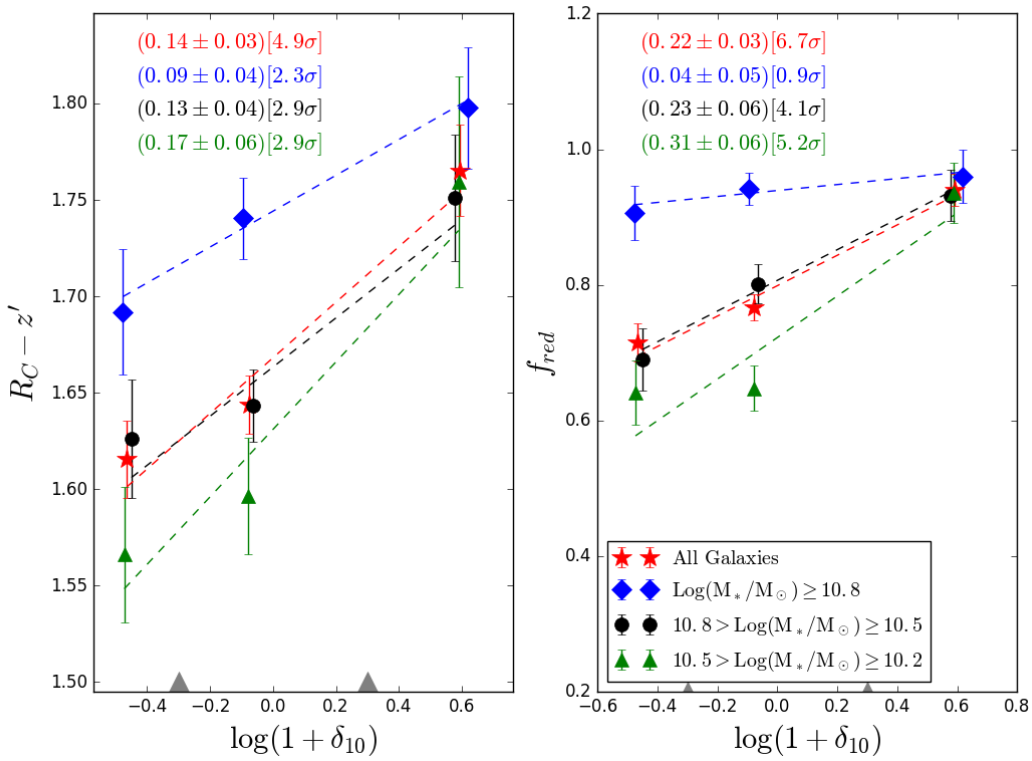

Figure 5.10: *Left:* Mean $(R_C - z')$ colour controlled for stellar mass as a function of relative overdensity in three density bins (underdense, average density, overdense), indicated by the grey triangles. The x-position indicates the mean overdensity per overdensity bin and the error bars show the standard error of the mean. *Right:* The fraction of red galaxies (defined as having $R_C - z' > 1.4$) as a function of relative overdensity in the same three density bins. The dotted lines represent the best fit slopes, with the slopes and uncertainties indicated in the top left for the corresponding mass bins. In brackets we indicate how significant the slope is in terms of how many standard deviations it is away from zero. The red stars indicate the relation for the entire sample of galaxies with $\log(M/\mathrm{M}_\odot) > 10.2$.

zero are shown in Figure 5.10. Indeed, for the entire mass limited sample there is a strong trend with colour and red fraction increasing as a function of local density, significant at nearly 5 and 7σ, respectively. When controlled for mass, the relation still appears to hold in nearly all bins although at lower significance. The correlation between local overdensity and colour is marginal yet consistent between all three mass bins, at significances of $2-3\sigma$. For the highest mass galaxies ($M_* \geq 6.5 \times 10^{10} \mathrm{M}_\odot$), their average colour increases with local density although as the second plot in Figure 5.10 shows, the fraction of red galaxies is nearly constant with density.

The galaxies are thus becoming redder with overdensity, although since the average colour is consistent with lying on the red-sequence, it is likely that the majority of the quenching has already occurred for the mass-selected sample with $\log(M_*/\mathrm{M}_\odot) \geq 10.2$. However, the lower mass galaxies still exhibit a significant increase with red fraction and local density. While, on average, the lower mass galaxies are still red (see in the first plot in Figure 5.10), there appears to be transition between blue-cloud and red-sequence populations dependent on local density. Darvish et al. (2016) find similar trends, with the quiescent fraction of galaxies increasing with both local overdensity and stellar mass for $z \lesssim 1$. Kawinwanichakij et al. (2017) also find the fraction of quenched galaxies increases with local overdensity over $0.5 < z < 1.0$ and determines both environmental and mass driven quenching mechanisms are present. Both studies find that environmentally driven quenching becomes less important at higher redshifts ($z > 1$) where mass driven quenching becomes dominant. At our cluster redshift of $z = 0.9$, our

findings our consistent with these results where we find both mass and density dependences on colour and red fraction. The fraction of red galaxies appears to have a higher dependence on local environment for lower mass galaxies, consistent with Kawinwanichakij et al. (2017) where they find environmentally driven quenching to have a stronger effect on lower mass galaxies.

A local density influenced quenching mechanism suggests that galaxies are gravitationally interacting with their neighbours, through processes such as harassment or merging. However, the densest regions are found in the cluster cores so it is possible the local overdensity is a proxy for global environment as well. Thus it is also possible that cluster driven quenching mechanisms such as ram-pressure stripping and strangulation are, at least partly, responsible for the observed colour–density relation.

5.4.2 Global Environment

While some studies look at properties such as cluster-centric radius to define the global environment a cluster galaxy resides in (e.g. Gómez et al., 2003; Li et al., 2009), the presence of three cluster cores makes this measurement difficult for RCS2319. Instead, we search for structures in the supercluster system using a friends-of-friends (FOF) grouping algorithm, following the spectroscopic analysis in Faloon et al. (2013) and adapted from Huchra & Geller (1982). A simplified version of the FOF algorithm is used, utilising a set linking length, D_L, and assuming all selected cluster objects are located at $z = 0.9$. While spectroscopic catalogues enable the use of line-of-sight velocities to make radial cuts in linking

members, the uncertainties in photometric redshifts are too broad to ascertain any dynamical information.

The FOF algorithm identifies structures using the following method: for each cluster member, we find all of its neighbours that fall within a projected distance of less than D_L. For all of those neighbours, we then look for all of its neighbours within the linking length that have not already been identified as group members. Once every member has no more new friends, the group membership is complete and the same process is done for the next object in the list not already in an identified association. The linking length was chosen through trial and error with the goal of structure recovery without linking all three cores together. A physical distance of $D_L = 175$ kpc was selected to meet these requirements.

To test the validity of our groups, we randomly distribute all cluster members over the same area and run the group finding algorithm using the same D_L requirement. Figure 5.11 shows the results of the FOF algorithm on the cluster, top, and an example Monte Carlo run, bottom. We run the simulation 1000 times and take the average number of groups for each group length, the results of which are shown compared against the cluster groups in Figure 5.12.

The largest structures recovered are the cluster cores with clusters A, C, and B comprising 82, 57, and 55 members, respectively. Additionally, six associations are found with greater than 15 members compared to an average of 0.8 associations of the same respective lengths from the 1000 Monte Carlo trials. We thus define three global environments: cores, consisting of the three largest associations; groups, the three non-core associations with greater than 15 members, which have a higher

Figure 5.11: The results of the FOF algorithm for a linking length of 175 kpc. The cluster is on the top, with a sample Monte Carlo randomization on the bottom. The groups are connected by lines with the colour of the group indicating the size; dark purple are small groups, with group size increasing from blue to green to yellow.

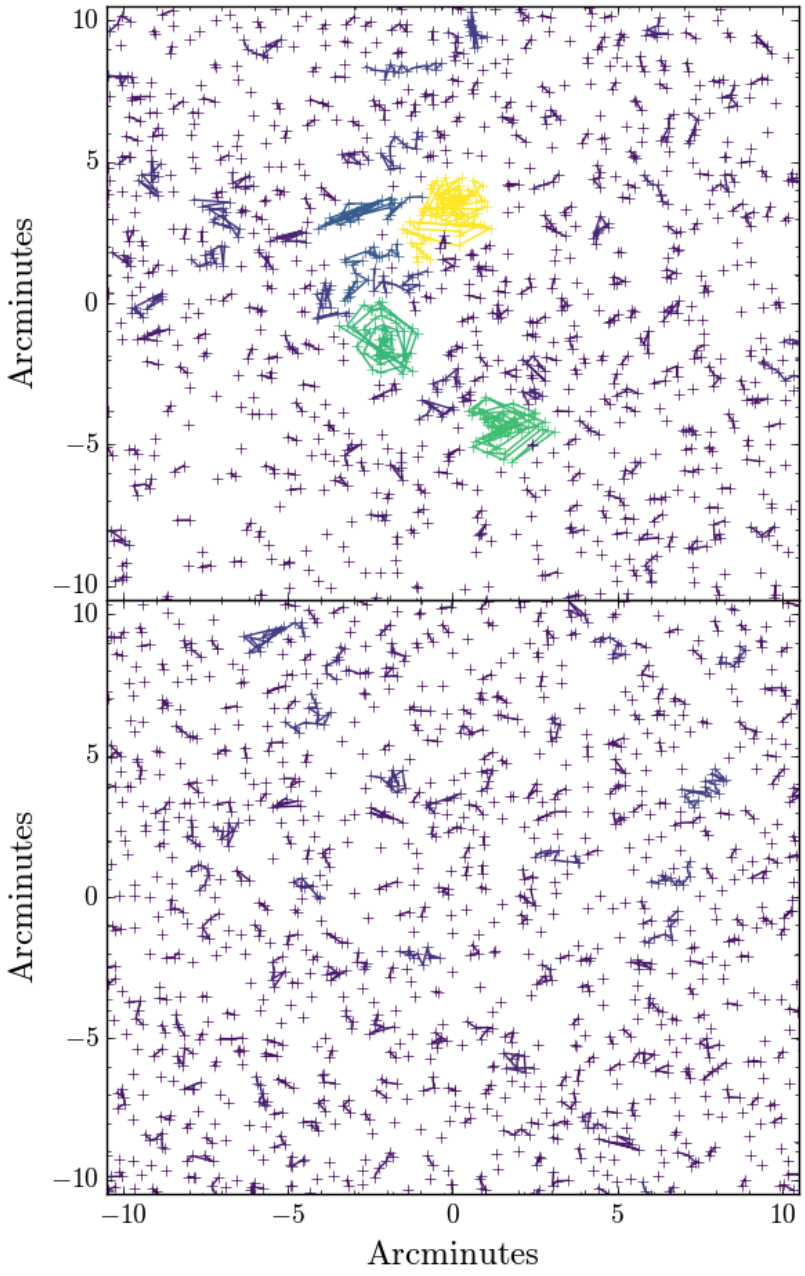

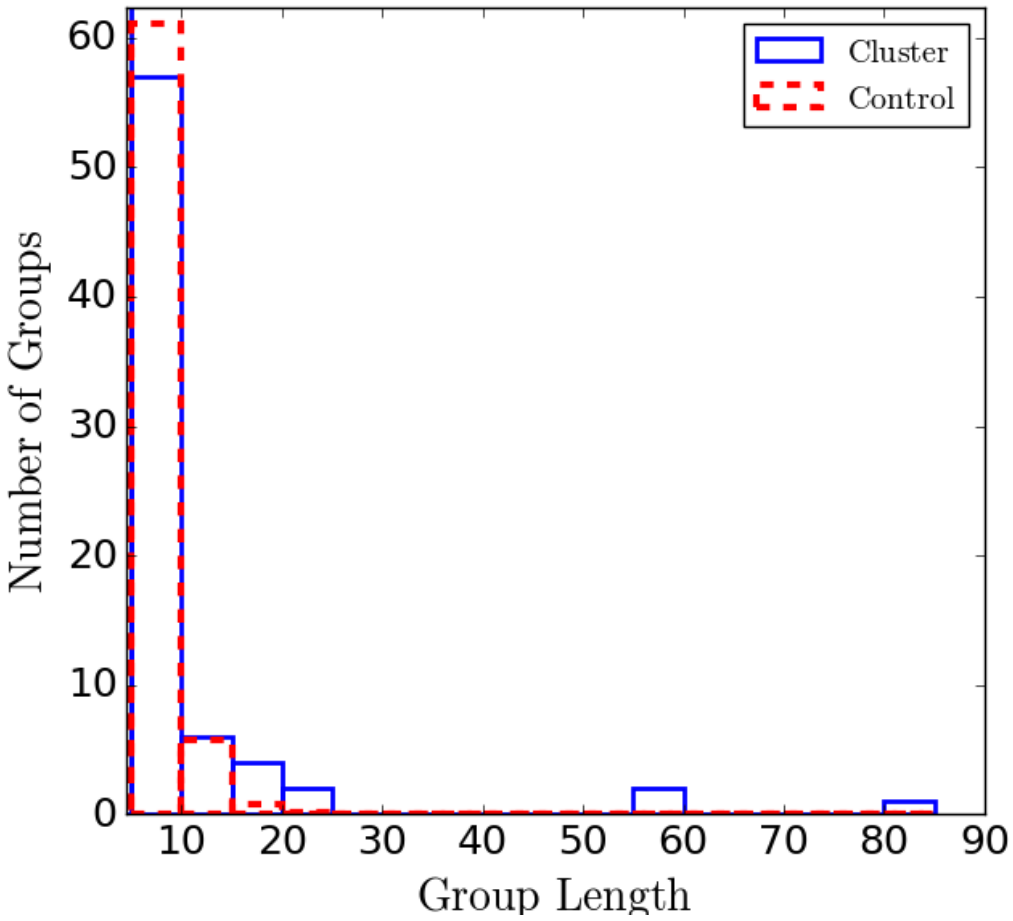

Figure 5.12: Group length distributions for the supercluster (blue line) and 1000 control trials (red dashed line) for groupings with at least five members. The three largest groups are the three supercluster cores.

likelihood of tracing real structure; and field, any associations with fewer than 15 members, consistent with a random distribution of sources across the field.

Figure 5.13 shows the results of the group finding algorithm indicating the cores, groups, and field galaxies. The bottom left plot in Figure 5.13 shows the normalized distribution in stellar mass for each grouping classification, and the bottom right plot shows the normalized distribution in $R_C - z'$ colour. We see a clear red-sequence in the colour distribution of the cluster cores centred around $R_C - z' = 1.7$, as well as an overall higher mass distribution. This is also evidenced in Figure 5.6, where nearly all red-sequence and highest mass galaxies reside in the high density cluster cores, consistent with what is seen in the local universe (Baldry et al., 2006). The field population lacks a clear red-sequence and comprises lower mass galaxies, consistent with what is observed at $z = 0$. However, the intermediate populations between these two extreme density environments are identified as the six FOF groups, and are not as easily classified as the other two environments.

Two-sided Kolmogorov−Smirnov (K−S) tests were done between the different classifications for both mass and colour distributions in order to investigate the likelihood that the galactic properties of a given environment are similar to those of another. As expected, the field and core populations in terms of colour and mass are most definitely drawn from different distributions, with the null hypothesis consistent at $> 99.99\%$. The groups also appear to be drawn from a different distribution than the core populations, with likelihoods less than 1%. However, we cannot exclude the possibility that the groups are from the same mass and

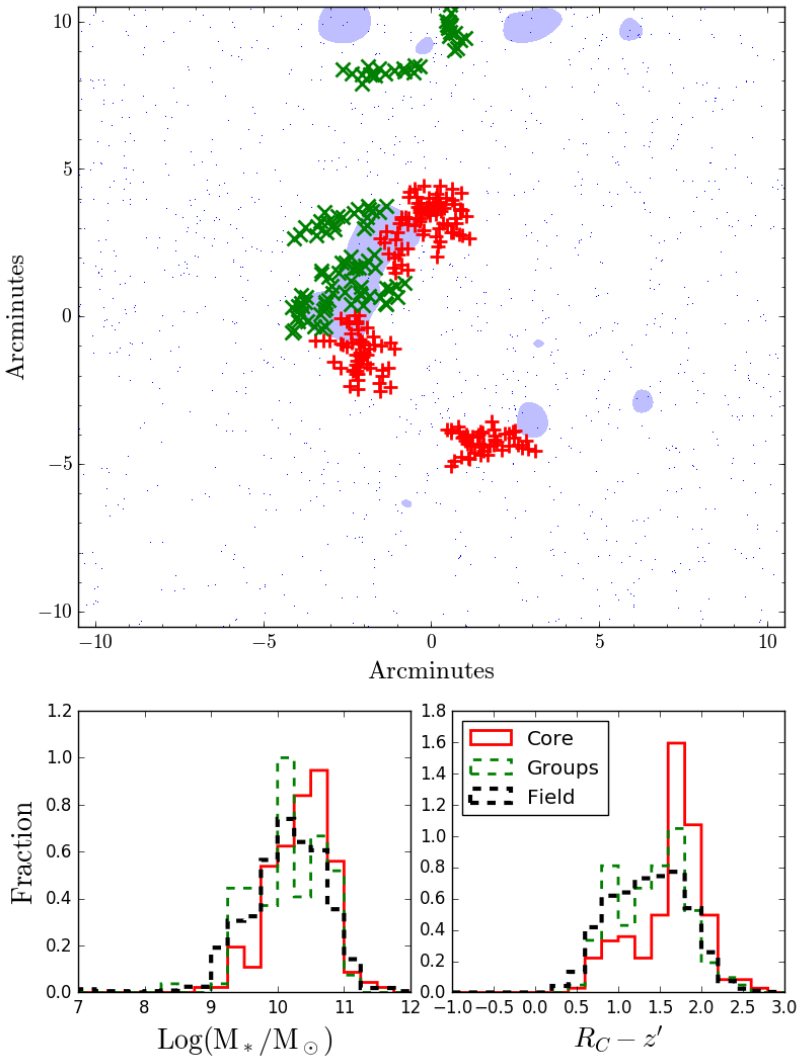

Figure 5.13: Results of the group finding algorithm with three cores indicated in red, six groups in green, and field galaxies in black. Groups are defined as non-core associations with 15 or more members, with field galaxies defined as associations with fewer than 15 members. The background blue contours indicate the position of the submillimetre bright filament from Coppin et al. (2012), also indicated in Figure 5.7. The normalized stellar mass and $R_C - z'$ colour are shown in the bottom plots for the three environmental classifications.

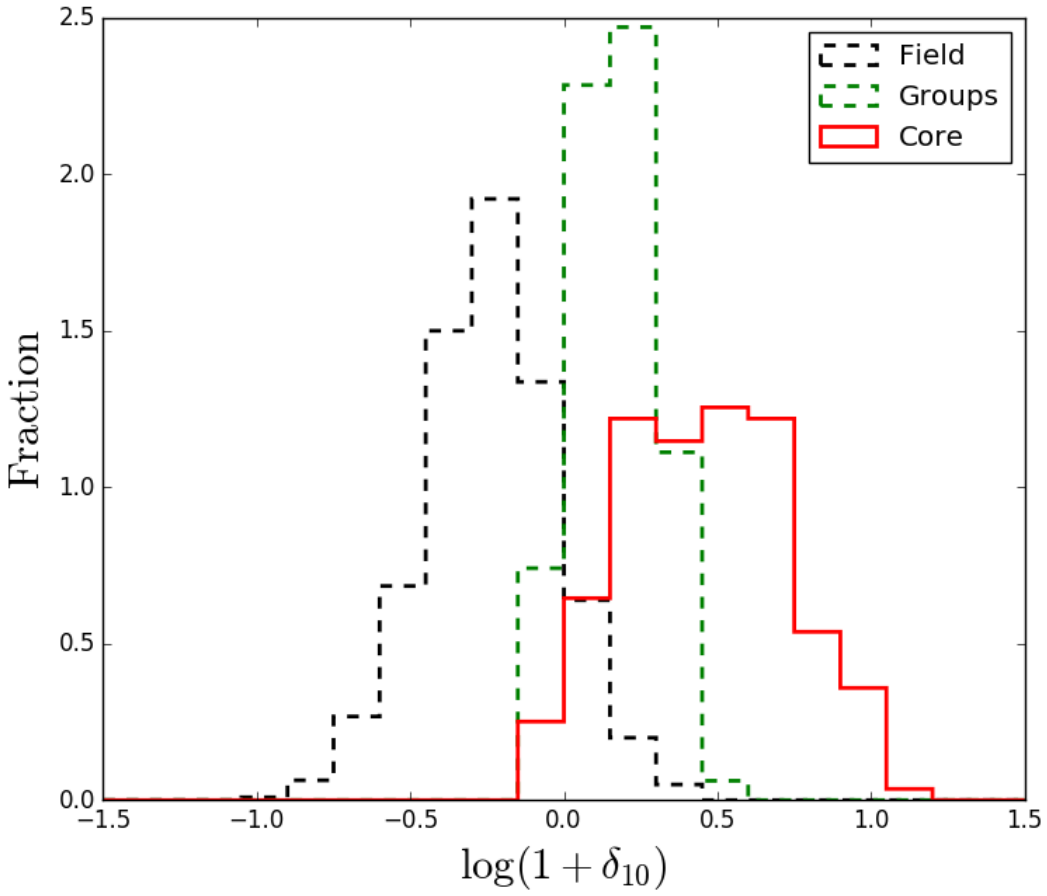

Figure 5.14: Overdensity distributions of field, group, and core populations as identified by the grouping algorithm, as shown in Figure 5.13.

colour distributions as the field galaxies at high significance ($\sim$ 80% in both cases).

Indeed, Figure 5.13 highlights the strong population of red galaxies present in the core populations as well as an excess of high-mass galaxies and relatively fewer low-mass galaxies. The similarity between the group and field galaxies suggests that there is no evidence of pre-processing occurring in group environments and any associations that might end up being accreted onto the cores have not yet

experienced strong quenching. In contrast, the spectroscopic FOF analysis done in Faloon et al. (2013) found that the five significant non-core group associations tended to have a higher fraction of red sequence galaxies compared to the field, although not as many as the core populations. However, the structures found by the spectroscopic FOF algorithm do not overlap with the FOF associations found in the photometric analysis with the exception of the filament and a group coincident with Cluster B which identified as part of the core population. The location of the filament based on the 250μm emission from Coppin et al. (2012) is indicated by the shaded blue region in Figure 5.13. Interestingly, Faloon et al. (2013) find that the filament is instead populated with a higher fraction of blue galaxies and that the red fraction of the other combined groups increased considerably when the filament is excluded from the analysis. Of the six associations we find with our FOF algorithm, three of them overlap with the filament region suggesting that part of the similarity between the groups and field is simply that some of the groups are dominated by low-mass, high star-forming galaxies. As star-forming populations tend to look more similar to field populations rather than quiescent core galaxies, there is no clear evidence of quenching occurring in the group environments. Similar results are found in a star-formation study of the $z = 0.55$ supercluster Cl0016+16, where localized pockets of enhanced star-forming fractions are found along filamentary structure (Geach et al., 2011). They propose that star-formation is being triggered in infalling populations due to tidal or gravitational interactions, a form of pre-processing that will eventually quench the populations but currently causes them to resemble non-cluster field galaxies.

It's possible a similar scenario is occuring in the RCS2319 filament where we are seeing pre-processing during an active star-formation phase, but before quenching has caused a complete transition to red-sequence galaxies.

We also investigate the local density properties of the FOF structures, as seen in Figure 5.14. Indeed there is an overlap between the selection of the two environmental probes, with the large core structures residing in overdense environments, the field galaxies almost exclusively population relatively underdense environments, and the groups lying in between. It is interesting then that although the group structures populate a significantly different local environment than the field galaxies, we don't see any statistically different properties in terms of stellar mass or colour. It's possible that this is mostly due to the filament's presence, as described above. Due to the small numbers statistics, it's difficult to constrain whether or not there is evidence of an enhanced red fraction in the non-filamentary identified groups.

It has been suggested that the majority of accreted cluster galaxies do not experience any form of 'processing' or evolution before encountering the cluster environment (Berrier et al., 2009). This suggests that perhaps the interactions between infalling group members, such as merging and harassment, are not as influential as the cluster environment itself. Interactions between the hot intracluster X-ray halo and infalling galaxies can cause both rapid and slow timescale quenching in the form of ram-pressure stripping and strangulation, respectively. Simulations by Taranu et al. (2014) favour longer timescale quenching in the form of strangulation to explain the morphologies and colours of infalling galaxies. If

the majority of non-cluster galaxies are being accreted as late-type, star-forming galaxies, it suggests that these intra-cluster medium (ICM) triggered mechanisms are a more dominant source of galactic evolution.

5.5 Summary

In this chapter we have presented a multiwavelength photometric study of the $z = 0.9$ supercluster RCS2319+00. We have determined over 16,500 photometric redshifts across our 1 sq. deg. field with over 1,700 objects with high confidence redshifts selected as cluster members in the central $25' \times 25'$ region. We find an excess of high-mass, red galaxies located near the cluster cores, with a slight excess of low-mass galaxies residing near a previously IR identified star-forming filament. We find significant colour$-$density and red-fraction$-$density relations for a mass limited sample at the 5-7σ levels. After controlling for mass, the dependence weakens although it is still present, especially for lower mass galaxies. This implies that there are both extrinsic (environmental) and intrinsic (mass) quenching mechanisms affecting the evolution of the cluster populations. We also define global environments using a Friends-of-Friends algorithm. We identify six associations as groups along with the three cluster cores and a population of field galaxies. The core populations are notably different from the group and field populations, with an excess of massive and red galaxies. The properties of groups appear to be consistent with those of the field galaxies, and we are unable to rule out the possibility that they are drawn from the same distribution. Several of the

groups overlap with the infrared star-forming filament which could explain why the groups have populations similar to the field (low-mass and blue colours, consistent with field star-forming populations). With the similarity between the field and group populations, this suggests that inter-galaxy interactions do not significantly contribute to any pre-processing as galaxies fall into the cluster potential, and that rather processing is more likely to occur once they have reached the cluster environment and begin interacting with the ICM.

RCS2319+00 presents a rare opportunity to probe many different densities and environments all located within the same object. We are able to investigate how galaxy evolution is affected by the environment, from field galaxies to infalling to groups to dense cluster cores, as well as the different density regions within each environment.

6

Galaxy Merger Candidates in High-Redshift Cluster Environments

This chapter is adapted from the following paper:

"Galaxy Merger Candidates in High-Redshift Cluster Environments"

A. G. Delahaye, T. M. A. Webb, J. Nantais, A. DeGroot, G. Wilson, A. Muzzin, H. K. C. Yee, R. Foltz, A. G. Noble, R. Demarco, A. Tudorica, M. C. Cooper, C. Lidman, S. Perlmutter, B. Hayden, K. Boone, and J. Surace, 2017, *The Astrophysical Journal*, 843, 126

6.1 Introduction – Mergers as a Quenching Mechanism in Galaxy Clusters

Major mergers between galaxies can vastly alter their appearances and properties. The gravitational interactions cause tidal tails of material to be stripped away from the galaxy, and the disruption of stellar orbits can permanently change the morphology of the resulting galaxy (Schweizer, 1982; Kauffmann et al., 1993). Although the individual stars themselves are generally too small and too far apart for direct collisions, the gas of the interstellar medium is not collisionless. In cases of a 'wet' merger, one or both of the merging galaxies are gas-rich and the resulting interactions can trigger intense periods of star-formation (Sanders & Mirabel, 1996; Ostriker & Shetty, 2011). Merging is thus an efficient and powerful mechanism for transforming the morphology and affecting the star-formation of galactic populations.

Galaxy–galaxy mergers are favored in areas where there is an overdensity of galaxies and moderate relative velocities. If the relative velocities are too low, it will take too long (beyond a Hubble time) for coalescence to occur, and if the velocities are too high they will pass by each other, perhaps interacting but not able to merge (see Mihos, 2004, for review). Galaxy clusters can provide high density environments where near neighbors are common - however, in the present day the velocity dispersions of massive virialized clusters are of the order 500–1000 km/s and not conducive to active merging amongst satellite galaxies. As would be expected, low-redshift clusters are populated by mostly red and dead populations

where star-formation occurs only in the very outskirts or the field and merger rates in higher density regions are found to be on the order of 2–3% (Adams et al., 2012; Cordero et al., 2016). Any mergers occurring in cluster environments are likely dry mergers and do not contribute to the new stellar mass assembly of the cluster via triggered star-formation. Indeed, while dry merging may be evident in lower redshift clusters (van Dokkum et al., 1999; Tran et al., 2005), stellar mass assembly in clusters has been shown to be complete by moderate redshifts of at least $z > 1$ and possibly as distant as $z > 1.5$ (Andreon & Congdon, 2014), although it has been found that mass accretion of the brightest cluster galaxy in the central core is ongoing (e.g., Lidman et al., 2012).

Nonetheless, recent studies of high-redshift galaxy overdensities (or 'proto-clusters') have seen evidence of enhanced merger rates, suggesting that merging may play an important role in mass assembly in these higher density environments. Lotz et al. (2013) identified mergers in a $z = 1.62$ proto-cluster and found an implied merger rate higher by a factor of 3–10 compared to the field. At even higher redshift, Hine et al. (2016) found elevated rates of merging Lyman-break galaxies in a $z = 3.1$ proto-cluster, with a rate enhancement of over 60% compared to the field. However, the merger rates in established clusters at high-redshift have not been investigated in detail, and it is unclear whether galaxy evolution in high-redshift cluster environments is dominated by local effects like active merging as suggested by Mancone et al. (2010), or global effects like ram-pressure stripping or strangulation from the intracluster gas.

In this chapter we investigate the fraction of potential mergers in several high-

redshift ($z > 1.5$) galaxy clusters, the largest study of its kind to date. We select four high-redshift galaxy clusters discovered in the *Spitzer* Adaptation of the Red-Sequence Cluster Survey (SpARCS) cluster catalogue and spanning a redshift range $1.59 < z < 1.71$. All four clusters have been spectroscopically confirmed and have a wealth of multiwavelength observations, including deep near-infrared imaging from *Hubble Space Telescope*. In §6.2 we summarize our datasets for both cluster and control, §6.3 outlines our merger identification method, our results are presented in §6.4 and discussed in §6.5. In this chapter we assume a ΛCDM cosmology with $H_0 = 70\text{km s}^{-1}\text{ Mpc}^{-1}$, $\Omega_M = 0.3$, and $\Omega_\Lambda = 0.7$.

6.2 Data

6.2.1 Cluster Sample

The push to identify galaxy clusters at these high-redshift epochs has resulted in the development of several novel observation techniques, and now dozens of galaxy clusters at redshifts $z > 1.3$ are known. The *Spitzer* Adaptation of the Red-Sequence Cluster Survey (SpARCS; Muzzin et al., 2009; Wilson et al., 2009) has provided over a dozen spectroscopically confirmed galaxy clusters at $z > 1.0$ and several at $z > 1.5$. Our dataset comprises four rich galaxy clusters selected from the high-redshift cluster sample of the SpARCS catalogue, including selection based on the $1.6\mu m$ Stellar Bump Sequence (SBS) method (Muzzin et al., 2013), that had been selected for extensive multiwavelength follow-up, including spectroscopy and *HST* imaging.

SpARCS104922.6+564032.5 at $z = 1.7089$ (hereafter J1049) was detected in the SpARCS coverage of the Lockman Hole and is notable for its highly star-forming brightest cluster galaxy (Webb et al., 2015a). The remaining three clusters were all detected using SBS combined with SpARCS as described in Muzzin et al. (2013). SpARCS033056−284300 ($z = 1.626$) and SpARCS022426−032331 ($z = 1.633$; hereafter J0330 and J0224) were both presented in Lidman et al. (2012), with J0224 additionally described in Muzzin et al. (2013). SpARCS022546−035517 at $z = 1.598$ (hereafter J0225) was presented in Nantais et al. (2016). The clusters are likely not fully virialized and the difficulty in obtaining spectroscopic redshifts for the passive members in the central core inhibits the ability to derive robust velocity dispersions; however, richness measurements suggest lower cluster mass limits of $10^{14}M_{\odot}$. See Table 6.1 for a summary of the cluster properties.

Spectroscopic members were confirmed using the multi-object spectrometer MOSFIRE on Keck-I and the Focal Reduction and Imaging Spectrograph 2 (FORS2) on VLT (Muzzin et al., 2013; Webb et al., 2015a; Nantais et al., 2016) with detailed reduction and analysis to be presented in DeGroot et al. (in prep). In total there are 118 confirmed spectroscopic members across the four clusters.

Multiwavelength imaging is available from optical to infrared for all four clusters. For clusters J0224, J0225, and J0330, 11 to 12 band (not including additional *HST* imaging described below) photometry is available. All three clusters have optical $ugriz$, near-infrared YK_s, and infrared (3.6μ, 4.5μm, 5.8μm, 8.0μm), with additional near-infrared J available for clusters J0224 and J0330 (Nantais et al., 2016). J1049 has 8 band photometry available with $ugrz$ from CFHT (Tu-

Table 6.1: Cluster Properties

Cluster ID	RA	Dec	z	Spec Members	*HST* Imaging	Exposure Times
SpARCS-J0225[a]	02 : 25 : 45.6	−03 : 55 : 17.1	1.598	8	F160W	2424s
SpARCS-J0330[b]	03 : 30 : 55.9	−28 : 42 : 59.5	1.626	38	F105W, F140W, F160W	10775s, 11625s, 5019s
SpARCS-J0224[b,c]	02 : 24 : 26.3	−03 : 23 : 30.8	1.633	45	F105W, F140W, F160W	7581s, 9829s, 6116s
SpARCS-J1049[d]	10 : 49 : 22.6	+56 : 40 : 32.6	1.709	27	F105W, F160W	8543s, 9237s

[a] Nantais et al. (2016)
[b] Lidman et al. (2012)
[c] Muzzin et al. (2013)
[d] Webb et al. (2015a)

dorica et al., in prep), JK_s from *UKIDSS* (Lawrence et al., 2007), and IRAC 3.6μm, 4.5μm from SERVS (Mauduit et al., 2012). Photometric redshifts were determined using EAZY (Brammer et al., 2008) for all of the clusters using the above photometry with resulting normalized median absolute deviations (σ_{nmad}) of $(z_{phot} - z_{spec})/(1 + z_{spec})$ of 0.04 for the 11/12 band photometry clusters (J0224, J0225, J0330; Nantais et al., 2016) and 0.065 for the 8 band photometry cluster (J1049). Stellar masses were derived for all clusters using FAST (Kriek et al., 2009) with Bruzual & Charlot (2003) stellar population libraries, Calzetti et al. (2000) dust law, IMF from Chabrier (2003), and assuming an exponentially declining SFR.

Deep *HST* imaging was obtained for the central regions of the four clusters in the F160W filter on the WFC3-IR camera with additional imaging in F105W and F140W for a subset of the clusters from programs GO−14327, GO−13677 and GO−13747. Programs GO−13677 (cycle 22) and GO−14327 (cycle 23) were observed as part of the "See Change" program, a large *HST* program using 174 orbits to discover and characterize ∼30 Type Ia supernovae at $z > 1$. The primary scientific goal of See Change is to improve our knowledge of the expansion history of the universe through distance measurements of high-redshift Type Ia supernovae, and calibration of the SZ−mass scaling relation using weak-lensing in the most massive, highest redshift clusters known to date. For all four clusters, the *HST* imaging covers a cluster-centric radius out to approximately 750 kpc. Standard reduction was performed on the images using the AstroDrizzle software available from the Space Telescope Science Institute. Reduced drizzled images

have a pixel scale of 0.09″ for all clusters with the exception of J0225 which has a final pixel scale of 0.128″/px. Exposure times in each filter are listed in Table 6.1.

Cluster galaxies were selected based on both spectroscopic and photometric redshifts. Spectroscopic members required a spectroscopic redshift within 1000 km/s of their respective cluster redshift. For objects that had no spectroscopy, cluster members were selected based on high quality photometric redshifts (quality parameter $q_z < 3$, as defined in Brammer et al. (2008)). Photometric cluster members required the photometric redshifts to be within $2\sigma_{nmad}$ of the cluster redshift, where σ_{nmad} is 0.065 for J1049 and 0.04 for J0224, J0225, and J0330. Additionally, a mass cut was done requiring a stellar mass greater than $3 \times 10^{10} M_{\odot}$ to ease comparison with other studies as well as ensuring completeness in all samples. The *HST* imaging covers the central 750 kpc (in cluster-centric radius) region for each cluster and each galaxy was required to reside at least 3″ (approximately 25 kpc physical) away from the edges of the *HST* imaging to allow near neighbor analysis. The final mass-selected catalogue results in a total of 59 cluster members, 23 of those confirmed spectroscopically and 36 photometrically selected.

6.2.2 Control Sample

To compare the fraction of merging systems to the field at high-redshift, we utilize the UKIDSS Deep Survey field (UDS), a pointing of the Cosmic Assembly Near-infrared Deep Extragalactic Survey (CANDELS)(Koekemoer et al., 2011). Near-infrared *HST* imaging from WFC3 is available for the UDS field in F125W and F160W to a two-orbits depth (Koekemoer et al., 2011; Grogin et al., 2011; Skelton

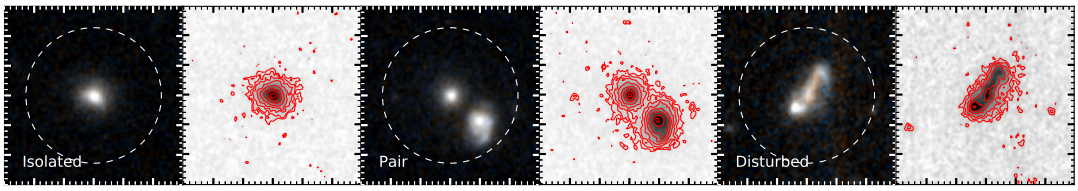

Figure 6.1: Examples of galaxies identified in each of the three classifications from the UDS control sample. Left panels are RGB images with filters F160W, F125W+F160W, F125W with a 20 kpc radius circle overlaid, and right panels are F160W grayscale maps with surface brightness shown as 0.5 mag arcsec^{-2} contours. The galaxy in the left stamp is identified as isolated, with no near neighbor within the 20 kpc radius and no significant asymmetry or distortion. The galaxy in the central stamp has a clear near neighbor within 20 kpc. The galaxy in the right stamp shows signs of tidal distortion and strong asymmetry with no clear counterpart.

et al., 2014). The extensive spectroscopy (Brammer et al., 2012; Momcheva et al., 2016) provides a large sample of confirmed high-redshift ($z \sim 1.65$) galaxies. Complementary photometric analyses utilising a combination of ground-based and space-based observations provided 18 filter photometry to determine stellar masses (Skelton et al., 2014) using FAST (Kriek et al., 2009), and derived with the same FAST parameters described above.

We select massive ($M_* \geq 3 \times 10^{10} M_\odot$) galaxies in the redshift range $1.55 < z < 1.75$ to sample the redshifts of our four clusters. Of those, 65 were selected via spectroscopic redshift and 26 selected via high quality ($q_z < 3$) photometric redshift. We do a regional cut to exclude the possibility of including members of the $z = 1.62$ spectroscopically confirmed proto-cluster presented in Papovich et al. (2010) and Tran et al. (2010). Our final control catalogue consists of 91 galaxies.

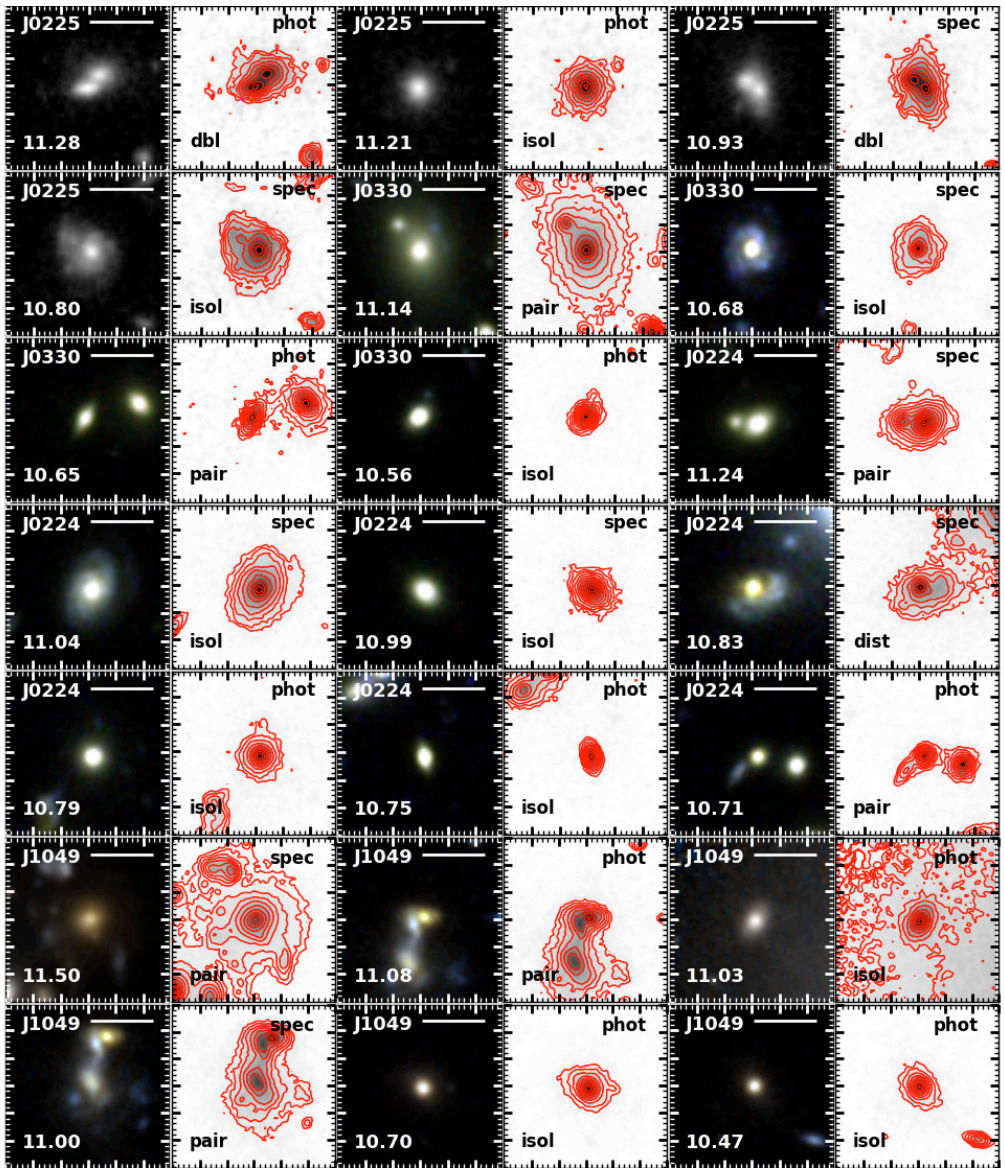

Figure 6.2: Simplified $6'' \times 6''$ stamps of a subset of cluster members. The left panels show the cluster name in the top left, a horizontal bar indicating a distance of 20 kpc physical at the cluster redshift, and the log stellar mass in the lower left. The left images show grayscale F160W stamps for J0225, three-filter RGB (F105W, F140W, F160W) for clusters J0330 and J0224, and two-filter RGB in (F105W, F105W+F160W, F160W) for J1049. The right panels for all objects show grayscale F160W images with surface brightness contours starting at 24.5 mag arcsec^{-2} and increasing by 0.5 mag arcsec^{-2}. The text in the upper right indicates whether the object was spectroscopically or photometrically selected, and the label in the lower left indicates the classification (isolated, pair, disturbed, or double nucleus).

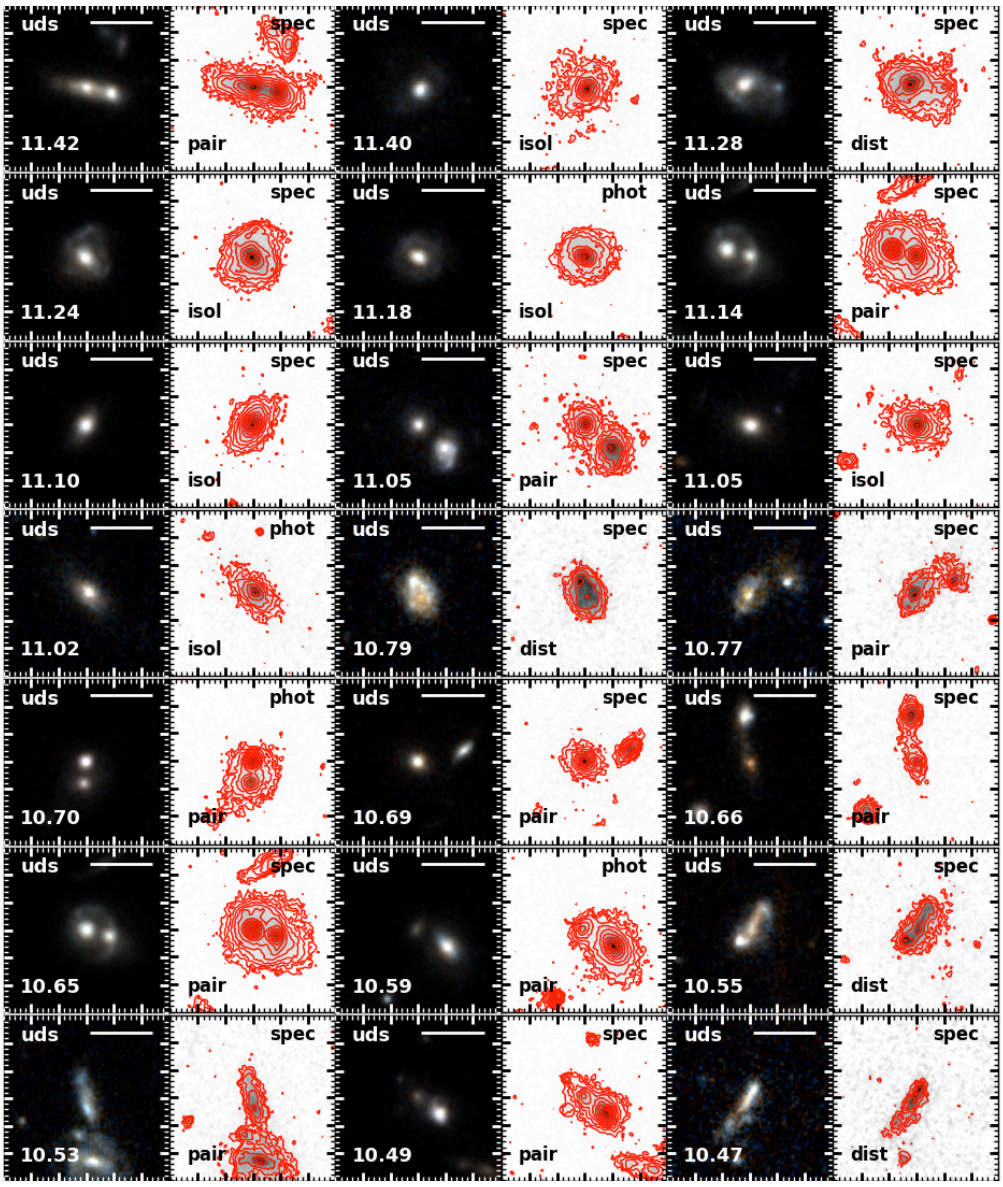

Figure 6.3: Same as Figure 6.2 but for a subset of UDS galaxies. The left panels are two-filter RGB images (F160W, F125W+F160W, F125W) and the right show grayscale F160W stamps with same contours as Figure 6.2. Labels and text are the same as Figure 6.2.

6.3 Merger Classification Methodology

HST imaging is available for all samples at a depth sufficient for morphological analyses: there is coverage in F160W for all clusters and the control sample in depths ranging from 2 to 9 orbits, as well as F125W for the control and some additional F105W and F140W for the cluster sample. The 4000Å break spans from 1.02μm to 1.10μm across the redshift range $1.55 < z < 1.75$, so color images including the F105W band are likely highlighting younger populations of stars compared to the redder filters and could introduce morphological differences not apparent in the F125W, F140W or F160W filters. Since F105W imaging is not available for all samples, for consistency the classifications were done on only single filter F160W maps.

Each object was presented as a grayscale F160W $6'' \times 6''$ stamp with segmentation map contours from SExtractor overlaid. Two additional stamps displayed surface brightness contours in both finely (0.25 mag arcsec^{-2}) and broadly spaced contours (0.5 mag arcsec^{-2}), to highlight double nuclei, tidal features, and asymmetry. These subtle features can be difficult to identify and disentangle using automatic software and by-eye classification has been utilized in many classification surveys, taking advantage of the processing power and pattern recognition afforded by the human eye (e.g. Lintott et al., 2008; Kartaltepe et al., 2015; Willett et al., 2017). Thus all objects were inspected and classified by eye to facilitate identification of features like close pairs, double nuclei, and asymmetries. Identification of advanced mergers, such as the local universe post-merger Arp220, may be difficult if the nuclei are too close to distinguish or tidal features are too faint.

However, the use of a control sample remedies this by looking for relative fractions of galaxies involved in mergers, rather than absolute numbers. To avoid bias during the classification process, each galaxy was inspected in randomized order so the location (field or cluster) was unknown during classification. J1049 has the deepest *HST* imaging in F160W; so, to ensure that there were no biases towards faint features in the deep exposure, single orbit (900s) images of J1049 were also classified blindly. The classifications were consistent with one another regardless of depth; so, for our purposes the varying exposure times for different samples is not anticipated to be a significant issue. Classifications were done individually by three people − two team members and one non-team member. Overall, classifications between all classifiers were consistent with one another and in ambiguous cases, the majority classification was used.

Galaxies were classified into three categories: Isolated, Pair, or Disturbed. Pairs were identified as having a near neighbor within a projected physical distance of 20 kpc, with no constraints on relative velocities, due to redshift incompleteness for the cluster sample. A magnitude limit of $m_{F160W} = 23.25$ for companions was used which roughly corresponds to a stellar mass of $10^{10} M_{\odot}$ at $z = 1.65$ to select for systems likely to be major merger progenitors instead of minor merger progenitors. In cases where both pair members are present in the sample based on redshift and mass requirements, the system is counted twice. Disturbed galaxies have signs of merger activity, including tidal features such as tails or major asymmetry, or double nuclei present within the segmentation map. In many cases with double nuclei the secondary peak was not detected as a separate source so

no magnitude requirement was placed on these systems. Isolated galaxies have no bright near neighbors or unusual morphology. Pairs and disturbed galaxies comprise our sample of 'potential mergers'. For example images highlighting the different classifications, see Figure 6.1.

6.4 Results

Of the 59 redshift-selected cluster objects with $M_* \geq 3 \times 10^{10} M_\odot$, 17 exhibit tidal features, double nuclei or close pairs, resulting in an observed fraction of merger candidates of $28.8^{+6.5}_{-5.1}\%$. * The UDS control sample comprising 91 objects with $M_* \geq 3 \times 10^{10} M_\odot$, contains 31 objects with tidal features, double nuclei, or close pairs, resulting in an observed fraction of merger candidates of $35.2^{+5.2}_{-4.6}\%$. Simplified versions of the stamps are shown for a subset of the cluster galaxies in Figure 6.2, and a subset of the control galaxies in Figure 6.3. Uncertainties were calculated assuming binomial statistics for 68% confidence intervals, following Cameron (2011). The results of the classification of both samples are presented in Figure 6.4 and Table 6.2.

It is likely that some identified pairs are coincidental due to proximity along the line-of-sight and do not represent intrinsic nearby pairs. For the control sample of galaxies, this was corrected by randomly scattering all galaxies in the field with $m_{160} < 23.25$ and recording how often the nearest object for each of the massive, redshift-selected galaxies was within 20 kpc. This was iterated 1000

*Since publication of this paper, four new photometric members of J1049 were identified utilizing the new z filter imaging. The results have been updated to reflect their inclusion.

Table 6.2: Merger Classification Results

Sample	$N_{spec,m}$ [a]	$N_{phot,m}$ [a]	N_{tot} [b]	$N_{merg,s}$ [c]	$N_{merg,p}$ [c]	$N_{merg,tot}$ [c]	f_{merg}	P_{int} [d]	$f_{merg,c}$ [e]
SpARCS−J0225	4	6	10	2	2	4	–	–	–
SpARCS−J0330	3	6	9	1	1	2	–	–	–
SpARCS−J0224	11	10	21	5	2	7	–	–	–
SpARCS−J1049	5	14	19	2	2	4	–	–	–
Cluster Total	23	36	59	10	7	17	$28.8^{+6.5}_{-5.1}\%$	$18.1 \pm 2.0\%$	$10.7^{+6.8}_{-5.5}\%$
UDS Control	65	26	91	24	7	31	$35.2^{+5.2}_{-4.6}\%$	$10.5 \pm 0.1\%$	$24.7^{+5.3}_{-4.6}\%$

Notes

[a] Number of objects spectroscopically or photometrically consistent with the cluster redshift, within *HST* field-of-view, and with $M_* \geq 3 \times 10^{10} \mathrm{M}_\odot$.

[b] Total number of objects included in final sample for each field.

[c] Number of galaxies in potential mergers, defined as either having a close pair with 20 kpc, or having signs of tidal features/double nuclei for spectroscopically or photometrically selected, and entire sample.

[d] Probability of interlopers falsely contributing to projected pairs.

[e] Fraction of galaxies in potential mergers after correcting for chance of interlopers.

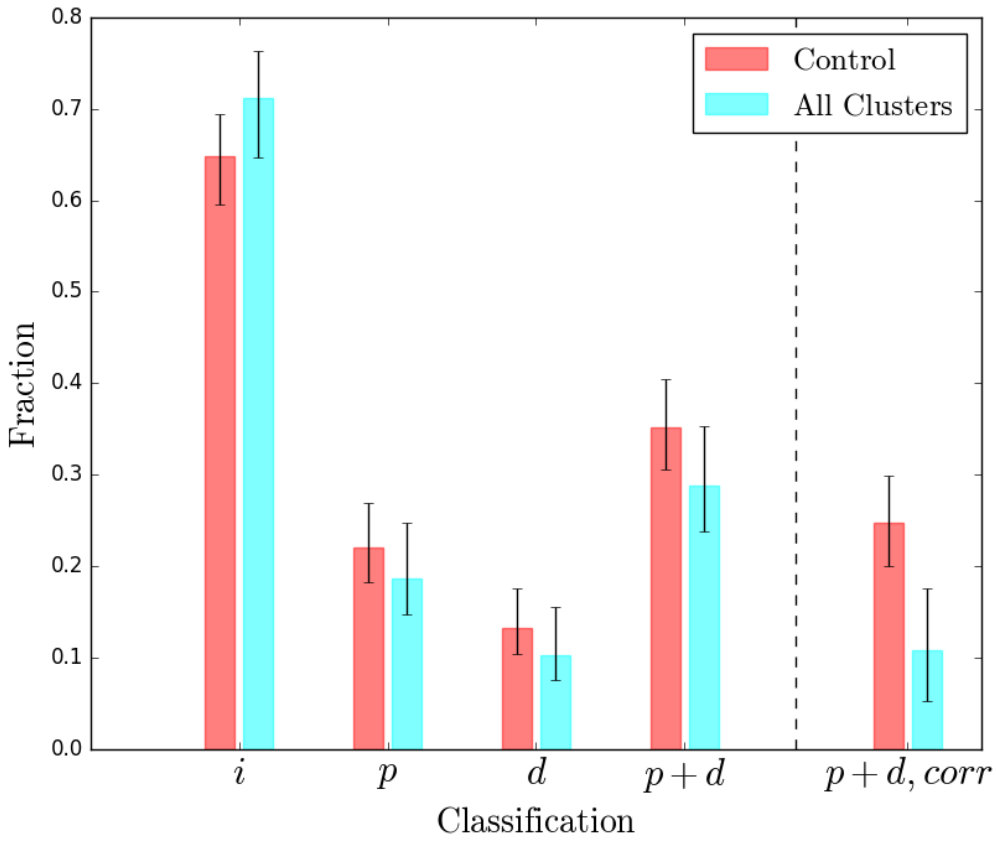

Figure 6.4: Fraction of galaxies found under each classification for UDS control sample and combined cluster sample. Left to right are isolated, pairs, disturbed, combined pairs + disturbed (representing overall merger probability) and combined pairs + disturbed after being corrected for interlopers. Errorbars show 68% confidence and were estimated assuming a binomial distribution and utilizing the beta function.

times resulting in an interloper fraction of $10.5 \pm 0.1\%$ and a corrected merger candidate fraction of $24.7^{+5.3}_{-4.6}\%$.

To preserve the overall distribution of galaxies within the clusters, where the higher densities can result in a higher probability of projected neighbors within the cluster, the interloper fraction was calculated by randomly scattering all bright objects ($m_{160} < 23.25$) within a set radius of their current positions. The scattering radius was selected to be large enough that we are not just recovering the 20 kpc pairs and small enough that the scattering does not become completely random. A scattering radius of 11.5" or 100 kpc physical at the clusters' redshift was chosen, although interloper fractions were calculated for scattering radii from 5" to 20" with the rate decreasing with increasing scattering radius and the lowest interloper fraction for uniform scattering. The combined interloper fraction across all four clusters is $18.1 \pm 2.0\%$ resulting in a corrected merger candidate fraction of $10.7^{+6.8}_{-5.5}\%$.

6.5 Discussion

We have assembled a sample of 23 spectroscopically confirmed and 36 photometrically selected massive galaxies in four galaxy clusters spanning the redshift range $1.59 < z < 1.71$, along with a comparative control sample from UKIDSS Deep Survey comprising 65 spectroscopic and 26 photometric selected massive galaxies in the redshift range $1.55 < z < 1.75$. Through blind classification, we have identified 17 merger candidates in the cluster sample and 31 merger candidates

in the control sample, resulting in potential merger fractions and 68% confidence intervals of $10.7^{+6.8}_{-5.5}$% and $24.7^{+5.3}_{-4.6}$% for the cluster and control sample, respectively, after correcting for interlopers. The potential merger fractions between the field and cluster samples are consistent within 1.6σ although we cannot rule out the possibility that merger activity is suppressed in the core cluster environments by a factor of 2 or more. However, we can rule out the possibility of a mild enhancement of merger activity compared to field (> 1.5 times) at the 3σ level and a strong enhancement (> 2 times) at the 4σ level.

Our sample is unique in that we are probing the environments of established clusters at high redshifts and our sample is significantly larger than similar studies. Previous studies by Lotz et al. (2013) and Hine et al. (2016) have identified merger fractions in lower mass proto-cluster systems at $z = 1.62$ and $z = 3.1$, finding elevated merger fractions by factors of roughly 5 and 1.5, respectively, when compared to the field. However, the enhancements are only significant at the 2σ and 1.5σ levels, respectively. While all three studies find merger fractions between the field and cluster to be within 3σ, we see no evidence of strongly elevated merger fractions in the clusters in contrast to the other two studies. A major difference between these studies and our own is the cluster environment – both Lotz et al. (2013) and Hine et al. (2016) involve lower halo mass ($\sim 10^{13}$M$_\odot$) proto-cluster environments, and we are probing the central regions (within 750 kpc) of massive, established clusters. Higher merger rates may be favored in proto-cluster environments where densities are higher than the field and infalling groups have low enough relative velocities to facilitate merging.

The galaxy cluster halo mass has been suggested to play an important role in galaxy properties, with the halo mass dependence becoming stronger at higher redshifts. Simulations by Muldrew et al. (2015) indicate that with increasing redshift, the properties and halo distributions of current epoch massive clusters vary significantly. Variations in quenching efficiencies in cluster environments are found to be largest in higher redshift samples (Nantais et al., 2017), suggesting halo mass or age may be dominant factors in galaxy evolution within cluster environments. The halo mass may also directly play a role in the number of mergers seen (Brodwin et al., 2013), with more massive clusters assembling mass at earlier epochs whereas proto-clusters of the same epoch will still be assembling and accreting members. A larger halo mass will also deepen the gravitational potential well resulting in higher relative velocities in evolved systems which inhibit interactions and mergers between members. If cluster mass is indeed a driving factor in merger activity, it would be expected to see a higher merger fraction in lower mass halos at similar redshifts, which is evident in Lotz et al. (2013) where the proto-cluster has a derived upper limit halo mass of several $10^{13}\mathrm{M}_{\odot}$ (Tanaka et al., 2010; Pierre et al., 2012), an order of magnitude smaller than our cluster sample ($\log(M_*/\mathrm{M}_{\odot}) > 14.0$).

As we see potential galaxy$-$galaxy merger fractions in central cluster regions comparable to the field, this suggests that merging is not a more dominant factor in the evolution of cluster galaxies relative to field populations. Our result is consistent with the conclusions drawn in Andreon (2013) which suggest that mass build-up in massive cluster galaxies is mostly complete by $z \sim 1.8$ and enhanced

build-up via merging in the redshift range $1.4 < z < 1.8$ is not expected in established clusters. The rapid quenching occurring in cluster populations from redshift $z \sim 1.6$ to $z \sim 1$ (e.g., van der Burg et al., 2013; Darvish et al., 2016; Nantais et al., 2016, 2017) is thus unlikely to be due to enhanced galaxy−galaxy merging, at least in the most massive cluster systems. This suggests that the driving forces in quenching cluster galaxies are more likely to be due to interactions within the intracluster medium (such as ram-pressure stripping), harassment, or mass-induced self-quenching (e.g., Peng et al., 2010; Bialas et al., 2015).

Simulations have shown that for all dark matter halos, regardless of mass, the overall halo merger rate (and implied galaxy merger rate) increases with increasing redshift (Wetzel et al., 2009). Yet the specific dependence on environment for merger rates is less studied. Overdense regions are found to have expected merger rates up to 2.5 times that of voids to a redshift of $z \sim 2$ (Fakhouri & Ma, 2009), but whether that trend holds in the densest galaxy cluster cores is less certain. De Lucia & Blaizot (2007) have traced out the merger trees of brightest cluster galaxies (BCGs) and found that at large lookback times the BCG progenitor subhalos are undergoing mergers between themselves while in the cluster environment, before being eventually accreted onto the BCG itself. N-body simulations by Berrier et al. (2009) have been used to trace back formation histories for dark matter halos in both cluster and field environments. They propose that at lookback times beyond 10 Gyr the merger rate of cluster subhalos may exceed the rate for merging field halos although this ratio drops significantly with decreasing redshift and most current cluster galaxies have not had a significant merger (greater

than 1:10) within the past several Gyr. However, at $z = 1.5$ the average rates for mergers become comparable between the two environments, consistent with the merger candidate fractions we determine in our $z \sim 1.65$ cluster and control samples.

We have derived the fraction of objects that appear to be undergoing or about to undergo mergers. The conversion from this fraction to an intrinsic merger rate is difficult, and depends on factors such as the relative velocities between pairs and timescales of tidal feature visibility. We have attempted to alleviate some of these complications by applying our requirements for identification equally across two samples (cluster and control) pulled from the same criteria in regards to stellar mass, redshift, and redshift selection method (both photometric and spectroscopic). As classification was done blindly between the two samples, any biases that could be introduced (for example due to individual classification by eye) should be present in both samples and thus not cause any discrepancies between the two. We have selected objects based on both spectroscopic and photometric redshift which allows identifications of both wet (star-forming, gas-rich) and dry (passive, quiescent) merging systems. In both spectroscopic and photometric samples the fraction of potential mergers is consistent with the corresponding field sample showing no enhancement for either wet or dry merging in these established clusters at $z \sim 1.65$.

7

Conclusion

7.1 Summary

In this thesis we have presented two studies concerning the effects of galaxy cluster environments on their constituent galaxies. In Chapter 1, we motivated the importance of galaxy clusters on galaxy evolution and outlined the various mechanisms − both in and out of cluster environments − that transform galactic populations. In Chapter 2 we introduced the instrumentation used to obtain data for these studies, as well as described the methodology for finding galaxy clusters, including RCS2319+00, a massive supercluster located at $z = 0.9$, and SpARCS1049, a

distant galaxy cluster with an intensely star-forming core at $z = 1.7$. Both studies involved the acquisition of wide-field imaging and the reduction and calibration of the multiwavelength datasets were outlined in Chapter 3. We assembled multiwavelength photometric catalogues in order to derive photometric redshifts as described in Chapter 4. In both studies, photometric redshifts were determined using 8 filter photometry, including optical, near-infrared, and infrared, and the spectral energy distribution template fitting software, EAZY (Brammer et al., 2008).

The first study was presented in Chapter 5, and involved an extensive photometric survey of the $z = 0.9$ RCS2319+00 supercluster, a triple cluster system expected to merge into a single $10^{15}M_{\odot}$ halo by $z = 0.5$. Using a catalogue of over 1,700 photometric members with an accuracy of $\sigma_{\Delta z/(1+z)} = 0.069$, we defined both local and global environmental parameters to investigate the properties of galaxies within different densities and structures. A friends-of-friends algorithm was developed to identify groupings and resulted in recovering the three cluster cores along with six large associations, which we designated groups. The colour and mass distributions of the cores, groups, and field (non-grouped) galaxies showed no evidence of preprocessing in the group environment, whereas the cores exhibited significantly redder and more massive members. We probed local environment by determining the relative overdensity based on the distance to tenth nearest neighbours. We found an overall significant trend between local overdensity and both colour and red fraction. After controlling for stellar mass by separating members into different mass bins, we found that there existed both a colour–mass relation

and a colour–density relation; mean colour and red fraction were found to increase both with stellar mass and overdensity.

Chapter 6 concerned the second study, which identified potential merging systems in a sample of high-redshift galaxy clusters. We utilized a sample of four clusters compiled from the *Spitzer* Adaptation of the Red-Sequence Cluster Survey, spanning a redshift range of $1.59 < z < 1.71$. All clusters had deep *HST* imaging taken, suitable for classifying morphologies of cluster galaxies. We identified close pairs and morphologically disturbed galaxies in both the clusters and a comparable field sample, to ascertain whether merging was a more likely avenue for galaxy transformation or quenching than other environmental processes. We found that the fraction of potential merging systems was consistent between the field and cluster samples within 1.5σ, with a smaller fraction occurring in the clusters. Thus, while merging does appear to be occurring within central cluster regions at high redshift, it is unlikely to be a more significant source of galactic evolution compared to field galaxies at the same epoch.

Both of these studies have explored galaxy cluster environments and their constituent galaxies. However, in light of recent cluster studies, it seems likely that clusters at $z \sim 0.9$ and $z \sim 1.6$ are probing different evolutionary epochs with a suggested cluster transition period at some point beyond $z \gtrsim 1$ (e.g. Mancone et al., 2010; Muzzin et al., 2012; Alberts et al., 2016; Nantais et al., 2017; Wagner et al., 2017). Indeed, we find a population of massive and quiescent galaxies comprising the supercluster cores of RCS2319 at $z = 0.9$, when considering both the highest density regions of the supercluster and the physical locations of the

cores. Galaxies located outside the core environments, including groups and isolated field galaxies, appear to have similar populations, distinctly different than the cores with, on average, lower masses and bluer colours. In the higher redshift study on the occurrence of merging systems in the central regions of $z \sim 1.65$ clusters, we find that merging is slightly less likely in clusters as it is in the field. Taken together, these studies emphasize the importance of the cluster environment directly affecting their galactic populations. If merging is not a dominant source of enhanced quenching in clusters beyond $z \sim 1.5$, then another mechanism must be responsible for the transition of star-forming cluster galaxies by $z \sim 1$. As well, if quenched populations are predominantly found in cluster cores and not evident in infalling groups, as seen in RCS2319, then the populations are likely being transformed once being accreted onto the cluster cores. These results both support the idea that interactions with the intra-cluster medium (ICM) cause significant transformations of accreted cluster galaxies. Quenching mechanisms related to the ICM such as strangulation and ram-pressure stripping are thus favoured to be dominant sources of the evolution of cluster galaxies.

7.2 Future Work

7.2.1 RCS2319

Tracing out the intrinsic structure in the distribution of galaxies within a field can be exceedingly difficult with photometric redshifts, even with relatively accurate photometric redshifts with $\sigma_{\Delta z/(1+z)} \sim 0.02$ (Cooper et al., 2005). Malavasi

et al. (2016) illustrate the observed 'smearing' of structure across redshifts with even more reliable photometric redshifts with $\sigma_{\Delta z/(1+z)} = 0.01$. Thus, it is safe to say that to recover the intrinsic local densities for members of RCS2319, spectroscopy remains the optimal method. While the extensive spectroscopic campaign presented in Faloon et al. (2013) has revealed a complicated web of infalling groups and intracluster structure, the spectroscopic coverage is not uniform across the field. The most massive cluster, Cluster A, has had a notably higher density of spectroscopic targets compared to the other clusters. Indeed, Cluster B, around which we have revealed significant structure in the form of friends-of-friends groups, has the lowest spectroscopic completeness. The photometric redshifts can detect the presence of structure but not the detailed distributions or dynamics of the systems which can be revealed with further spectroscopy.

We do not detect evidence of preprocessing occurring in the group environments of RCS2319. As the core populations appear significantly different from the field and group populations, this suggests that the immediate cluster environment is the dominant source of galactic evolution, and that galaxies are being quenched as they fall into the cluster halo. Additionally, we uncover a colour–density relation after controlling for mass, implying that there are density dependent quenching mechanisms affecting the cluster galaxies. Determining the key processes affecting the infalling populations requires imaging with high enough resolution, such as the *HST*, to measure galaxy morphologies and asymmetries. Distortion or asymmetry in group populations, such as the filament, could suggest that star-formation is being triggered by galaxy–galaxy interactions such as merging or harassment. If

the ICM is responsible for quenching infalling populations, there will be morphological evidence of strangulation or ram-pressure stripping. Kelkar et al. (2017), for example, have discovered an enhanced fraction of quiescent spiral galaxies in moderate redshift ($0.4 < z < 0.8$) cluster environments indicative of strangulation, where star-formation is quenched but the initial morphology remains unchanged.

7.2.2 Mergers

The push for identifying high-redshift clusters is ongoing and has produced dozens of candidates beyond redshifts of $z = 1.5$ (e.g., Papovich et al., 2010; Stanford et al., 2012; Zeimann et al., 2012; Muzzin et al., 2013; Tozzi et al., 2013; Bleem et al., 2015) and even $z = 2$ (Gobat et al., 2011; Spitler et al., 2012; Wang et al., 2016). While the spatial distributions and halo masses of high-redshift clusters can be used to derive cosmological parameters (Allen et al., 2011; Hou et al., 2014), an increasing sample of high-redshift clusters and proto-clusters will provide insight into the evolutionary track of early universe galaxies and the build-up of mass in the largest structures of the local universe.

The study presented in this thesis on merging systems in high-redshift galaxy clusters represents a first stage in examining the morphological properties of the galaxies in these massive systems. There are ongoing spectroscopic campaigns to identify more cluster members in the presented clusters which can be used to increase sample size and decrease uncertainties on merger candidate fractions. Additionally, expanding the study to further redshift regimes can uncover redshift dependencies on merging as a quenching mechanism. As Nantais et al. (2017)

shows, the quenching efficiency in cluster environments rapidly increases from $z \sim 1.6$ to $z \sim 1.3$ and continues to increase at lower redshift. Applying a similar analysis of clusters across multiple epochs can determine whether the merging fraction is correlated with quenching efficiency. Interestingly, as shown in Table 6.2, spectroscopically identified cluster members had a slightly higher chance to be identified as a potential merger. Especially at high-redshift, spectroscopy can more readily identify star-forming galaxies due to the present of bright emission lines, whereas photometric redshifts characterize the spectral continuum and are more likely to uncover quiescent galaxies. In addition to deriving the overall merger candidate fractions across redshift, it would also be interesting to see if the fraction of 'wet' (star-forming) mergers changes with respect to the fraction of 'dry' (quiescent) mergers. Dry mergers are not a quenching mechanism as both galaxies involved in the interaction would have already had their gas depleted, while wet mergers only occur when one or both galaxies have a sufficient reservoir of gas to trigger periods of star-formation. Indeed, tracing both the total merger fraction and wet/dry merger fractions with redshift will provide insight into the processes involved in quenching across these epochs.

In addition to investigating the effect of redshift on merging, both wet and dry, as discussed in Chapter 6 there is also the possibility that the cluster halo mass plays a significant role. As Brodwin et al. (2013) postulates, the most massive clusters would have formed at earlier epochs and ongoing mass assembly would thus be more active in lower mass haloes at a given redshift. While we are limited by small numbers, we do find the highest fraction of merger candidates

in the least rich cluster (SpARCS–J0225) based on the number of infrared bright galaxies, N_{gal}, as described by Webb et al. (2015a). Following the same richness metric, the two richest clusters (SpARCS−J0330 and SpARCS−J1049) exhibit the lowest merger fractions. While the richness provides an estimate for halo mass, there are other methods that could better ascertain the masses of these systems and eke out any halo mass dependence there may be. Indeed, since the clusters are cosmologically young, it is unlikely they are virialized and so dynamical mass estimates may either over or underestimate their intrinsic masses. In a similar vein, the luminosity of the X-ray halo can be used to infer total cluster mass but it may not yet be established, or luminous enough, at these high redshifts. However, X-ray haloes and corresponding M_{500} have been done for clusters beyond $z = 1.2$ and even as high as $z = 1.85$ (McDonald et al., 2017). Weak-lensing provides a relatively unbiased measurement, but requires deep and high quality imaging. Fortunately, the four clusters presented in Chapter 6 all have deep (and in most cases, multiwavelength) observations from the *Hubble Space Telescope*. As mentioned in Chapter 6, *HST* observations were part of the "SeeChange" program, which included deep observations on a total of 12 high-redshift clusters. Weak-lensing mass estimates have already been produced for two other high-redshift clusters ($z = 1.48$ and $z = 1.75$) in the SeeChange program (Jee et al., 2017), and would provide excellent cluster mass estimates when applied to rest of the cluster sample.

While the cluster environment as a whole provides an important laboratory for understanding evolutionary processes, the cores of the clusters themselves have

exhibited some unexpected properties. Webb et al. (2015b) and Bonaventura et al. (2017) have revealed a population of high-redshift ($z \gtrsim 1$) brightest cluster galaxies (BCGs) with significant star-formation rates of hundreds to thousands of solar masses per year. The enhanced levels of SFR in these galaxies challenges the idea that their mass is mostly established by high redshift ($z \sim 3$) with ongoing mass assembly due to minor or dry mergers (De Lucia & Blaizot, 2007). Instead, it is appearing likely that wet mergers and the triggered star-formation could be responsible for a significant fraction of the BCG mass. Indeed, of the sample of four BCGs in the study presented here, three exhibit some form of merging or tidal distortions. As shown in Webb et al. (2015a), the BCG in SpARCS1049 is surrounded by a complicated, diffuse structure (mostly outside the $6'' \times 6''$ stamp shown in Figure 6.2) indicative of gas and stars funnelling towards the BCG core. While the BCGs have been studied in terms of star-formation indicators including infrared and submillimetre emission, an extensive morphological study has not been yet been done. The complicated morphology of the SpARCS1049 BCG has shown that wet merging can occur in these massive galaxies, and future morphology studies of other high-redshift BCGs can reveal whether this galaxy is a unique outlier, or whether the accepted paradigm of how BCGs accrete their mass at high-redshift needs to be revised.

A

Observations of Additional RCS Clusters

The multiwavelength observations of the RCS2319 supercluster were part of a much larger follow-up survey for a subset of RCS identified clusters. Observations were done in optical bands g' and i' from MegaCam, complementing the R_C and z' observations from RCS, as well as near-infrared bands J, K_s, and a subset in H.

Table A.1 summarizes the observations done for the selected RCS clusters. All observations listed below were processed, reduced, mosaicked, and calibrated following the method outlined in Chapter 3. Multiwavelength catalogues were produced including optical and near-infrared photometry and spectroscopy, enabling

any future work or projects involving the extensive RCS cluster catalogue.

Table A.1: Subset of RCS clusters with observations taken with MegaCam (g' and i') and WIRCam (J, H, and K_s). z_{cl} is the photometric cluster redshift based on the red-sequence, or the spectroscopic redshift where available.

Cluster ID	z_{cl}	g'	i'	J	H	K_s
RCS145226+08	0.283	–	–	✓	✓	✓
RCS022403–02	0.329	✓	✓	✓	–	✓
RCS132655+30	0.343	–	–	✓	✓	✓
RCS022516+00	0.358	✓	✓	✓	–	✓
RCS231526–00	0.385	✓	✓	✓	–	✓
RCS035139–09	0.389	✓	✓	✓	–	✓
RCS022359+01	0.393	✓	✓	–	–	–
RCS092821+36	0.393	✓	✓	✓	✓	✓
RCS215223–05	0.480	✓	✓	✓	✓	✓
RCS110733–05	0.512	–	–	✓	–	✓
RCS110104–03	0.602	–	–	✓	–	✓
RCS144654+08	0.629	–	–	✓	–	✓
RCS144557+08	0.630	–	–	✓	–	✓
RCS215248–06	0.650	✓	✓	✓	–	✓
RCS141910+53	0.710	–	–	✓	–	✓
RCS110246–04	0.723	–	–	✓	–	✓
RCS044106–28	0.734	✓	✓	✓	–	✓
RCS144726+08	0.735	–	–	✓	✓	✓
RCS022433–00	0.773	✓	✓	✓	–	✓
RCS162002+29	0.870	✓	✓	✓	–	✓
RCS231955+00	0.905	✓	✓	✓	–	✓
RCS022158–03	0.914	✓	✓	✓	–	✓
RCS043932–29	0.936	✓	✓	✓	–	✓
RCS110118–03	0.946	–	–	✓	–	✓
RCS022056–03	1.026	✓	✓	✓	–	✓
RCS132629+29	1.045	–	–	✓	–	✓
RCS132939+28	1.047	–	–	✓	–	✓

References

Abell, G. O. 1958, ApJS, 3, 211

Adams, S. M., Zaritsky, D., Sand, D. J., et al. 2012, AJ, 144, 128

Alam, S., Albareti, F. D., Allende Prieto, C., et al. 2015, ApJS, 219, 12

Alberts, S., Pope, A., Brodwin, M., et al. 2014, MNRAS, 437, 437

—. 2016, ApJ, 825, 72

Allen, S. W., Evrard, A. E., & Mantz, A. B. 2011, ARA&A, 49, 409

Andreon, S. 2010, MNRAS, 407, 263

—. 2013, A&A, 554, A79

Andreon, S., & Congdon, P. 2014, A&A, 568, A23

Baldry, I. K., Balogh, M. L., Bower, R. G., et al. 2006, MNRAS, 373, 469

Baldry, I. K., Glazebrook, K., Brinkmann, J., et al. 2004, ApJ, 600, 681

Balogh, M. L., Baldry, I. K., Nichol, R., et al. 2004, ApJ, 615, L101

Berrier, J. C., Stewart, K. R., Bullock, J. S., et al. 2009, ApJ, 690, 1292

Bialas, D., Lisker, T., Olczak, C., Spurzem, R., & Kotulla, R. 2015, A&A, 576, A103

Blanton, M. R., & Roweis, S. 2007, AJ, 133, 734

Bleem, L. E., Stalder, B., de Haan, T., et al. 2015, ApJS, 216, 27

Bolzonella, M., Miralles, J.-M., & Pelló, R. 2000, A&A, 363, 476

Bonaventura, N. R., Webb, T. M. A., Muzzin, A., et al. 2017, MNRAS, 469, 1259

Bower, R. G., Lucey, J. R., & Ellis, R. S. 1992, MNRAS, 254, 601

Boylan-Kolchin, M., Springel, V., White, S. D. M., Jenkins, A., & Lemson, G. 2009, MNRAS, 398, 1150

Brammer, G. B., van Dokkum, P. G., & Coppi, P. 2008, ApJ, 686, 1503

Brammer, G. B., van Dokkum, P. G., Franx, M., et al. 2012, ApJS, 200, 13

Brodwin, M., Stanford, S. A., Gonzalez, A. H., et al. 2013, ApJ, 779, 138

Brown, M. J. I., Webster, R. L., & Boyle, B. J. 2000, MNRAS, 317, 782

Bruzual, G., & Charlot, S. 2003, MNRAS, 344, 1000

Butcher, H., & Oemler, Jr., A. 1984, ApJ, 285, 426

Calzetti, D., Armus, L., Bohlin, R. C., et al. 2000, ApJ, 533, 682

Cameron, E. 2011, Proc. Astr. Soc. Aust., 28, 128

Caon, N., Capaccioli, M., & D'Onofrio, M. 1993, MNRAS, 265, 1013

Carlberg, R. G., Yee, H. K. C., Ellingson, E., et al. 1996, ApJ, 462, 32

Chabrier, G. 2003, PASP, 115, 763

Ciliegi, P., Zamorani, G., Hasinger, G., et al. 2003, A&A, 398, 901

Clements, D. L., Braglia, F. G., Hyde, A. K., et al. 2014, MNRAS, 439, 1193

Colless, M., Dalton, G., Maddox, S., et al. 2001, MNRAS, 328, 1039

Conroy, C., Gunn, J. E., & White, M. 2009, ApJ, 699, 486

Cooper, M. C., Newman, J. A., Madgwick, D. S., et al. 2005, ApJ, 634, 833

Cooper, M. C., Newman, J. A., Weiner, B. J., et al. 2008, MNRAS, 383, 1058

Coppin, K., Chapin, E. L., Mortier, A. M. J., et al. 2006, MNRAS, 372, 1621

Coppin, K. E. K., Geach, J. E., Webb, T. M. A., et al. 2012, ApJ, 749, L43

Cordero, J. P., Campusano, L. E., De Propris, R., et al. 2016, ApJ, 817, L6

Crowl, H. H., Kenney, J. D. P., van Gorkom, J. H., & Vollmer, B. 2005, AJ, 130, 65

Dahlen, T., Mobasher, B., Faber, S. M., et al. 2013, ApJ, 775, 93

Darvish, B., Mobasher, B., Sobral, D., et al. 2016, ApJ, 825, 113

De Lucia, G., & Blaizot, J. 2007, MNRAS, 375, 2

Dressler, A. 1980, ApJ, 236, 351

Dressler, A., Oemler, Jr., A., Butcher, H. R., & Gunn, J. E. 1994, ApJ, 430, 107

Eke, V. R., Cole, S., & Frenk, C. S. 1996, MNRAS, 282, astro-ph/9601088

Elbaz, D., Daddi, E., Le Borgne, D., et al. 2007, A&A, 468, 33

Fakhouri, O., & Ma, C.-P. 2009, MNRAS, 394, 1825

Faloon, A. J., Webb, T. M. A., Ellingson, E., et al. 2013, ApJ, 768, 104

Geach, J. E., Ellis, R. S., Smail, I., Rawle, T. D., & Moran, S. M. 2011, MNRAS, 413, 177

Gilbank, D. G., Yee, H. K. C., Ellingson, E., et al. 2008, ApJ, 677, L89

Gioia, I. M., & Luppino, G. A. 1994, ApJS, 94, 583

Gioia, I. M., Maccacaro, T., Schild, R. E., et al. 1990, ApJS, 72, 567

Gladders, M. D., Hoekstra, H., Yee, H. K. C., Hall, P. B., & Barrientos, L. F. 2003, ApJ, 593, 48

Gladders, M. D., & Yee, H. K. C. 2000, AJ, 120, 2148

—. 2005, ApJS, 157, 1

Gladders, M. D., Yee, H. K. C., Majumdar, S., et al. 2007, ApJ, 655, 128

Gobat, R., Daddi, E., Onodera, M., et al. 2011, A&A, 526, A133

Gómez, P. L., Nichol, R. C., Miller, C. J., et al. 2003, ApJ, 584, 210

Gonzalez, A. H., Sivanandam, S., Zabludoff, A. I., & Zaritsky, D. 2013, ApJ, 778, 14

Grogin, N. A., Kocevski, D. D., Faber, S. M., et al. 2011, ApJS, 197, 35

Grützbauch, R., Chuter, R. W., Conselice, C. J., et al. 2011, MNRAS, 412, 2361

Gunn, J. E., & Gott, III, J. R. 1972, ApJ, 176, 1

Haines, C. P., Pereira, M. J., Smith, G. P., et al. 2013, ApJ, 775, 126

Hasinger, G., Burg, R., Giacconi, R., et al. 1993, A&A, 275, 1

—. 1998, A&A, 329, 482

Hasinger, G., Altieri, B., Arnaud, M., et al. 2001, A&A, 365, L45

Henry, J. P. 2000, ApJ, 534, 565

Hicks, A. K., Ellingson, E., Bautz, M., et al. 2008, ApJ, 680, 1022

Hine, N. K., Geach, J. E., Alexander, D. M., et al. 2016, MNRAS, 455, 2363

Hogg, D. W., Blanton, M., Strateva, I., et al. 2002, AJ, 124, 646

Hogg, D. W., Blanton, M. R., Brinchmann, J., et al. 2004, ApJ, 601, L29

Holden, B. P., Illingworth, G. D., Franx, M., et al. 2007, ApJ, 670, 190

Hopkins, P. F., Hernquist, L., Cox, T. J., & Kereš, D. 2008, ApJS, 175, 356

Hou, Z., Reichardt, C. L., Story, K. T., et al. 2014, ApJ, 782, 74

Huang, J.-S., Barmby, P., Fazio, G. G., et al. 2004, ApJS, 154, 44

Huchra, J. P., & Geller, M. J. 1982, ApJ, 257, 423

Ilbert, O., Capak, P., Salvato, M., et al. 2009, ApJ, 690, 1236

Ivison, R. J., Greve, T. R., Smail, I., et al. 2002, MNRAS, 337, 1

Jee, M. J., Ko, J., Perlmutter, S., et al. 2017, ApJ, 847, 117

Jee, M. J., Dawson, K. S., Hoekstra, H., et al. 2011, ApJ, 737, 59

Kartaltepe, J. S., Mozena, M., Kocevski, D., et al. 2015, ApJS, 221, 11

Kauffmann, G., White, S. D. M., & Guiderdoni, B. 1993, MNRAS, 264, 201

Kauffmann, G., White, S. D. M., Heckman, T. M., et al. 2004, MNRAS, 353, 713

Kauffmann, G., Heckman, T. M., White, S. D. M., et al. 2003, MNRAS, 341, 33

Kawara, K., Sato, Y., Matsuhara, H., et al. 1998, A&A, 336, L9

Kawinwanichakij, L., Papovich, C., Quadri, R. F., et al. 2017, ApJ, 847, 134

Kelkar, K., Gray, M. E., Aragón-Salamanca, A., et al. 2017, MNRAS, 469, 4551

Kodama, T., Tanaka, M., Tamura, T., et al. 2005, PASJ, 57, 309

Koekemoer, A. M., Faber, S. M., Ferguson, H. C., et al. 2011, ApJS, 197, 36

Kriek, M., & Conroy, C. 2013, ApJ, 775, L16

Kriek, M., van Dokkum, P. G., Labbé, I., et al. 2009, ApJ, 700, 221

Lai, C.-C., Lin, L., Jian, H.-Y., et al. 2016, ApJ, 825, 40

Larson, R. B., Tinsley, B. M., & Caldwell, C. N. 1980, ApJ, 237, 692

Lawrence, A., Warren, S. J., Almaini, O., et al. 2007, MNRAS, 379, 1599

Li, I. H., Yee, H. K. C., & Ellingson, E. 2009, ApJ, 698, 83

Lidman, C., Suherli, J., Muzzin, A., et al. 2012, MNRAS, 427, 550

Lidman, C. E., & Peterson, B. A. 1996, AJ, 112, 2454

Lilly, S. J., Le Fevre, O., Hammer, F., & Crampton, D. 1996, ApJ, 460, L1

Lintott, C. J., Schawinski, K., Slosar, A., et al. 2008, MNRAS, 389, 1179

Lockman, F. J., Jahoda, K., & McCammon, D. 1986, ApJ, 302, 432

Lonsdale, C. J., Smith, H. E., Rowan-Robinson, M., et al. 2003, PASP, 115, 897

López-Cruz, O., Barkhouse, W. A., & Yee, H. K. C. 2004, ApJ, 614, 679

Lotz, J. M., Papovich, C., Faber, S. M., et al. 2013, ApJ, 773, 154

Mahony, E. K., Morganti, R., Prandoni, I., van Bemmel, I., & LOFAR Surveys Key Science Project. 2016, Astronomische Nachrichten, 337, 135

Malavasi, N., Pozzetti, L., Cucciati, O., Bardelli, S., & Cimatti, A. 2016, A&A, 585, A116

Mancone, C. L., Gonzalez, A. H., Brodwin, M., et al. 2010, ApJ, 720, 284

Martin, D. C., Fanson, J., Schiminovich, D., et al. 2005, ApJ, 619, L1

Mauduit, J.-C., Lacy, M., Farrah, D., et al. 2012, PASP, 124, 714

McDonald, M., Stalder, B., Bayliss, M., et al. 2016, ApJ, 817, 86

McDonald, M., Allen, S. W., Bayliss, M., et al. 2017, ApJ, 843, 28

Mihos, J. C. 2004, Clusters of Galaxies: Probes of Cosmological Structure and Galaxy Evolution, 277

Momcheva, I. G., Brammer, G. B., van Dokkum, P. G., et al. 2016, ApJS, 225, 27

Moore, B., Katz, N., Lake, G., Dressler, A., & Oemler, A. 1996, Nature, 379, 613

Moore, B., Lake, G., & Katz, N. 1998, ApJ, 495, 139

Mortier, A. M. J., Serjeant, S., Dunlop, J. S., et al. 2005, MNRAS, 363, 563

Muldrew, S. I., Hatch, N. A., & Cooke, E. A. 2015, MNRAS, 452, 2528

Muzzin, A., Wilson, G., Demarco, R., et al. 2013, ApJ, 767, 39

Muzzin, A., Wilson, G., Yee, H. K. C., et al. 2009, ApJ, 698, 1934

—. 2012, ApJ, 746, 188

Nantais, J. B., van der Burg, R. F. J., Lidman, C., et al. 2016, A&A, 592, A161

Nantais, J. B., Muzzin, A., van der Burg, R. F. J., et al. 2017, MNRAS, 465, L104

Ostriker, E. C., & Shetty, R. 2011, ApJ, 731, 41

Papovich, C., Momcheva, I., Willmer, C. N. A., et al. 2010, ApJ, 716, 1503

Patel, S. G., Holden, B. P., Kelson, D. D., Illingworth, G. D., & Franx, M. 2009, ApJ, 705, L67

Peacock, J. A., Cole, S., Norberg, P., et al. 2001, Nature, 410, 169

Peng, Y., Maiolino, R., & Cochrane, R. 2015, Nature, 521, 192

Peng, Y.-j., Lilly, S. J., Kovač, K., et al. 2010, ApJ, 721, 193

Pierre, M., Clerc, N., Maughan, B., et al. 2012, A&A, 540, A4

Planck Collaboration, Ade, P. A. R., Aghanim, N., et al. 2016, A&A, 594, A13

Postman, M., Lubin, L. M., Gunn, J. E., et al. 1996, AJ, 111, 615

Quadri, R. F., Williams, R. J., Franx, M., & Hildebrandt, H. 2012, ApJ, 744, 88

Rosati, P., Della Ceca, R., Norman, C., & Giacconi, R. 1998, ApJ, 492, L21

Sanders, D. B., & Mirabel, I. F. 1996, ARA&A, 34, 749

Santos, J. S., Altieri, B., Valtchanov, I., et al. 2015, MNRAS, 447, L65

Schawinski, K., Urry, C. M., Simmons, B. D., et al. 2014, MNRAS, 440, 889

Schulz, S., & Struck, C. 2001, MNRAS, 328, 185

Schweizer, F. 1982, ApJ, 252, 455

Scoville, N., Abraham, R. G., Aussel, H., et al. 2007, ApJS, 172, 38

Sersic, J. L. 1968, Atlas de Galaxias Australes

Simon, P., Watts, P., Schneider, P., et al. 2008, A&A, 479, 655

Skelton, R. E., Whitaker, K. E., Momcheva, I. G., et al. 2014, ApJS, 214, 24

Skrutskie, M. F., Cutri, R. M., Stiening, R., et al. 2006, AJ, 131, 1163

Spitler, L. R., Labbé, I., Glazebrook, K., et al. 2012, ApJ, 748, L21

Springel, V., White, S. D. M., Jenkins, A., et al. 2005, Nature, 435, 629

Stanford, S. A., Eisenhardt, P. R., & Dickinson, M. 1998, ApJ, 492, 461

Stanford, S. A., Brodwin, M., Gonzalez, A. H., et al. 2012, ApJ, 753, 164

Strateva, I., Ivezić, Ž., Knapp, G. R., et al. 2001, AJ, 122, 1861

Strazzullo, V., Gobat, R., Daddi, E., et al. 2013, ApJ, 772, 118

Tanaka, M., Finoguenov, A., & Ueda, Y. 2010, ApJ, 716, L152

Taranu, D. S., Hudson, M. J., Balogh, M. L., et al. 2014, MNRAS, 440, 1934

Tody, D. 1986, in Proc. SPIE, Vol. 627, Instrumentation in astronomy VI, ed. D. L. Crawford, 733

Toomre, A., & Toomre, J. 1972, ApJ, 178, 623

Tozzi, P., Santos, J. S., Nonino, M., et al. 2013, A&A, 551, A45

Tran, K.-V. H., van Dokkum, P., Franx, M., et al. 2005, ApJ, 627, L25

Tran, K.-V. H., Papovich, C., Saintonge, A., et al. 2010, ApJ, 719, L126

van der Burg, R. F. J., Muzzin, A., Hoekstra, H., et al. 2013, A&A, 557, A15

van der Wel, A. 2008, ApJ, 675, L13

van Dokkum, P. G., Franx, M., Fabricant, D., Kelson, D. D., & Illingworth, G. D. 1999, ApJ, 520, L95

Wagner, C. R., Courteau, S., Brodwin, M., et al. 2017, ApJ, 834, 53

Wang, T., Elbaz, D., Daddi, E., et al. 2016, ApJ, 828, 56

Webb, T., Noble, A., DeGroot, A., et al. 2015a, ApJ, 809, 173

Webb, T. M. A., O'Donnell, D., Yee, H. K. C., et al. 2013, AJ, 146, 84

Webb, T. M. A., Muzzin, A., Noble, A., et al. 2015b, ApJ, 814, 96

Wetzel, A. R., Cohn, J. D., & White, M. 2009, MNRAS, 395, 1376

Willett, K. W., Galloway, M. A., Bamford, S. P., et al. 2017, MNRAS, 464, 4176

Wilson, G., Muzzin, A., Yee, H. K. C., et al. 2009, ApJ, 698, 1943

York, D. G., Adelman, J., Anderson, Jr., J. E., et al. 2000, AJ, 120, 1579

Zeimann, G. R., Stanford, S. A., Brodwin, M., et al. 2012, ApJ, 756, 115

Zwicky, F., & Rudnicki, K. 1963, ApJ, 137, 707